



2

# NAVAL POSTGRADUATE SCHOOL

## Monterey, California



# THESIS

DTIC  
ELECTE  
SEP 24 1991  
S B D

A Calibration of the Naval Postgraduate School Middle  
Ultraviolet Spectrograph and an Analysis of the OII 2470 Å  
and OI 2972 Å Emissions Obtained from Mid-Latitude  
Rocket Observations

by

Carl K. Andersen

September 1990

Thesis Advisor:

David D. Cleary

Approved for public release; distribution is unlimited.

91-11304



9 1 9 23 046

UNCLASSIFIED

SECURITY CLASSIFICATION OF THIS PAGE

REPORT DOCUMENTATION PAGE				Form Approved OMB No 0704-0188	
1a REPORT SECURITY CLASSIFICATION <b>UNCLASSIFIED</b>			1b RESTRICTIVE MARKINGS		
2a SECURITY CLASSIFICATION AUTHORITY			3 DISTRIBUTION / AVAILABILITY OF REPORT <b>Approved for public release, distribution is unlimited</b>		
2b DECLASSIFICATION / DOWNGRADING SCHEDULE					
4 PERFORMING ORGANIZATION REPORT NUMBER(S)			5 MONITORING ORGANIZATION REPORT NUMBER(S)		
6a NAME OF PERFORMING ORGANIZATION <b>Naval Postgraduate School</b>		6b OFFICE SYMBOL <b>33</b> (if applicable)	7a NAME OF MONITORING ORGANIZATION <b>Naval Postgraduate School</b>		
6c ADDRESS (City, State, and ZIP Code) <b>Monterey, CA 93943-5000</b>			7b ADDRESS (City, State, and ZIP Code) <b>Monterey, CA 93943-5000</b>		
8a NAME OF FUNDING / SPONSORING ORGANIZATION		8b OFFICE SYMBOL (if applicable)	9 PROCUREMENT INSTRUMENT IDENTIFICATION NUMBER		
8c ADDRESS (City, State, and ZIP Code)			10 SOURCE OF FUNDING NUMBERS		
			PROGRAM ELEMENT NO	PROJECT NO	TASK NO
			WORK UNIT ACCESSION NO		
11 TITLE (Include Security Classification) <b>A Calibration of the Naval Postgraduate School Middle Ultraviolet Spectrograph and an Analysis of the OII 2470 Å and OI 2972 Å Emissions Obtained by Mid-Latitude Rocket Observations</b>					
12 PERSONAL AUTHOR(S) <b>Andersen, Carl K.</b>					
13a TYPE OF REPORT <b>Master's Thesis</b>		13b TIME COVERED FROM _____ TO _____	14 DATE OF REPORT (Year, Month, Day) <b>September, 1990</b>		15 PAGE COUNT <b>119</b>
16 SUPPLEMENTARY NOTATION <b>The views expressed in this thesis are those of the author and do not reflect the official policy or positions of the Department of Defense or the U.S. Government.</b>					
17 COSATI CODES			18 SUBJECT TERMS (Continue on reverse if necessary and identify by block number)		
FIELD	GROUP	SUB-GROUP	<b>Ebert-Fastie Spectrograph; Ultraviolet spectra; Dayglow; OII 2470 Å Multiplet; OI 2972 Å Line Emission</b>		
19 ABSTRACT (Continue on reverse if necessary and identify by block number)  <b>The MUSTANG instrument was calibrated using standard techniques to determine the sensitivity and wavelength calibrations and field of view. The instrument was launched aboard a NASA sounding rocket on March 30, 1990. Post-flight tests indicated that the calibration did not change as a result of the rocket experiment. Ultraviolet dayglow spectra of the Earth's ionosphere were obtained from approximately 100 km to 320 km in altitude over a wavelength range of 1800 Å to 3400 Å. The spectra were divided into 512 pixels of approximately 3.134 Å per pixel. Analyses of the data from 2420 Å to 2490 Å and from 2920 Å to 2972 Å were conducted to obtain the intensity profiles of the OII 2470.4 Å multiplet and the OI 2972.3 Å line emission, respectively. The intensity profile of the OII 2470.4 Å multiplet was found to have a broad peak of 1.6 kR centered at approximately 250 km. The intensity profile of the OI 2972.3 Å line emission shows a general trend of decreasing intensity with altitude. The maximum intensity of 3.6 kR was found at 105 km and the minimum of 137 R at 315 km. A partial layer, with an intensity of 4.1 kR, was evident near 150 km.</b>					
20 DISTRIBUTION / AVAILABILITY OF ABSTRACT <input checked="" type="checkbox"/> UNCLASSIFIED/UNLIMITED <input type="checkbox"/> SAME AS RPT <input type="checkbox"/> DTIC USERS			21 ABSTRACT SECURITY CLASSIFICATION		
22a NAME OF RESPONSIBLE INDIVIDUAL <b>David D. Cleary</b>			22b TELEPHONE (Include Area Code) <b>(408) 646-2828</b>		22c OFFICE SYMBOL <b>61-CL</b>

DD Form 1473, JUN 86

Previous editions are obsolete

S/N 0102-LF-014-6603

SECURITY CLASSIFICATION OF THIS PAGE

UNCLASSIFIED

Approved for public release; distribution is unlimited

**A Calibration of the Naval Postgraduate School Middle Ultraviolet Spectrograph  
and an Analysis of the OII 2470 Å and OI 2972 Å Emissions  
Obtained from Mid-Latitude Rocket Observations**

by

**Carl K. Andersen**  
**Lieutenant, United States Coast Guard**  
**B.A., United States Coast Guard Academy**

**Submitted in partial fulfillment  
of the requirements for the degree of**

**MASTER OF SCIENCE IN PHYSICS**

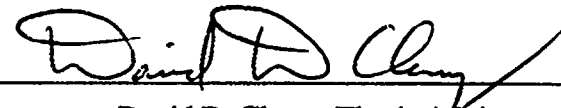
from the


**NAVAL POSTGRADUATE SCHOOL**  
**September 1990**


Author:

  
\_\_\_\_\_  
Carl K. Andersen

Approved by:

  
\_\_\_\_\_  
David D. Cleary, Thesis Advisor

  
\_\_\_\_\_  
Suntharalingam Gnanalingam, Second Reader

  
\_\_\_\_\_  
Karlheinz E. Woehler, Chairman, Department of Physics

## ABSTRACT

The MUSTANG instrument was calibrated using standard techniques to determine the sensitivity and wavelength calibrations and field of view. The instrument was launched aboard a NASA sounding rocket on March 30, 1990. Post-flight tests indicated that the calibration did not change as a result of the rocket experiment. Ultraviolet dayglow spectra of the Earth's ionosphere were obtained from approximately 100 km to 320 km in altitude over a wavelength range of 1800 Å to 3400 Å. The spectra were divided into 512 pixels of approximately 3.134 Å per pixel. Analyses of the data from 2420 Å to 2490 Å and from 2920 Å to 2972 Å were conducted to obtain the intensity profiles of the OII 2470.4 Å multiplet and the OI 2972.3 Å line emission, respectively. The intensity profile of the OII 2470.4 Å multiplet was found to have a broad peak of 1.6 kR centered at approximately 250 km. The intensity profile of the OI 2972.3 Å line emission shows a general trend of decreasing intensity with altitude. The maximum intensity of 3.6 kR was found at 105 km and the minimum of 137 R at 315 km. A partial layer, with an intensity of 4.1 kR, was evident near 180 km.



Accession For	
NTIS GRA&I	<input checked="checked" type="checkbox"/>
DTIC TAB	<input type="checkbox"/>
Unannounced	<input type="checkbox"/>
Justification	
By	
Distribution/	
Availability Codes	
Dist	Avail and/or Special
A-1	

## TABLE OF CONTENTS

I. INTRODUCTION .....	1
A. THESIS OBJECTIVES .....	2
B. THESIS OUTLINE .....	3
II. BACKGROUND .....	4
A. THE ATMOSPHERE .....	4
1. General Description .....	4
2. The Ionosphere .....	6
3. Atmospheric Airglow .....	8
B. ATOMIC AND DIATOMIC MOLECULAR SPECTRA .....	10
1. Introduction .....	10
2. Atomic Emissions .....	10
3. Diatomic Molecular Spectra .....	12
C. GENERATION OF SYNTHETIC SPECTRA .....	13
III. THE EXPERIMENT .....	16
A. INTRODUCTION .....	16
B. INSTRUMENT DESCRIPTION .....	17
C. DATA COLLECTION .....	20
IV. CALIBRATION .....	21
A. INTRODUCTION .....	21
B. CALIBRATION PROCESS .....	21
1. Sensitivity Calibration .....	21
2. Wavelength Calibration .....	48
3. Field of View Calibration ... ..	52

V. DATA ANALYSIS .....	55
A. INTRODUCTION .....	55
B. APPLICATION OF SYNTHETIC SPECTRA.....	56
C. THE OI 2972 Å LINE EMISSION .....	58
D. THE OII 2470 Å MULTIPLET .....	64
E. DISCUSSION .....	71
VI. CONCLUSION .....	78
A. INTRODUCTION .....	78
B. SUMMARY OF FINDINGS .....	78
C. RECOMMENDATIONS FOR FURTHER RESEARCH .....	79
APPENDIX .....	81
BIBLIOGRAPHY .....	108
INITIAL DISTRIBUTION LIST .....	110

## LIST OF FIGURES

Figure 2-1:	Temperature Profile of the Atmosphere (Banks and Kockarts, 1973) .....	5
Figure 2-2:	Ionospheric Electron Density .....	7
Figure 2-3:	Energy Curves of a Diatomic Molecule (Eisberg and Resnick, 1985) .....	14
Figure 3-1:	Schematic Diagram of MUSTANG Instrument .....	17
Figure 3-2:	Block Diagram of Image Intensifier .....	19
Figure 4-1:	Sensitivity Curve of the MUSTANG Instrument .....	23
Figure 4-2:	Calibration Geometry .....	24
Figure 4-3:	Calibration Parameter for the MUSTANG Instrument .....	31
Figure 4-4:	Irradiance From Deuterium Lamp at 50 cm .....	34
Figure 4-5:	Irradiance From FEL-IR Tungsten Filament Lamp at 50 cm .....	35
Figure 4-6:	Reflectance of BaSO <sub>4</sub> Coated Screen versus Wavelength .....	38
Figure 4-7:	Lambertian Properties of Diffusive Screen .....	41
Figure 4-8:	Linearity of MUSTANG Instrument Response .....	45
Figure 4-9:	Time Dependence of MUSTANG Instrument Response .....	47
Figure 4-10:	Platinum Hollow Cathode Lamp Spectrum .....	50
Figure 4-11:	Wavelength versus Pixel Position of 23 Selected Emissions .....	51
Figure 4-12:	Vertical FOV for MUSTANG Instrument .....	54
Figure 5-1:	Ultraviolet Dayglow Spectrum Measured at 155 km (down leg) .....	56
Figure 5-2:	Fit of Synthetic Spectra to 2972 Å Feature - 195 km (up leg) .....	59
Figure 5-3:	Intensity Profile of OI 2972 Å Line Emission .....	61
Figure 5-4:	Intensity Profile of N <sub>2</sub> VK (0-7) Band .....	62
Figure 5-5:	Comparison of Inferred and Predicted Temperature Profiles .....	63
Figure 5-6:	Fit of Synthetic Spectra to 2470 Å Feature - 155 km (down leg) .....	65
Figure 5-7:	Intensity Profile of OII 2470 Å Multiplet .....	66

Figure 5-8: Intensity Profile of N <sub>2</sub> VK (0-4) Band .....	68
Figure 5-9: Column Density Profile of NO .....	69
Figure 5-10: Comparison of NO Column Densities with Clayton (1990) .....	70
Figure 5-11: Comparison of 2472 Å Feature as Received with Instrument Slit Function - 155 km (down leg).....	73
Figure 5-12: Comparison of 2472 Å Feature Corrected for Known Data Dropout with Instrument Slit Function - 155 km (down leg).....	74
Figure 5-13: Comparison of 2472 Å Feature Corrected for Known and Additional Data Dropouts with Instrument Slit Function - 155 km (down leg) .....	75





## I. INTRODUCTION

The experiment presented in this paper is part of an ongoing effort to develop a practical method of measuring the Earth's ionospheric electron density profile on a global basis. The electromagnetic properties of the ionosphere are a result of the electron density, which varies with time, altitude, and geographic position. A plot of the electron density versus altitude for a given time and location is known as a density profile. Electron density profiles are currently measured by about 20 ground-based ionosonde stations. While the measurements are considered highly accurate, their geographic coverage is extremely limited. Generating a global map of the ionospheric electron density from these twenty sites has obvious difficulties and a large inherent uncertainty.

Beyond a purely scientific curiosity there are several defense applications which require knowledge of the electron density profile. Among these are high frequency (HF) radio communications, over-the-horizon (OTH) radar, Ballistic Missile Early Warning Systems (BMEWS) and the Ground Wave Emergency Network (GWEN). Accordingly, the Joint Chiefs of Staff prioritized the measurement of the Earth's ionospheric electron density as number five of 50 critical global parameters for inclusion in a defense environmental satellite (MJCS 154-86 dated March 21, 1986).

The solution for providing true global coverage would appear to lie with a satellite system. However, at present satellite-based ionosondes are unfeasible due to their size and power requirements. Development of a passive technique of measuring the electron density is necessary to take advantage of the global coverage offered by a satellite system.

Measurement of the natural ultraviolet emissions from the Earth's ionosphere is a passive technique which theoretically may be used to infer the electron density. Scientists at the Naval Research Laboratory (NRL) are actively involved in developing a methodology using observations of the OI 834 Å emission to measure the density of  $O^+$  (Anderson and

Meier, 1985; McCoy et al., 1985; Cleary et al., 1987). Above approximately 200 km  $O^+$  is the major positive ion in the atmosphere. If the concentration of positive ions is known then it is possible to deduce the electron density from the fact that the ionosphere is electrically neutral. Below 200 km  $O_2^+$  and  $NO^+$  become the major ions and the NRL measurements cannot be relied on (Cleary et al., 1989).

Work at the Naval Postgraduate School (NPS) suggests that the  $O_2^+$  and  $NO^+$  densities in the region from 100 km to 200 km in altitude may be deduced through measurement of emissions from the neutral atmospheric constituents (Bosserman, 1989; Danczyk, 1989). The electron density would then be inferred from the calculated ion densities.

A joint NRL/NPS rocket experiment was flown aboard a NASA sounding rocket to test these theoretical methods for inferring the ionospheric electron density. The Air Force Geophysics Laboratory conducted a simultaneous ground-based Ionospheric DigiSonde measurement for comparison with the experimental results.

The NRL instrument is based on a 0.5 meter Rowland Circle Spectrograph with an Electrographic Detector. It is designated the High Resolution Airglow and Aurora Spectrograph (HIRAAS). The NPS instrument is based on a 1/8th meter Ebert-Fastie Spectrograph with a photodiode detector. It is designated the Middle Ultraviolet Spectrograph (MUSTANG).

## A. THESIS OBJECTIVES

The work outlined in this paper has two main goals; calibration of the MUSTANG instrument and calculation of the intensity profiles for the  $OII$  2470.4Å multiplet and the  $OI$  2972.3Å line emission from data collected during the rocket experiment. An accurate calibration is required to permit analysis of experimental data in order to provide a context for comparison with previous measurements and theoretical models. The intensity profiles

for the OII 2470.4Å multiplet and the OI 2972.3Å line emission are obtained by an analysis of 25 averaged spectra which were collected over an altitude range of 100 km to 320 km by the MUSTANG instrument.

## **B. THESIS OUTLINE**

The thesis is divided into six chapters and has one appendix. Chapter II gives some general background information relevant to this work, including a brief description of the Earth's atmosphere and atmospheric airglow, a review of atomic emissions and diatomic molecular spectra, and the generation of sythetic spectra.

Chapter III describes the experiment and the MUSTANG instrument. The data collection process is also explained.

In Chapter IV the calibration of the MUSTANG instrument is presented. The procedures followed in the process, and the results of the various calibration tests are discussed.

Analysis of the data is performed in Chapter V. Each of the 25 spectra are broken-down into two smaller wavelength regions for individual analysis of the OII 2470.4Å multiplet and the OI 2972.3Å line emissions. A self-correlation is performed by comparing the results obtained for the two wavelength regions. Finally, a comparison is made with results obtained by Clayton (1990) for the column density profile of NO.

Chapter VI concludes this paper with a summary of the findings. In particular, the significantly high (kinetic) temperatures deduced for 105 km and 115 km are discussed. Suggestions for further research are also made.

The data and the best fits produced with the synthetic spectra are presented in the appendix.

## II. BACKGROUND

### A. THE ATMOSPHERE

#### 1. General Description

The Earth's atmosphere is a dynamic system, driven by the solar flux and constrained by gravity. The balancing of these forces leads to a partial stratification, wherein the pressure, temperature, density and chemical composition of the atmosphere vary with altitude. This stratification is primarily described in two ways; by the temperature gradient or by the chemical composition. The comparison of any one of these parameters with altitude is known as a profile. Figure 2-1 shows the general temperature profile for the Earth's atmosphere.

The temperature profile is used to divide the atmosphere into four major regions, in which the dynamics of the system will vary. The *troposphere* is the lowest of these regions, beginning at the Earth's surface and continuing up to an altitude of approximately 18 km at the equator and 8 km at the poles. This region acts as a heat engine, absorbing visible sunlight and developing convective currents. It is characterized by a negative temperature gradient. Above the *tropopause* lies the second atmospheric region known as the *stratosphere*. Trace amounts of O<sub>3</sub> are formed in this region. Due to the ability of O<sub>3</sub> to absorb both ultraviolet and infrared radiation this region is marked with a positive temperature gradient. The stratosphere extends up to approximately 50 km. Above the *stratopause* there is a decline in O<sub>3</sub> production. This factor, coupled with an increase in the loss into space of infrared emission by CO<sub>2</sub>, reestablishes the negative temperature gradient in the *mesosphere*. Above the *mesopause*, at approximately 85 km, begins the final region of the atmosphere, the *thermosphere*. In this region the temperature again increases with increasing altitude, to values above 1000 K. This is due to the absorption of ultraviolet radiation and ionization of the constituent gases. A balance is again achieved as the

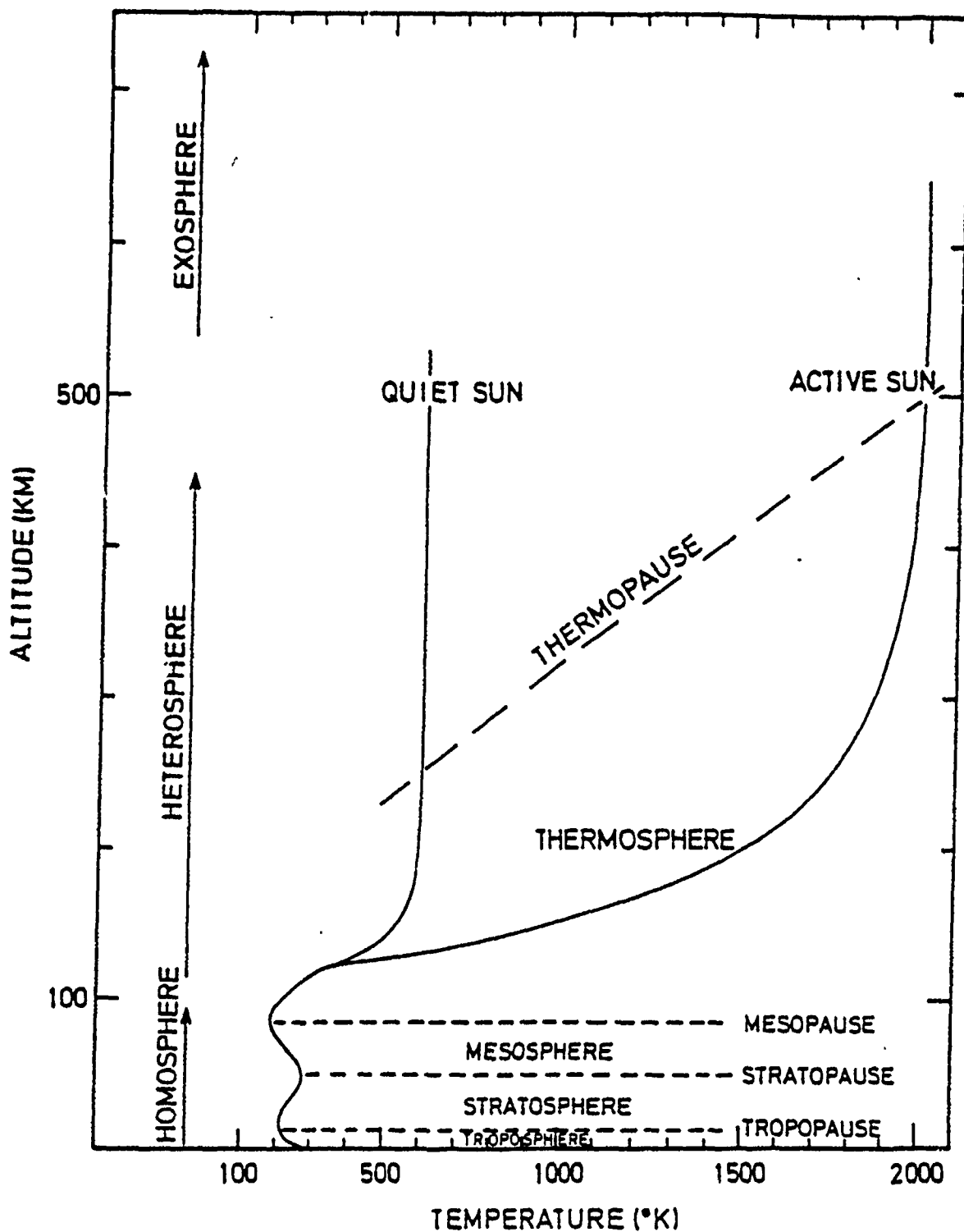


Figure 2-1: Temperature profile for the Earth's atmosphere showing division of atmosphere into different regions (Banks and Kockarts, 1973).

concentration of gases falls off. The *thermopause* describes the altitude above which the temperature is fairly constant. The altitude of the thermopause and the maximum temperature varies with solar activity.

Division of the atmosphere by chemical composition leads to two major regions. The *homosphere* encompasses that altitude region where the mean molecular composition of the atmosphere does not change. This uniform composition is brought about by convective mixing. The three lowest temperature regions generally lie within the homosphere. The upper limit of the homosphere is defined by the *turbopause*, at approximately 100 km. Above the turbopause is the *heterosphere*, which is marked by molecular diffusion rather than convective mixing. In this region the distribution of atmospheric constituents changes with altitude.

Since the overall density of the atmosphere falls off exponentially with altitude, there is no clear division between the Earth's atmosphere and space. A region known as the *exosphere*, marked by extremely low molecular densities (primarily of He and H), describes the region from approximately 500 km and extending out to infinity.

## 2. The Ionosphere

The *ionosphere* is defined as that portion of the atmosphere where the density of ions and electrons is sufficiently large to affect radiowave propagation. It is subdivided into three layers, the D, E and F regions, based on the electron density profile. The ionosphere is formed by the ionization of atmospheric constituents, primarily by solar x-rays and ultraviolet radiation. The amount of solar activity in the 10.7 cm band has been correlated to the intensity of the sun's emissions in the ultraviolet region, and is reported as the F10.7 number.

As the ionosphere straddles several of the temperature regions described above, the varying mechanisms of transport of the atmospheric constituents plays a key role in the

determination of which ions will dominate in the different ionospheric layers. Figure 2-2 shows the break down of the ionosphere, and the dominant ions in each region.

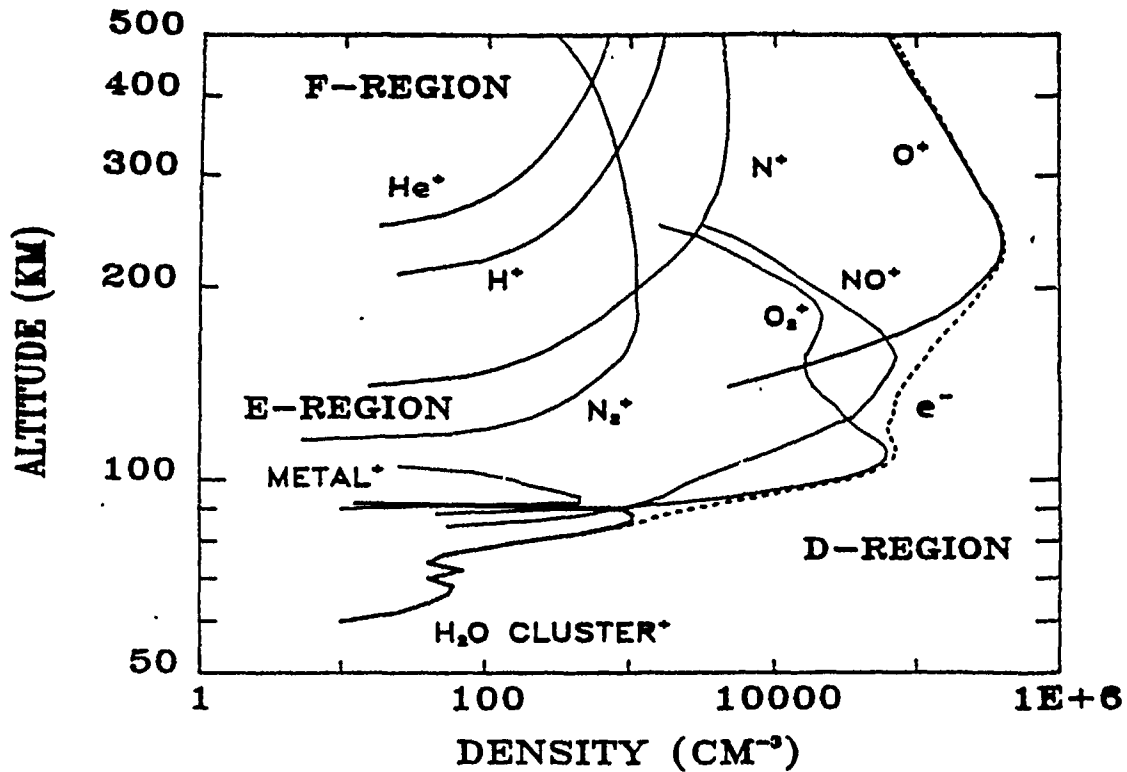


Figure 2-2: The electron density profile of the Earth's Ionosphere; with contributions by positive ions

The D region, ranging from about 50 km to 90 km in altitude, is the lowest layer of the ionosphere. Ionization is primarily due to absorption of solar Lyman- $\alpha$  radiation (1216 Å) by NO, and of x-rays by the other atmospheric constituents. This layer generally disappears at night due to ion/electron recombination.

The E region lies between 90 km and 140 km. Ionization is primarily due to the absorption of extreme ultraviolet (EUV) and soft x-rays by  $\text{O}_2$  and O in the lower portion of the layer, and absorption of far ultraviolet (FUV) by  $\text{O}_2$  and O in the upper portion. The



dominant ions in this layer are  $\text{NO}^+$  and  $\text{O}_2^+$ .  $\text{NO}^+$  is primarily formed by ion/atom exchange between  $\text{O}^+$  and  $\text{N}_2$  and by charge transfer between  $\text{O}_2^+$  and  $\text{NO}$ . The density of  $\text{O}^+$  increases rapidly near the top of this layer and is the dominant ion in the F region.

The F region is further divided into the F<sub>1</sub> and F<sub>2</sub> layers, with the F<sub>1</sub> layer ranging from 140 km to 200 km. The F<sub>1</sub> and F<sub>2</sub> layers are dominated by absorption of EUV by O. The F<sub>1</sub> layer disappears at night while the F<sub>2</sub> layer, partially sustained by energetic particle bombardment, persists.

Above the peak of the F<sub>2</sub> layer, at approximately 400 km, is a region commonly referred to as the *topside ionosphere*. As the altitude increases the dominant ion changes from  $\text{O}^+$  to  $\text{He}^+$  and finally to  $\text{H}^+$  in this region.

The density of ions and electrons in the ionosphere, although sufficient to affect radiowave propagation, is still less than one-tenth of one percent that of the neutral species. A photochemical model of the ionosphere developed by Cleary (1985) shows how the neutral species  $\text{N}_2$ ,  $\text{O}_2$ , O, NO, and N are chemically coupled with  $\text{O}_2^+$  and  $\text{NO}^+$ . It is this model which provides the framework wherein the electron density will be inferred by the NPS experiment. The process involves measuring the densities of the neutral species from the atmospheric airglow, allowing deduction of the  $\text{O}_2^+$  and  $\text{NO}^+$  densities. These, in turn, provide the basis to infer the electron density.

### 3. Atmospheric Airglow

The Earth's atmosphere emits radiation as a result of energy absorbed from the solar flux and energetic particle bombardment. Emissions during the daylight hours, dayglow, are produced from excited states achieved by chemical reactions as well as by solar photons and energetic particle bombardment. Nightglow is primarily driven by stored energy in the form of ion/electron recombination. In the absence of the solar flux the

electron concentrations in the ionosphere drops rapidly; so much so that the D and F<sub>1</sub> layers effectively disappear.

Photo-excitation will follow the selection rules of quantum physics, leading to allowed transitions from the ground state. Collisional excitation, by photo-electrons, and the transfer of energy through chemical reactions may lead to any excited upper state being achieved. The excitation energy will be reradiated at some rate determined by the lifetime of the upper state. The lifetimes of states with allowed transitions to the ground state are extremely short. If the upper state must undergo a forbidden transition to the ground state it may persist for some time (several seconds in extreme cases) and is said to be metastable.

Knowledge of the emission rate from an excited state may be used to calculate the density of a particular species if the excitation mechanism is understood. Due to the geometry of atmospheric observations, a column emission rate is the natural quantity measured. A number of techniques are available to convert column emission rates to volume emission rates. The radiometric unit for a column emission rate is known as the Rayleigh (R). It is defined as the rate of omnidirectional emission in a column of unit cross section along the line of sight, with dimensions of  $10^5 \text{ photons cm}^{-2} \text{ sec}^{-1}$ , and describes the number of photons emitted over an entire spectral feature. The column emission rate for isotropic emissions is given by;

$$4\pi I = \int_{z_0}^{\infty} E(z) dz ; \quad (2-1)$$

where  $4\pi I$  is the column emission rate in Rayleighs and  $E$  is the volume emission rate at altitude  $z$  in units of  $10^6 \text{ ph cm}^{-3} \text{ sec}^{-1}$ . For continuum emission (and broad spectral features) the spectral photon flux  $4\pi I$  in units of  $R/\text{\AA}$  is used. A thorough discussion of the derivation of the Rayleigh is given by Chamberlain (1978).

## B. ATOMIC AND DIATOMIC MOLECULAR SPECTRA

### 1. Introduction

The atmosphere consists predominantly of atoms and diatomic molecules with the majority of its mass made up of  $N_2$ ,  $O_2$  and  $O$ . Emissions in the middle ultraviolet regime from atoms and diatomic molecules are primarily the result of transitions of *optically active electrons* from an upper excited state to the ground state. This section provides a brief explanation of the differences between the spectra observed from these two types of atmospheric constituents. Herzberg (1950) provides a very thorough discussion of atomic and diatomic molecular spectra.

### 2. Atomic Emissions

The classic model of the atom is that of a positively charged nucleus surrounded by electrons in concentric orbits or shells. This model, first postulated by Neils Bohr, defines the energy state of the atom by the orbital levels of the electrons; with only specific energy states allowable. These discrete energy states are known as *stationary states*, which are determined by the *quantum conditions* of the electrons.

The derivation of the possible electron configurations of an atom is altered in quantum mechanics, but still results in discrete stationary states. Quantum mechanics is based on the theory that all matter has a wave nature as well as a particle nature. Thus, an atomic system is defined by an equation combining the wave motions of all the particles making up that system. This wave equation has only a finite number of solutions. These solutions are known as *eigenfunctions*. Associated with these solutions are specific energy values for the system, known as the *eigenvalues*. The terms which comprise a solvable equation make up an *eigenstate*, which are the allowable stationary states of the atom. The stationary states are described by the various *quantum numbers* of the electrons. An additional postulate required for determining the possible eigenstates of an atom is the Pauli

exclusion principle which states that in the same atomic system no two electrons can have the exact same quantum numbers.

An optically active electron, one in the outermost unfilled shell, may be excited and move into a higher energy state under the influence of electromagnetic radiation (photo-excitation) or by collision with a high energy particle. The process of excitation involves a transfer of energy to the electron and a change in its quantum numbers. When the electron returns to its ground state that energy will be emitted as a photon. Since eigenstates have discrete energy values, the energy of the emitted photons will have discrete values equal to the difference between the eigenvalues of the two eigenstates involved in the transition. The frequency of the photon is determined by the relationship  $E=h\nu$ ; where  $E$  is the energy of the photon,  $h$  is Planck's constant and  $\nu$  is the frequency. The wave-length is found by the relationship  $c = \nu\lambda$ ; where  $c$  is the phase speed of the radiation (speed of light) and  $\lambda$  is the wavelength.

The probability that an electron will undergo a transition from one state to another under photo-excitation is determined by the eigenfunctions. This defines the relative intensities of the various emission (or absorption) lines of the system. Only specific changes in the quantum numbers are allowable. This results in a series of *selection rules* for electron transitions. Interaction between an electromagnetic field and the magnetic dipole or electric quadrupole of the electron may also result in a transition. The probabilities of such transitions are much lower than electric dipole transition probabilities. Therefore, transitions which cannot occur with dipole radiation are considered *forbidden transitions*.

The probability of collisional excitation of an electron is determined by the flux of the high energy particles and the effective cross section of the atom to particles at those energies. This cross section is a function of the energy level of the particles. Collisional

excitation may result in an electron transition to a state for which the subsequent downward transition is forbidden. As the probability of such a transition is low the electron may remain in the excited state for a relatively long period of time. The atom is said to be in a *metastable* state when this condition occurs.

A transition between two orbital levels involves a change to the primary quantum number,  $n$ , of the electron. This results in a relatively large change in the energy of the system. For a given orbital transition, changes in the secondary quantum numbers, which define the various angular momenta of the system, result in small differences in the emitted energy. The number of possible discrete energy levels in which an electron can reside for a given orbital is known as the *multiplicity* of the state. For a multiplicity of one, only a single transition is possible from the upper excited state to the ground state of the electron. This results in a line emission. When the multiplicity is greater than one the transition is made up of a *multiplet* of discrete lines.

### 3. Diatomic Molecular Spectra

A diatomic molecule has two modes of motion which do not occur for an atom. The first is a vibrational motion of the atoms relative to each other along the internuclear axis. Secondly, the molecule can rotate about its center of mass on the internuclear axis.

The vibrational motion of a diatomic molecule may be modeled as a harmonic oscillator. That is, the atoms move towards and away from each other along the internuclear axis in simple harmonic motion. Quantum mechanics again imposes specific vibrational eigenfunctions, with the result that only specific vibrational frequencies of the molecule are allowed. These frequencies are proportional to the energy of the vibrational state. A transition from one vibrational state to another thus requires a transfer of energy by absorption or emission of a photon or by collisional excitation/deexcitation. The

differences in energy between vibrational eigenstates are typically an order of magnitude smaller than the differences between electronic states.

The rotational motion is described in a simple model of the molecule called the rigid rotator. In this model the atomic masses are considered to be point-like and fastened at a set distance apart on a weightless rigid rod. The rotational eigenstates allowed by quantum mechanics have specific quantized values for the rotational energy and angular momenta of the molecule. The results are rotational spectra consisting of series of equally spaced line emissions. The energy of a photon emitted due to a change in rotational states is an order of magnitude smaller than that of a photon emitted by a vibrational transition.

A given electronic transition involves several vibrational transitions. Each of these vibrational transitions will, in turn, encompass a series of rotational transitions. The collection of rotational spectra about a given vibrational transition is known as a vibrational band. Figure 2-3 illustrates this relationship between the various components of a molecular transition.

### C. GENERATION OF SYNTHETIC SPECTRA

Synthetic spectra are generated based on the selection rules and probabilities governing the various band emissions for diatomic molecules. The selection rules will determine whether a specific transition is allowed, while the various transition probabilities governs the relative intensities between the various emission bands, and the individual vibrational-rotational lines within a band. The probability of a particular electronic transition occurring is based on its *oscillator strength*. The probabilities of the various vibrational transitions results in a branching ratio within each electronic state. These branching ratios are given by the Franck-Condon factors. Finally, the probability for a specific change of rotational state within a specific electronic and vibrational transition is determined by the Honl-London factors.

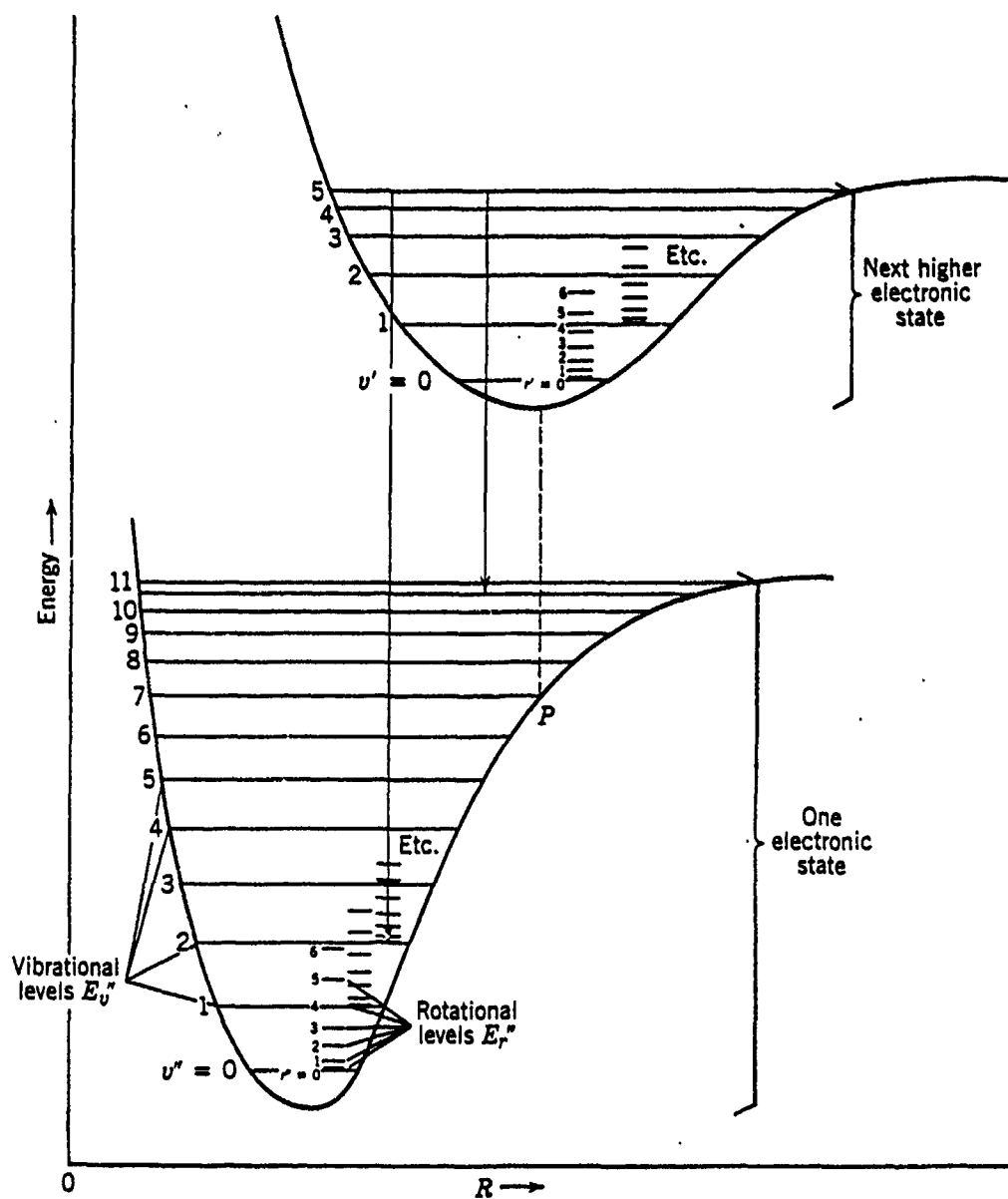


Figure 2-3: Molecular energy curves for two electronic states, illustrating the relationship between the electronic, vibrational and rotational levels. The energy difference between the vibrational and rotational states are not to scale. (Eisberg and Resnick, 1985)

All of these parameters are used to mathematically generate synthetic spectra. The emission rates are determined for each rotational line in a vibrational band of an electronic transition. The spectral region is divided into wavelength bins, and as each line is calculated its intensity is added to the appropriate bin. An algorithm of this type was developed by Cleary (1986) and is used in the analysis of the data presented in Chapter V.



### III. THE EXPERIMENT

#### A. INTRODUCTION

The objective of the experiment was to measure the atmospheric dayglow of the lower ionosphere. The payload consisted of the NRL spectrograph, designed to observe the 500Å to 1500Å wavelength region, and the NPS MUSTANG instrument, designed to observe the 1800Å to 3400Å wavelength region. The instruments were flown aboard a NASA Terrier Black Brandt sounding rocket, launched at White Sands Missile Range, New Mexico at 1700 GMT on 30 March, 1990. Observations are of mid-latitude atmospheric dayglow. The solar zenith angle was 62.9° and the F10.7 was 186.9.

The payload contained an internal attitude control system (ACS) which provided control of the instrument viewing direction. One minute after launch, at an altitude of approximately 140 km, the payload was despun and maneuvered so that the observation zenith angle (OZA) was 90° and the viewing direction was perpendicular to the solar direction. The payload maintained this orientation until it reached apogee at approximately 320 km. The payload was then rotated 270° along the transverse axis, until the OZA was 0°. This attitude was maintained down to an altitude of 200 km, at which time a final maneuver was performed resulting in an additional 90° transverse rotation. This resulted in a total transverse rotation of 360°, so that from 200 km down to the conclusion of data collection the payload was in the same orientation as during the ascent. Data collection was continued down to an altitude of approximately 100 km.

The spectra measured by the MUSTANG instrument are broken-down into two sets, the ascent (up leg) from 150 km to 320 km and the descent (down leg) from 200 km to 100 km.

## B. INSTRUMENT DESCRIPTION

The MUSTANG instrument consists of a 1/8th m off-axis telescope, a 1/8th m Ebert-Fastie spectrograph with a photo-detector system located at the exit focal plane and an electronics interface. The optical equipment was fabricated by Research Support Instruments, Inc. The electronics interface was designed and constructed at NPS (Campbell 1989). A diagram of the instrument is shown in Figure 3-1.

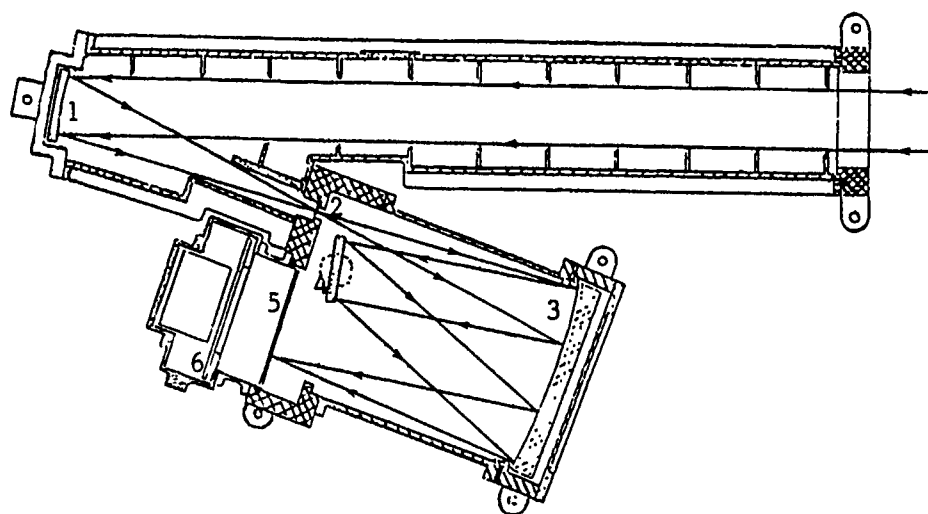


Figure 3-1 Schematic Diagram of MUSTANG Instrument. Major components are: (1) 1/8th m Telescope mirror, (2) Spectrograph entrance slit, (3) 1/8th m Ebert mirror, (4) Diffraction grating, (5) ITT Image intensifier, and (6) Hamamatsu Image detector.

The photo-detector system is comprised of an ITT F4145 Proximity Focused Channel Intensifier Tube with Dual Microchannel Plates and a HAMAMATSU S2300-512Q Plasma-Coupled Device (PCD) Linear Image Sensor mounted on a HAMAMATSU evaluation board.

The ITT device is an image intensifier consisting of a quartz input window, a cesium telluride (CsTe) photo-cathode, two microchannel plates (MCP) in cascade, a phosphor screen, and a fiberoptic output window. The HAMAMATSU device is a monolithic, self-scanning linear array of 512 p-n junction photodiodes, with 50  $\mu\text{m}$  center-to-center spacing and 5.0 mm height. It has a fiberoptic input window. The evaluation board is a driver/amplifier circuit for the image sensor. It provides a start pulse to initiate a scan of the array, a three phase clock to drive the scan sequentially, and a charge-amplifier for the photodiode output.

Incident light is collected by the telescope mirror and passed through the entrance slit of the spectrograph located at the focal point of both the telescope mirror and of the Ebert mirror. Collimated light from the Ebert mirror strikes a reflective diffraction grating and is reflected back to the Ebert mirror. The resulting diffraction pattern is focused by the Ebert mirror on the input window of the image intensifier, located at the exit focal plane of the spectrograph.

The telescope has a 1/8th m focal length off-axis parabolic mirror coated with aluminum with an overcoat of Magnesium Fluoride ( $\text{MgF}_2$ ). The Ebert mirror is also  $\text{MgF}_2$  coated aluminum. The entrance slit of the spectrograph has an area measuring 140  $\mu\text{m}$  by 5 mm. During the flight, the instrument was oriented with the 5 mm axis of the slit in the vertical direction. The diffraction grating, provided by HYPERFINE, has a linespacing of 1200 lines/mm and is blazed to optimize output of 2400  $\text{\AA}$  light in the first order. The resulting diffraction pattern has a bandwidth from 1800  $\text{\AA}$  to 3400  $\text{\AA}$  over the effective detector length of 25 mm.

The spectrum produced from the spectrograph strikes the photo-cathode at the exit focal plane and generates photo-electrons. These electrons are accelerated down the MCP by an accelerating voltage of approximately 1600 V. As the photo-electrons strike the walls

of the MCP secondary electrons are created, which are accelerated in turn generating still more secondary electrons in a cascade fashion. The result is approximately 15,000 electrons produced for every one emitted by the photo-cathode. The electrons are accelerated by an additional potential of approximately 5000V between the MCP and the phosphor screen. The phosphor fluoresces in response to the electron shower. The fluorescent light is transmitted by the fiberoptic window with the same spatial configuration as the original spectrum incident on the photo-cathode. A block diagram of the image intensifier is presented in Figure 3-2.

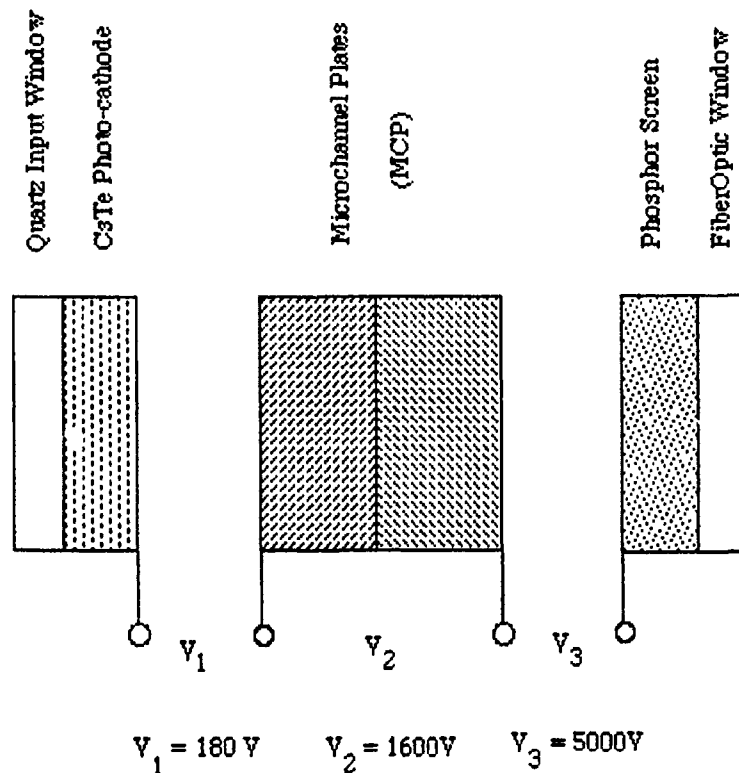


Figure 3-2 Block Diagram of ITT F4145 Proximity Focused Channel Intensifier Tube

The fiberoptic input window covering the photodiode surface of the image sensor is abutted to the output window of the image intensifier. Each of the photodiodes integrates charge over time as a function of the number of photons striking it. As the photodiode array is scanned the detector outputs an analog signal with a maximum value of 7.7V.

The electronics interface consists of an analog-to-digital (A-to-D) converter, a first-in-first-out data storage device (FIFO) and a buffer. The analog signal is sent to the A-to-I converter and the resulting digital data word is stored in the FIFO until it is ready to be read by telemetry. The data word is then sent to the buffer for acceptance into the data stream.

### C. DATA COLLECTION

Data collection and readout are controlled by NASA timing signals. Telemetry is broken down into frames of 1024 words, with 10 bits per word. At a bit rate of 200kHz this generates approximately 19.5 frames per second. Frames are comprised of 32 subframes of 32 words each, with NASA using the first 16 words of each subframe for command and control signals and general housekeeping. The remaining 16 words in each subframe are dedicated to the MUSTANG data. Therefore, data is transmitted in spurts of 16 words (pixels) per subframe resulting in transmission of one complete spectrum every 51.2 ms.

In the laboratory the MUSTANG instrument is driven by a Macintosh II equipped with NATIONAL INSTRUMENTS Direct Memory Access (DMA), Multi-function Input/Output (MIO) and Digital Input/Output (DIO) expansion cards. Timing signals and data acquisition are performed using the programming language 'LabVIEW' also by NATIONAL INSTRUMENTS. Power is provided to the instrument using a HEWLITT-PACKARD 6206B DC Power Supply. Data are acquired and saved on the computer with 50 individual spectra averaged together for each measurement.

## IV. CALIBRATION

### A. INTRODUCTION

In order to evaluate the data collected during the rocket flight it is first necessary to understand the following characteristics of the MUSTANG instrument:

1. The output from the detector resulting from a range of possible inputs;
2. The precise wavelength band striking each photodiode; and
3. The field of view for the instrument.

In the following sections the calibration steps followed to obtain these parameters are described in detail.

### B. CALIBRATION PROCESS

#### 1. Sensitivity Calibration:

##### *a. Overview*

The sensitivity calibration of the instrument was conducted by illuminating a diffusing screen with calibrated light sources and measuring the resulting response of the instrument. Because the primary interest of this experiment is in wavelengths longwards of 2000Å the calibration was performed in open air.

The sensitivity was determined by dividing the response of the detector by the product of the reflectance of the screen and the output from a light source. This was carried out by enclosing the calibrated source in a box with a controllable aperture and having the instrument view the reflective screen at an angle of approximately 40° from the normal of the screen. The normal of the screen was coincident with the optical axis of the source and the instrument was placed so that it was level with this axis. The laboratory was darkened and the aperture opened until the reflective screen was fully illuminated by the source. The screen was assumed to be an ideal Lambertian surface.

To effectively cover the bandwidth of the instrument two types of sources were used; an EG&G GAMMA SCIENTIFIC GS-5150 Deuterium Light Source and a tungsten filament quartz halogen lamp (FEL-IR) from OPTRONIC LABORATORIES. These sources are both traceable to the National Institute of Science and Technology (NIST). The sensitivity curves produced for the two sources match very closely from 2300 Å to 3100 Å. The response of the instrument to the FEL-IR source is considered most reliable for wavelengths from 2300 Å to 3400 Å, while the response to the Deuterium source is reliable for wavelengths from 2000 Å to 3100 Å. An overall sensitivity curve constructed from those regions of the two sensitivity curves is shown in Figure 4-1. The large dip in sensitivity at approximately 2370 Å, distinctly illustrated in Figure 4-1, is believed to be due to a blemish on the image intensifier.

#### ***b. Calibration Geometry***

The theory may be reviewed in a few simple steps. The following definitions will be used in this discussion:

$E_{\lambda}$  - spectral irradiance  $\left(\frac{\text{ph}}{\text{cm}^2 \text{ s } \text{Å}}\right)$  striking the screen;

$L_{\lambda}(\theta)$  - spectral radiance  $\left(\frac{\text{ph}}{\text{cm}^2 \text{ s } \text{Å} \text{ str}}\right)$  leaving the screen;

$P_{\lambda}$  - photon flux received over a one-Å wide wavelength bin  $\left(\frac{\text{ph}}{\text{s } \text{Å}}\right)$ ;

$A_t$  - area ( $\text{cm}^2$ ) of the telescope aperture;

$A_s$  - area ( $\text{cm}^2$ ) of the spectrograph entrance slit;

$A_v$  - area ( $\text{cm}^2$ ) of the screen viewed by the instrument;

$f$  - focal length (cm) of the off-axis telescope collecting mirror;

$d$  - distance (cm) from the mirror to the screen;

$\rho$  - relectance of the screen.

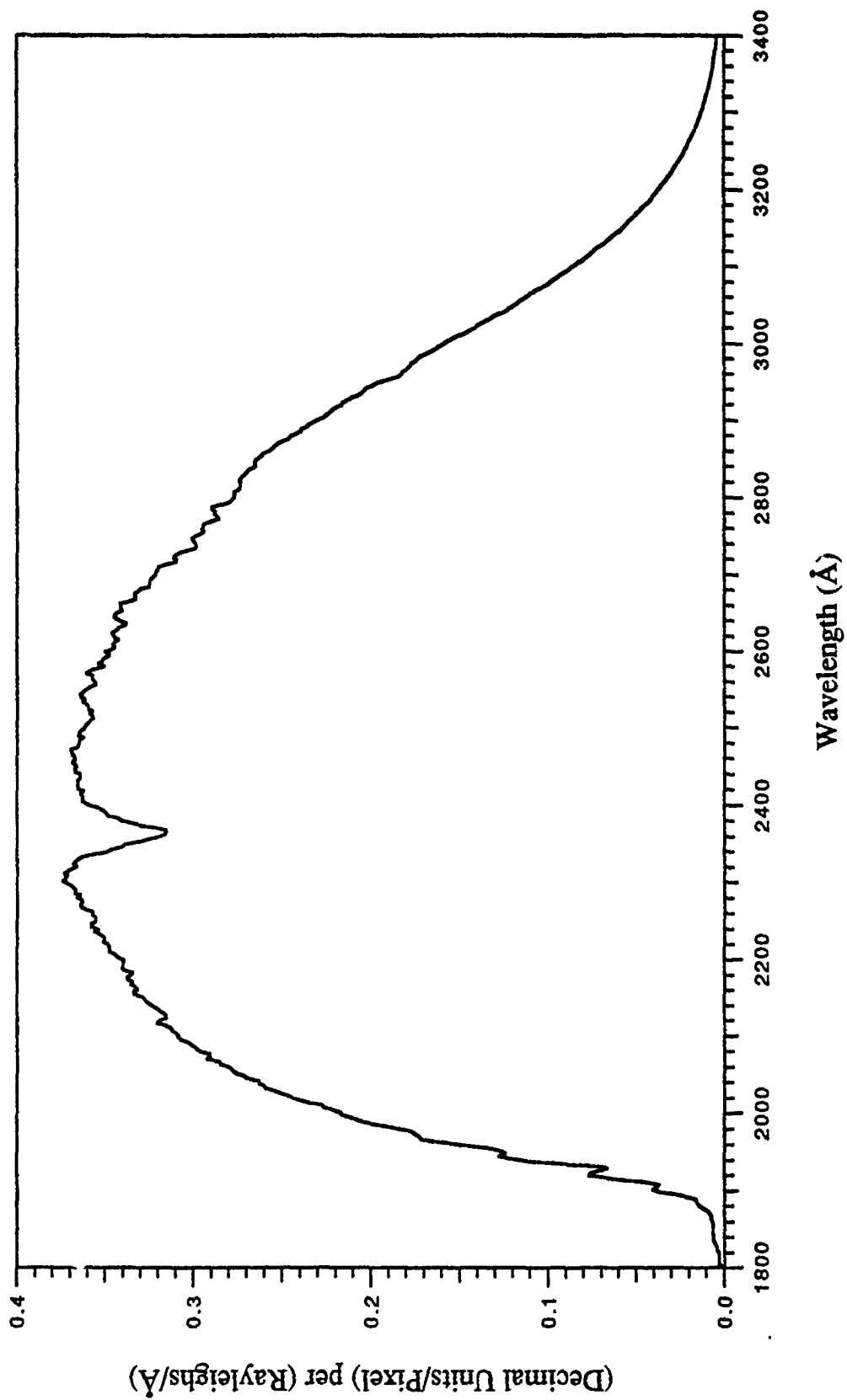


Figure 4-1: Sensitivity curve of the MUSTANG instrument.



For simplicity the  $\lambda$ -subscripts will be left off; spectral irradiance/radiance and photon flux will be implied unless otherwise stated.

The geometry of the calibration setup is shown in Figure 4-2. Geometric optics allows for the calculation of  $A_v$ , in the limit where the slit is narrow and  $d \gg f$ . The solid angle viewed by the telescope is:  $\Omega = (A_s/f^2)$ , with the area of the screen viewed by the slit given by:  $\frac{A_v \cos\theta}{d^2} = \Omega$ . Therefore:

$$A_v = A_s \left( \frac{d^2}{f^2} \right) \left( \frac{1}{\cos\theta} \right). \quad (4-1)$$

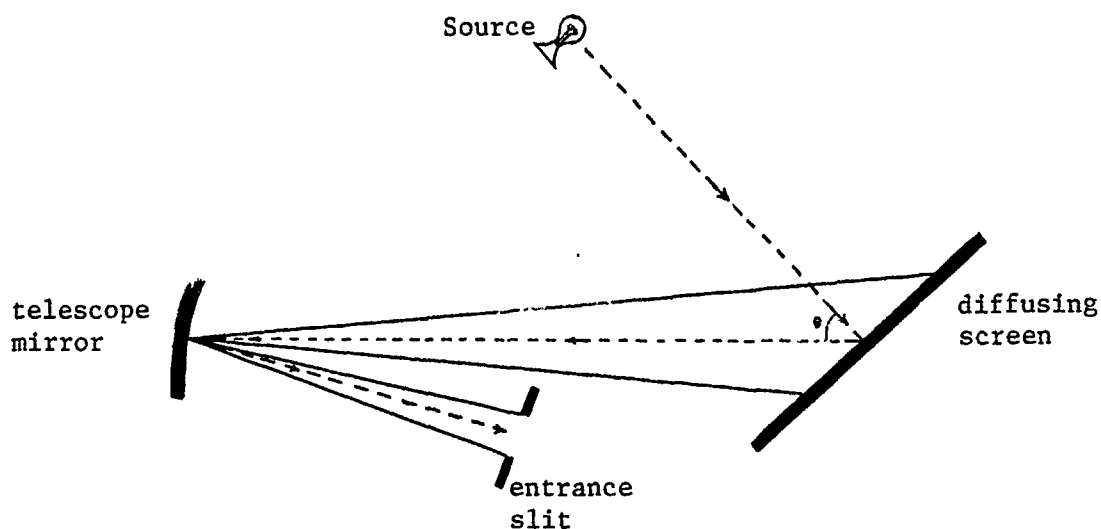


Figure 4-2: Schematic drawing of the calibration geometry; showing the area of the diffusive screen observed by the spectrograph.

Lambert's Law states that for an ideal diffuse reflector, or Lambertian surface, the radiance at an angle  $\theta$  from the normal of the screen is equal to the product of the irradiance at  $\theta = 0^\circ$  times the cosine of  $\theta$ :

$$L(\theta) = L_0 \cos\theta. \quad (4-2)$$

The solid angle subtended by the telescope aperture at each element of area ( $da$ ) on the screen is:  $\omega = (A_t/d^2)$ . Thus, the number of photons per second per Angstrom received at the telescope mirror due to an element of area is:  $dP = L(\theta) da \omega$ . Substituting for  $\omega$  yields:  $dP = L(\theta) (A_t/d^2) da$ . The total number of photons received at the entrance slit of the spectrograph from the reflecting screen may be calculated by integrating over the projected area of the slit on the screen. Ignoring reflective losses from the mirror, and assuming that  $L(\theta)$  is constant over the area in question:

$$P = L(\theta) \frac{A_t}{d^2} \int da. \quad (4-3)$$

Using the definition of the area viewed by the entrance slit this becomes;

$$P = L(\theta) \frac{A_t}{d^2} A_v. \quad (4-4)$$

Substituting for  $A_v$  yields:

$$P = L(\theta) \frac{A_t}{d^2} \left( A_s \frac{d^2}{f^2} \frac{1}{\cos\theta} \right). \quad (4-5)$$

Rearranging the terms and simplifying leaves:

$$P = \left( \frac{A_t A_s}{f^2} \right) \left( \frac{L(\theta)}{\cos\theta} \right). \quad (4-6)$$

For a Lambertian surface, where  $L(\theta) = L_0 \cos\theta$ ;

$$P = L_0 \left( \frac{A_t A_s}{f^2} \right). \quad (4-7)$$

Thus, the number of photons per second per Angstrom passing through the entrance slit of the spectrograph is a product of constants (for constant radiance) and is independent of  $\theta$ .

The spectral radiance of the screen is determined by equating the spectral irradiance striking the screen to the total spectral radiance leaving the screen divided by the reflectivity of the screen:

$$E = \frac{\int L(\theta) d\Omega}{\rho}; \quad (4-8)$$

where  $d\Omega = \sin\theta d\theta d\phi$ ,  $\theta$  ranges from 0 to  $\pi/2$ , and  $\phi$  ranges from 0 to  $2\pi$ . Assuming that the reflectance is independent of  $\theta$ , Equation 4-8 becomes;

$$E = \frac{1}{\rho} \int_{\phi=0}^{2\pi} \int_{\theta=0}^{\pi/2} (L_0 \cos\theta) \sin\theta d\theta d\phi. \quad (4-9)$$

The solution of this integral is:  $E = \pi L_0 / \rho$ . Therefore; the radiance normal to the screen is:

$$L_0 = \frac{\rho E}{\pi}; \quad (4-10)$$

and the directional spectral radiance is written as:

$$L(\theta) = \frac{\rho E}{\pi} \cos\theta. \quad (4-11)$$

Substituting Equation 4-10 into Equation 4-7 gives;

$$P = \left( \frac{A_t A_s}{\pi f^2} \right) \rho E. \quad (4-12)$$

### *c. Calibration Theory*

The output from the MUSTANG instrument is an array of 512 voltages which have undergone an A-toD conversion. These raw data have dimensions of decimal units per pixel. It is necessary to convert these values to a standard unit such as R/Å. This is done by equating the flux entering the spectrograph, P (see discussion in Section b above), to the instrument output, D, in decimal units per pixel. This relationship is;

$$D = P\Gamma B_w; \quad (4-13)$$

where  $\Gamma$  is the instrument gain in decimal units per photon per second, and  $B_w$  is the bandwidth of each pixel in Angstroms per pixel. The gain is the product of the various efficiencies and transfer functions of the individual components of the instrument. While it is not the objective of this thesis to determine the numerical value of  $\Gamma$ , it is helpful to demonstrate how it is derived. The following definitions will be used in this discussion:

$\eta_1$  - quantum efficiency  $\left(\frac{el}{ph}\right)$  of the photo-cathode;

$\Gamma_{mcp}$  - gain  $\left(\frac{el}{el}\right)$  of the microchannel plates;

$\eta_2$  - efficiency  $\left(\frac{ph}{el}\right)$  of the phosphor screen;

$\eta_3$  - quantum efficiency  $\left(\frac{el}{ph}\right)$  of the photodiode;

$\tau$  - integration time (sec);

$g_1$  - transfer function  $\left(\frac{V}{el}\right)$  of the image detector amplifier;

$g_2$  - transfer function  $\left(\frac{\text{decimal units}}{V}\right)$  of the analog to digital conversion.

Over one integration time, the output from a photodiode ( $W_{pd}$ ) will be;

$$W_{pd} = P (\eta_1 \Gamma_{mcp} \eta_2 \eta_3 \tau); \quad (4-14)$$

in electrons per Angstrom. During this same time period, the instrument output will be;

$$D = W_{pd} (g_1 g_2) B_w. \quad (4-15)$$

Recombining the terms, and separating out the flux entering the spectrograph leaves;

$$D = P (g_1 g_2 \eta_1 \Gamma_{mcp} \eta_2 \eta_3 \tau) B_w. \quad (4-16)$$

Therefore, the overall MUSTANG instrument gain,  $\Gamma$ , may be defined as;

$$\Gamma = (g_1 g_2 \eta_1 \Gamma_{mcp} \eta_2 \eta_3 \tau), \text{ and} \quad (4-17)$$

Substituting for the flux,  $P$ , gives;

$$D = \Gamma B_w \left( \frac{A_t A_s}{\pi f^2} \right) \rho E. \quad (4-18)$$

The constants in Equation 4-18 are gathered together to define a constant;

$$K = \Gamma B_w \left( \frac{A_t A_s}{\pi f^2} \right) \rho; \quad (4-19)$$

which allows the output of the instrument to be written as;

$$D = KE. \quad (4-20)$$

Given an omnidirectional emission rate from the atmosphere of  $4\pi I$  R/Å, (see Equation 2-1) the spectral radiance received by the MUSTANG instrument is;

$$L = \left( \frac{10^6 I}{4\pi} \right); \quad (4-21)$$

where L is in units of  $\left( \frac{\text{ph}}{\text{cm}^2 \text{ s Å str}} \right)$ . The spectral radiance may also be written in terms of the spectral irradiance of the atmosphere. For normal incidence this is;

$$L = E/\pi. \quad (4-22)$$

With omnidirectional emissions the instrument is at normal incidence to the atmospheric airglow. Therefore, the output of the instrument due to the spectral radiance received from the atmosphere is;

$$D = \Gamma B_w \left( \frac{A_t A_s}{f^2} \right) L. \quad (4-23)$$

This is rewritten in terms of the omnidirectional emission rate;

$$D = \Gamma B_w \left( \frac{A_t A_s}{f^2} \right) \left( \frac{10^6 I}{4\pi} \right). \quad (4-24)$$

Solving for the emission rate of the atmosphere gives;

$$I = \left( \frac{1}{10^6} \right) \left( \frac{4\pi f^2}{B_w \Gamma A_t A_s} \right) D; \quad (4-25)$$

where I is in units of R/Å.

A new constant is defined;

$$\zeta = \left( \frac{4\pi f^2}{10^6 B_w \Gamma A_t A_s} \right). \quad (4-26)$$

This is simplified by using the definition for K from Equation 4-19, which yields;

$$\zeta = \left( \frac{4\rho}{10^6 K} \right). \quad (4-27)$$

Substituting this constant into Equation 4-20, where E is the spectral irradiance from a calibration source, gives;

$$D = \left( \frac{4\rho}{10^6} \right) \left( \frac{E}{\zeta} \right). \quad (4-28)$$

The constant  $\zeta$  may then be defined in terms of the spectral irradiance and the response of the instrument as;

$$\zeta = \left( \frac{4\rho}{10^6} \right) \left( \frac{E}{D} \right); \quad (4-29)$$

under the assumption that the screen is an ideal Lambertian surface.

This results in a calibration parameter ( $\zeta$ ) for the MUSTANG instrument;

$$I = \zeta D; \quad (4-30)$$

where the spectral emission rate from the atmosphere is equal to the calibration parameter times the detector response.

Because the calibration below  $\sim 2000 \text{ \AA}$  is affected by absorption due to oxygen, no sensitivity is calculated in this region. The spectral calibration parameter, in  $(R/\text{\AA})$  per (Decimal unit/pixel), is presented in Figure 4-3.

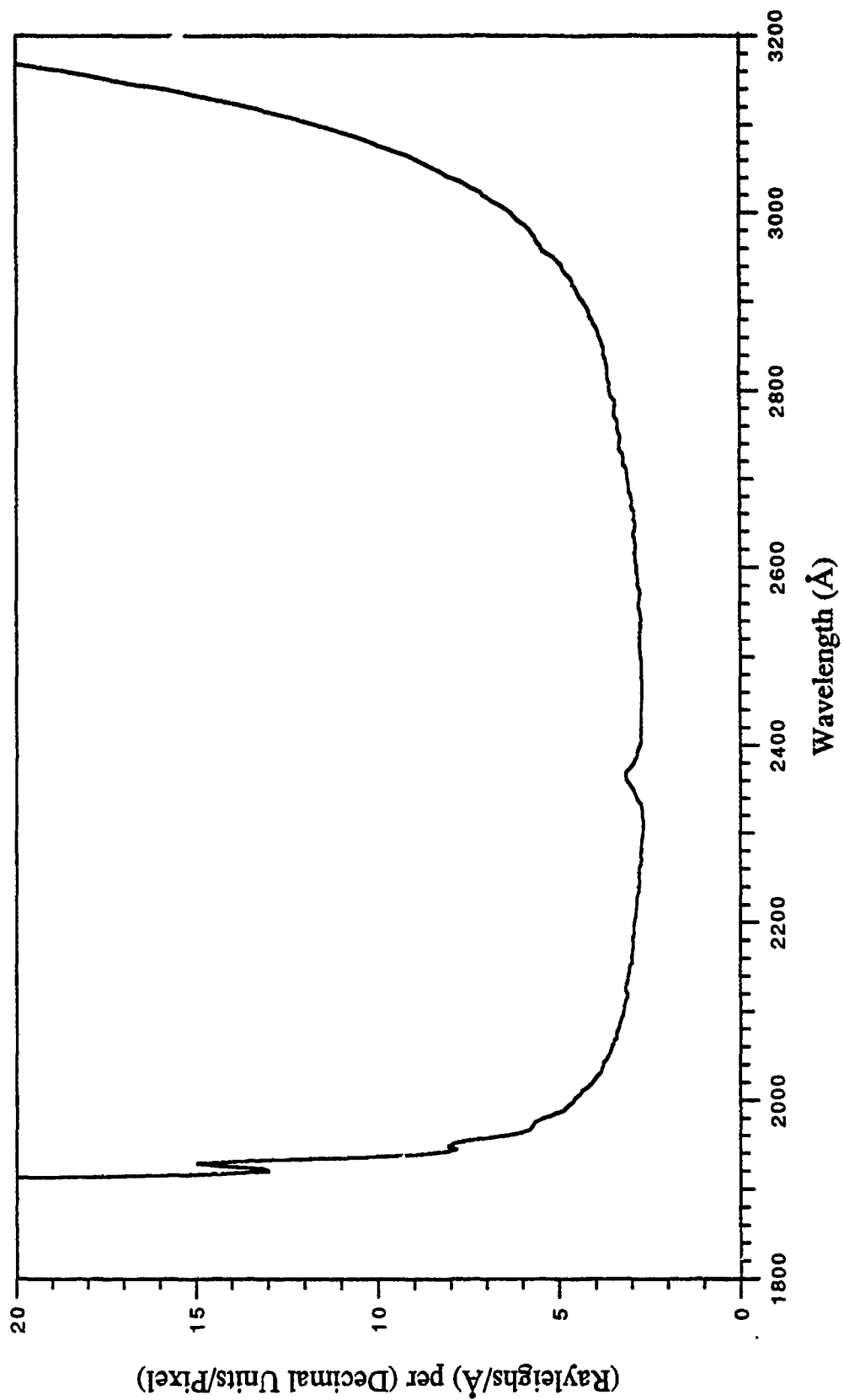


Figure 4-3: Calibration parameter for the MUSTANG data



**d. Output of calibration sources as a function of wavelength**

The calibration data provided by the manufacturers of the Deuterium Lamp and FEL-IR sources are in terms of spectral irradiance [ $\mu\text{W}/(\text{cm}^2 \text{ nm})$ ], provided at specific wavelengths. For the calibration the output was required as a continuous function of wavelength. The manufacturer's data are shown in Tables 4-1 and 4-2.

**TABLE 4-1**  
**IRRADIANCE FROM DEUTERIUM**  
**SOURCE AT 50 cm**

Wavelength (Å)	Irradiance $\left(\frac{\mu\text{W}}{\text{cm}^2 \text{ nm}}\right)$
2000	$5.2698 \times 10^{-2}$
2100	4.7427
2200	4.4895
2300	4.3975
2400	4.2214
2500	3.5706
2600	3.0351
2700	2.5182
2800	2.1528
2900	1.8548
3000	1.5673
3100	1.3508
3200	1.1693
3300	1.0341
3400	$9.1718 \times 10^{-3}$
3500	8.0237

**TABLE 4-2**  
**IRRADIANCE FROM FEL-IR**  
**SOURCE AT 50 cm**

Wavelength (Å)	Irradiance $\left(\frac{\mu\text{W}}{\text{cm}^2 \text{ nm}}\right)$
---	---
---	---
---	---
---	---
---	---
2600	$3.15 \times 10^{-2}$
2600	3.15
2700	5.22
2800	8.17
2900	$1.23 \times 10^{-1}$
3000	1.78
3100	2.50
3200	3.43
3300	4.58
3400	5.99
3500	7.69

The calibration procedure described above requires an irradiance for each wavelength bin of the detector. Therefore, the manufacturer's data were fitted with curves to produce a continuous function of output versus wavelength. Three separate curves were required for the Deuterium lamp; a gaussian distribution for the wavelength range from 1800 Å to 2100 Å, an exponential from 2100 Å to 2400 Å and a second exponential for wavelengths above 2400 Å. The equations for these curves are:

$$E_{\lambda}(1800 - 2100 \text{ \AA}) = 0.046 + 0.0092xe^{-(\lambda-1929)/115.0]^2}; \quad (4-31a)$$

$$E_{\lambda}(2100 - 2400 \text{ \AA}) = 0.041 + 103.3xe^{-(\lambda/217.2)}; \text{ and} \quad (4-31b)$$

$$E_{\lambda}(\lambda > 2400 \text{ \AA}) = 0.003 + 3.542xe^{-(\lambda/533.3)}; \quad (4-31c)$$

in  $[\mu W/(cm^2 \text{ nm})] \times 10^{-3}$ . The calibration data and the three curve fits for the Deuterium source are shown in Figure 4-4.

The FEL-IR source is advertised as a 'black-body' radiator with a color temperature of approximately 3000 K. A Planckian distribution was successfully fitted to the data with a calculated color temperature of 3081 K:

$$E_{\lambda} = \left( \frac{2.49 \times 10^{-27}}{\lambda^5} \right) \left( \frac{1}{e^{(4.67 \times 10^{-6}/\lambda)} - 1} \right); \quad (4-32)$$

in  $[\mu W/(cm^2 \text{ nm})]$ . The data and calculated Planckian distribution for the FEL-IR source is presented in Figure 4-5.

The calibration data for the sources were established for a radial distance of 50 cm. Due to the sensitivity of the detector the Deuterium lamp was normally set at a distance of 200 cm from the screen while the FEL-IR source was set at 300 cm. The output curves were modified by the ratios  $(50/\text{distance})^2$ . In addition, the output of the detector is determined by the number of photons which strike each photodiode over the data integration time, not by the energy flux. Therefore, the output of the two calibration sources was converted to a photon flux by dividing the fitting curves by the photon energy at each wavelength. This resulted in values of the irradiance in units of  $\left( \frac{\text{ph}}{cm^2 \text{ \AA}} \right)$ .

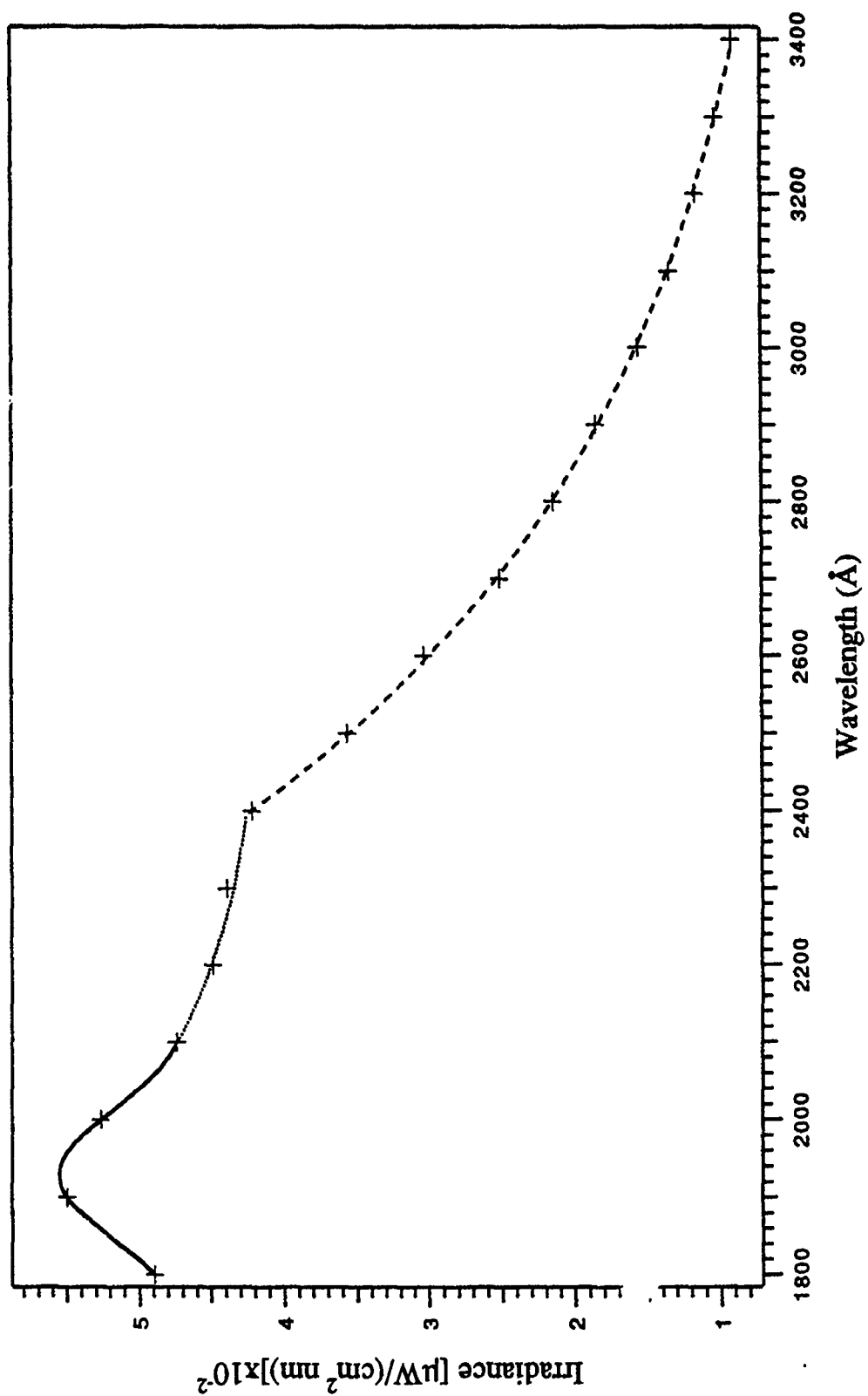


Figure 4-4: Irradiance from Deuterium lamp at 50 cm  
Three curves fitted to manufacturer's data

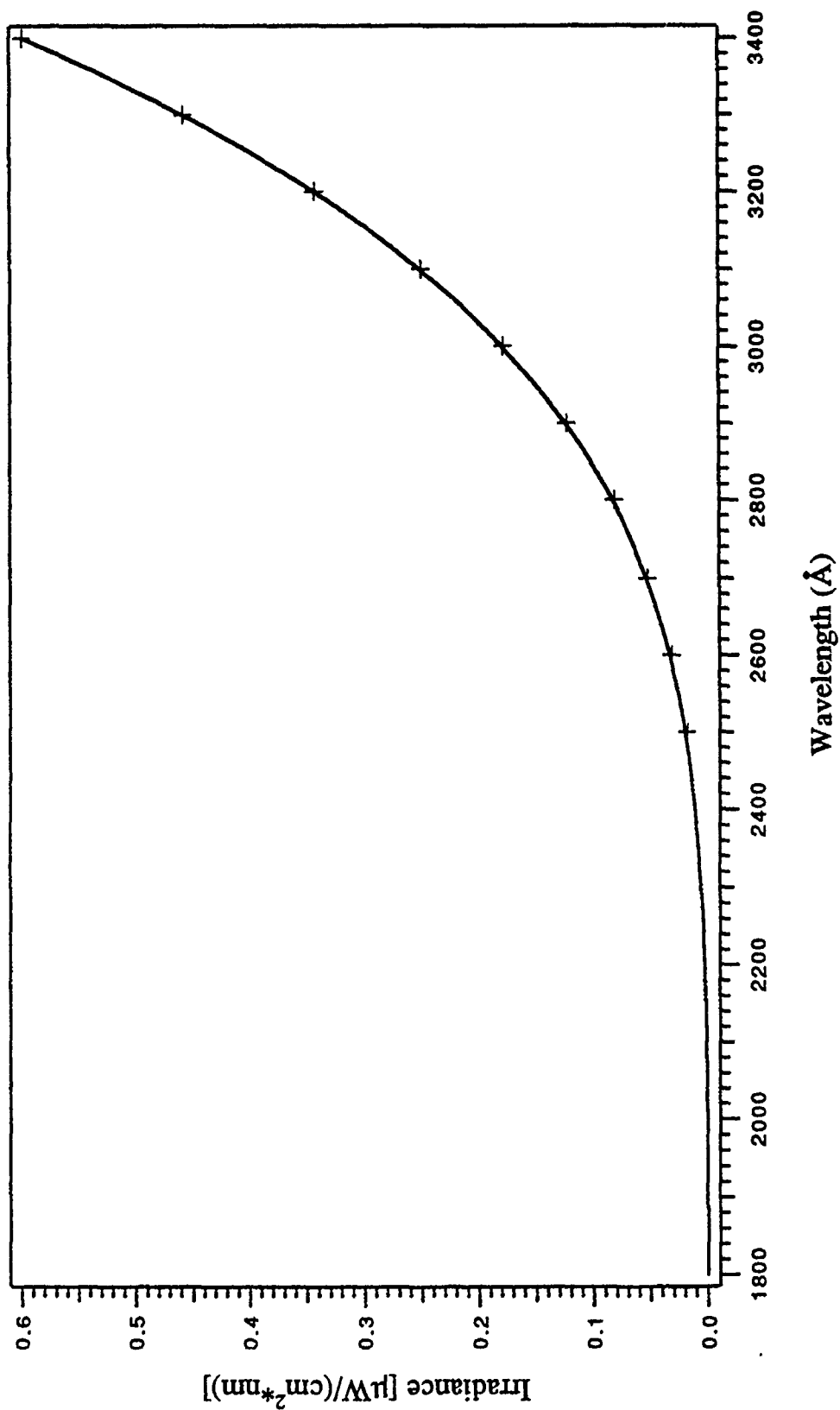


Figure 4-5: Irradiance from FEL-IR tungsten filament lamp at 50 cm.  
Planckian distribution fitted to manufacturer's data.

*e. Reflectivity of Screen as a Function of Wavelength*

During flight, the atmosphere appears to the instrument as an extended source. In order to mimic this situation a diffuse reflective screen is illuminated by a source while the MUSTANG instrument measures the flux over a small solid angle projected upon a portion of the screen.

The screen is constructed of a one-quarter inch thick sheet of aluminum, measuring one foot square, painted with KODAK Model 6080 White Reflectance Coating; a solution of Barium Sulfate ( $\text{BaSO}_4$ ) suspended in ethanol. The solution was applied using a KODAK Model 13270 Laboratory Sprayer (for high viscosity use). Ten coats were applied allowing the screen to air dry between coats.

To determine the reflectivity of the screen as a function of wavelength, the intensity measured by reflecting a source off the screen is compared to the intensity measured for direct illumination of the instrument. The ratio of these two measurements is calculated and normalized to a known value of the absolute reflectance of the  $\text{BaSO}_4$  coating. This provides a continuous curve of the reflectance as a function of wavelength.

Due to the sensitivity of the detector an extremely small aperture was required to reduce the irradiance sufficiently to allow the instrument to "look" directly at the sources. Even a small pinhole in a sheet of aluminum foil allowed too much light to reach the instrument. A suitable aperture was finally constructed by pricking a small hole in a strip of black tape placed over the controllable aperture in front of the source. The "self-healing" property of the tape caused the pinhole to shrink until useable data could be taken. (The hole would continue to shrink, until it was fully sealed and had to be reopened.) Five measurements were taken in this manner for each source. These measurements varied in intensity and were normalized prior to being averaged together.

Five measurements were also made with the instrument viewing the illuminated screen and the aperture fully open. These measurements were averaged together and the ratios of the reflected to direct measurements were calculated for each source. The resultant curve from the FEL-IR source was normalized to the curve produced by the Deuterium lamp using the ratio of their values at 2700 Å.

An overall reflectance curve for the screen was produced by combining the 1950 Å to 2700 Å section of the curve produced by the Deuterium lamp with the 2700 Å to 3200 Å section of the FEL-IR curve. It was normalized to the absolute reflectance of BaSO<sub>4</sub> at 3500 Å reported by Grum and Luckey (1968). An exponential function was fitted to this curve to produce a continuous function relating the reflectance and wavelength;

$$\rho = 0.989 - 21.29xe^{-(\lambda/448.5)} ; \quad (4-33)$$

where  $\lambda$  and the decay constants are in Å.

Figure 4-6 displays the actual reflectivity curve obtained for the screen, the exponential fit and the published values for the absolute reflectance of BaSO<sub>4</sub> (Grum and Luckey, 1968). The divergence of the data from the published values is probably due to the method of application. Spraying reportedly does not permit a sufficient thickness of BaSO<sub>4</sub> to be produced to achieve the reflectance values obtained with a 1.0 mm coating (Grum and Luckey 1968).

#### *f. Lambertian Properties of the Screen*

To test the Lambertian properties of the screen, the MUSTANG instrument was placed at several angles, ranging from 6° to 65°, from the normal to the screen. The ratios of the detector output for each angle  $\theta$  to that at 6° were plotted versus  $\theta$ . The 6° angle was the smallest which could be measured without the instrument interfering with the illumination of the screen and was assumed to be close enough to 0° for this purpose. For

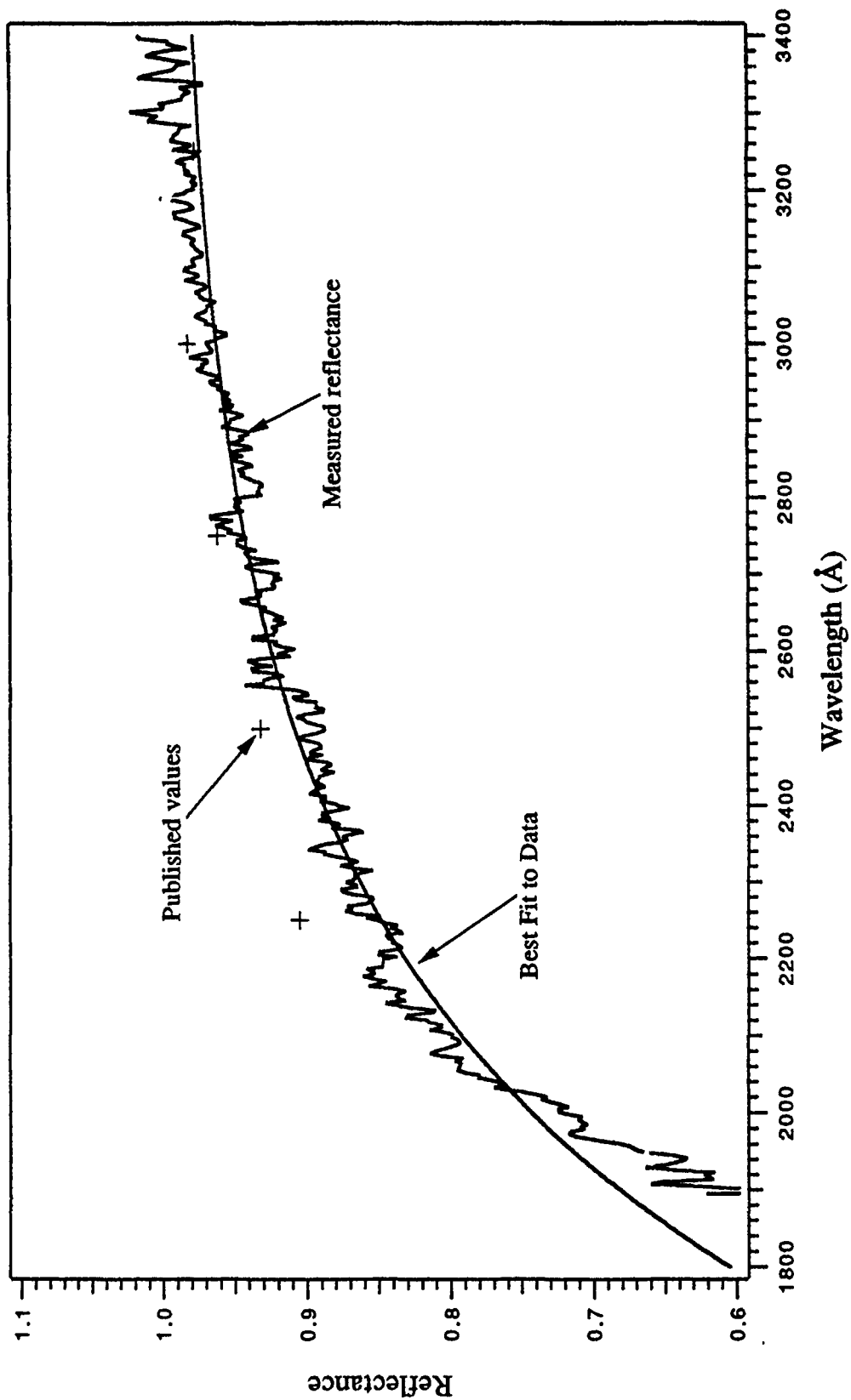


Figure 4-6: Reflectance of BaSO<sub>4</sub> coated screen versus wavelength. The experimentally measured curve, best fit and published values are displayed.

an ideal Lambertian surface this ratio will always be one. The actual data showed a decrease in the ratios with increasing  $\theta$ .

Angular dependence of the spectral radiance for a non-Lambertian screen will involve some function of  $\theta$  other than  $\cos\theta$ . Lambert's Law is modified to read;

$$L(\theta) = L_0 f(\theta). \quad (4-34)$$

Equating this to the spectral irradiance from the source gives;

$$E = \frac{1}{\rho} \int L(\theta) d\Omega ; \quad (4-35)$$

where the reflectance,  $\rho$ , is again assumed to be independent of  $\theta$ . This equation is written in terms of  $\theta$  and  $\phi$ ;

$$E = \frac{1}{\rho} \int_{\phi=0}^{2\pi} \int_{\theta=0}^{\pi/2} (L_0 f(\theta)) \sin\theta d\theta d\phi). \quad (4-36)$$

Solving for  $\phi$  leaves;

$$E = 2\pi \frac{1}{\rho} \int_0^{\pi/2} L_0 f(\theta) \sin\theta d\theta . \quad (4-37)$$

Equation 4-37 may not be solved analytically without knowing  $f(\theta)$ . It may be solved in general terms by using the definition;

$$\Psi = \int_0^{\pi/2} f(\theta) \sin\theta d\theta ; \quad (4-38)$$



which leads to the solution;

$$E = L_0 \frac{2\pi\Psi}{\rho}. \quad (4-39)$$

Thus, the spectral radiance normal to the screen is;

$$L_0 = \frac{\rho E}{2\pi\Psi}; \quad (4-40)$$

and the directional spectral radiance is;

$$L(\theta) = \frac{\rho E}{2\pi\Psi} f(\theta). \quad (4-41)$$

Substituting this into Equation 4-6 yields:

$$P = \left( \frac{A_t A_s}{\pi f^2} \right) \rho E \left( \frac{f(\theta)}{2\Psi \cos\theta} \right). \quad (4-42)$$

Assuming that the reflectance is only slightly different from that for an ideal Lambertian surface, and changes slowly,  $f(\theta)$  is approximated as  $f(\theta)\cos\theta$ . A plot of the data, presented in Figure 4-7, indicates that  $f(\theta)$  is a linear function of  $\theta$ . Substituting  $(m\theta + b)\cos\theta$  for  $f(\theta)$  in Equation 4-36 yields:

$$E = \frac{2\pi L_0}{\rho} \int_0^{\pi/2} (m\theta + b) \cos\theta \sin\theta \, d\theta. \quad (4-43)$$

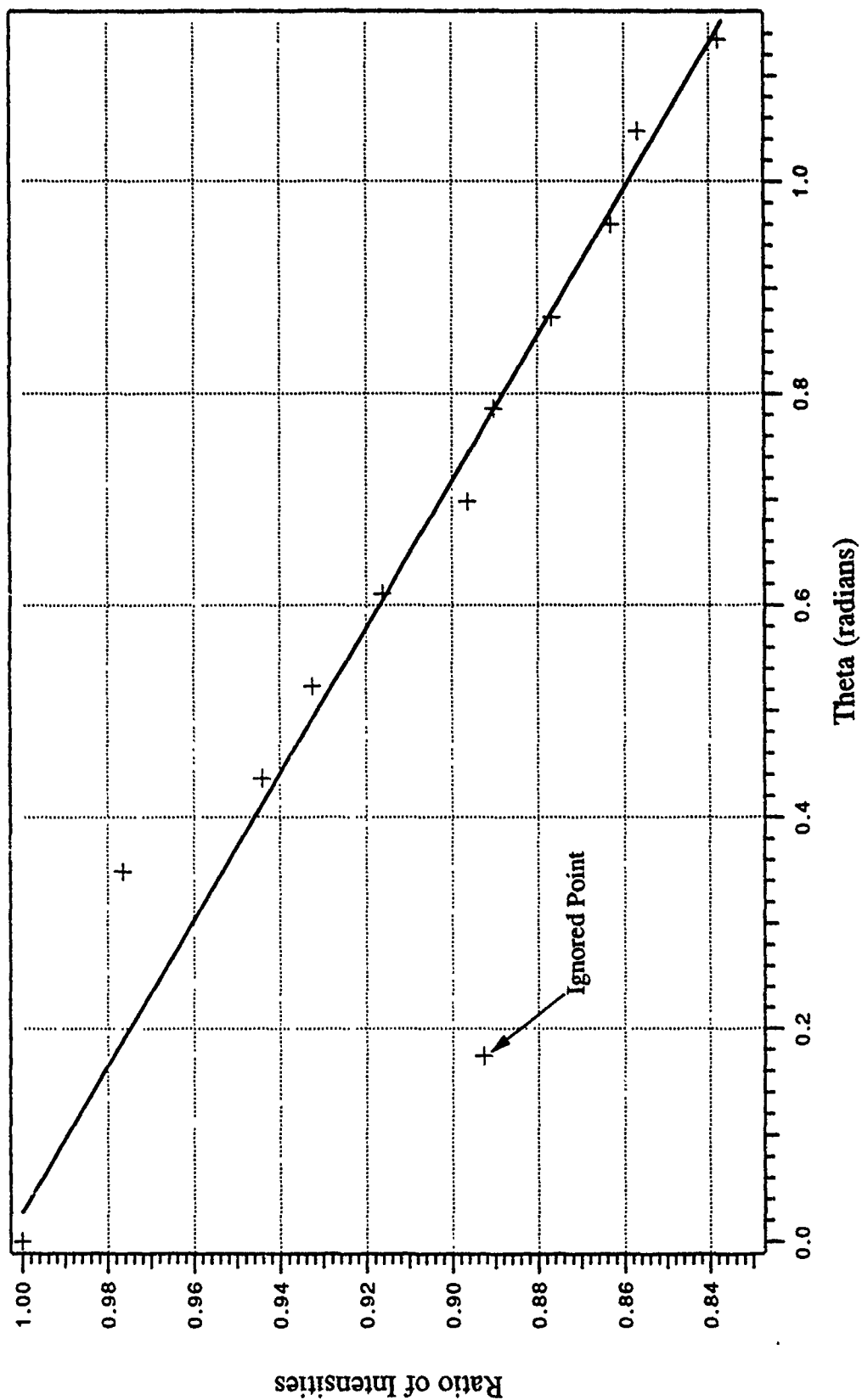


Figure 4-7: Response of MUSTANG instrument to changes in angle  $\theta$  from the screen.

This is solved by parts:

$$E = \frac{2\pi L_0}{\rho} \left( \int_0^{\pi/2} b \cos\theta \sin\theta \, d\theta + \int_0^{\pi/2} m\theta \cos\theta \sin\theta \, d\theta \right); \quad (4-44)$$

$$E = \frac{2\pi L_0}{\rho} \left( \frac{b}{2} + m \int_0^{\pi/2} \theta \frac{\sin 2\theta}{2} \, d\theta \right); \quad (4-45)$$

$$E = \frac{2\pi L_0}{\rho} \left( \frac{b}{2} + \frac{m}{2} \frac{\pi}{4} \right); \quad (4-46)$$

$$E = \frac{\pi L_0}{\rho} \left( m \frac{\pi}{4} + b \right). \quad (4-47)$$

Solving for  $L_0$ :

$$L_0 = \frac{\rho E}{\pi} \frac{1}{\left( m \frac{\pi}{4} + b \right)}. \quad (4-48)$$

Therefore,  $L(\theta)$  may be written as:

$$L(\theta) = \frac{\rho E}{\pi} \frac{(m\theta + b)}{\left( m \frac{\pi}{4} + b \right)} \cos\theta. \quad (4-49)$$

The terms may be gathered to indicate that the directional spectral radiance from the screen is equal to that for an ideal Lambertian screen plus a "correction factor."

$$L(\theta) = \frac{\rho E}{\pi} \cos \theta \left( 1 + \frac{\theta - \frac{\pi}{4}}{\frac{\pi}{4} + \frac{b}{m}} \right). \quad (4-50)$$

This leads to a solution for the total number of photons per second per Angstrom transiting the entrance slit as:

$$P(\theta) = \left( \frac{A_t A_s}{\pi f^2} \right) \rho E \left( 1 + \frac{\theta - \frac{\pi}{4}}{\frac{\pi}{4} + \frac{b}{m}} \right). \quad (4-51)$$

At  $\theta = \pi/4$  this solution is identical to that for an ideal Lambertian surface.

Inasmuch as the calibration data were taken at  $40^\circ$  no correction is deemed necessary due to the angular dependence of the reflectivity of the screen.

#### *g. Linearity of Instrument Response*

The experiment was designed to measure the atmospheric airglow spectra over an altitude range of 100 km to approximately 320 km. Consequently, the data was expected to have a large dynamic range. It was, therefore, necessary to measure the change in response of the MUSTANG instrument to changes in irradiance.

The irradiance was controlled by varying the distance between the Deuterium lamp and the reflective screen. The irradiance at the screen corresponds to the inverse of the square of the distance. The instrument response to the varying irradiance was recorded and the relative intensity at 2500 Å for each distance was plotted versus the square of the ratio of 200 cm to the actual distance between the source and the screen. (These values were selected because the response to the Deuterium lamp peaks at about 2500 Å and this source was normally set at 200 cm from the screen during the other calibration tests.) For simplicity, the square of the ratio of 200 cm to the different distances used in this test will

be called the "distance ratio". A plot of the relative intensity versus the distance ratio is shown in Figure 4-8. The results of this test are also tabulated in Table 4-3.

TABLE 4-3  
MUSTANG INSTRUMENT RESPONSE AT 2500 Å  
TO VARIOUS VALUES OF IRRADIANCE

Data Point	Relative Intensity	Distance (cm) Source to Screen	Distance Ratio
0	994	140	2.04
1	986	150	1.78
2	813	170	1.38
3	722	180	1.23
4	709	180	1.23
5	640	200	1.00
6	581	200	1.00
7	496	220	0.83
8	476	220	0.83
9	410	240	0.69
10	401	240	0.69
11	350	260	0.59
12	298	282	0.50
13	241	311	0.41
14	206	339	0.35

Figure 4-8 indicates a strong linear relationship between the instrument response and the irradiance up to a relative intensity of approximately 800 decimal units per pixel. (This corresponds to an output of 6.2 V from the image sensor.) A check of the instrument response at other wavelengths confirmed this linearity .

Prior to launch the decision was made to reduce the sensitivity of the instrument. To do this the gain voltage supplied to the image intensifier was lowered from 9.77 V to 9.41 V, resulting in a calculated drop of the potential across the MCP to approximately 58% of its original value. The ratio of the instrument response prior to and after this modification was calculated for the Deuterium source and applied uniformly across the wavelength band. This "sensitivity-reduction" coefficient had a measured value of  $0.600 \pm 0.005$ . A post-flight check showed that the MCP gain voltage stayed constant.

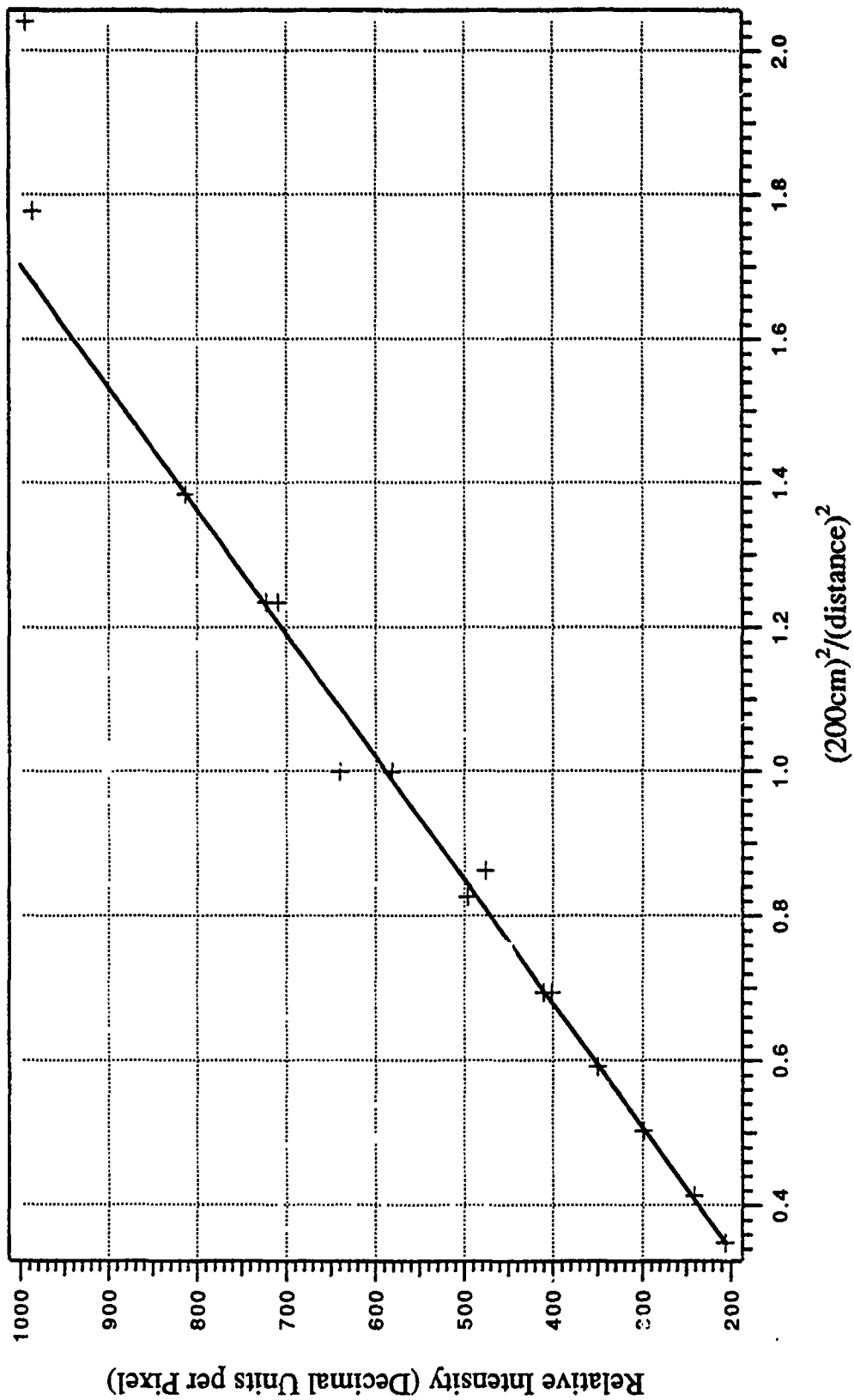


Figure 4-8: Linearity of MUSTANG instrument response to varying irradiance.

#### ***h. Time Dependency of Instrument Response***

The total flight time of the experiment was approximately 14 minutes, with power to the image sensor turned on at +85 seconds followed by power to the high voltage system for the image intensifier at +96 seconds. Data were collected, at a rate of one full spectrum every ~50 ms, from +96 seconds until the high voltage system was turned off at +517 seconds. This sequence was simulated in the laboratory, with measurements of the instrument response to the FEL-IR source taken every minute over a span of 10 minutes. The ratio of each measurement to the initial reading at time "zero" were calculated and are presented in Table 4-4.

**TABLE 4-4  
TIME DEPENDENCE OF MUSTANG INSTRUMENT RESPONSE**

<b>Data Point</b>	<b>Elapsed Time (sec)</b>	<b>Ratio</b>
0	00	1.000
1	60	0.976
2	120	0.959
3	180	0.944
4	240	0.939
5	300	0.929
6	360	0.923
7	420	0.919
8	480	0.916
9	540	0.913
10	600	0.908

The results were fitted with an exponential curve with a lower limit of 0.904 and a decay constant of 224 seconds. This indicates that the instrument response will not stabilize over the 421 seconds that data is collected. The measured response at 420 seconds of elapsed time was 92% that at high voltage turn on. This establishes an uncertainty in the data of  $\pm 8\%$ . The data and curve fit are presented in Figure 4-9.

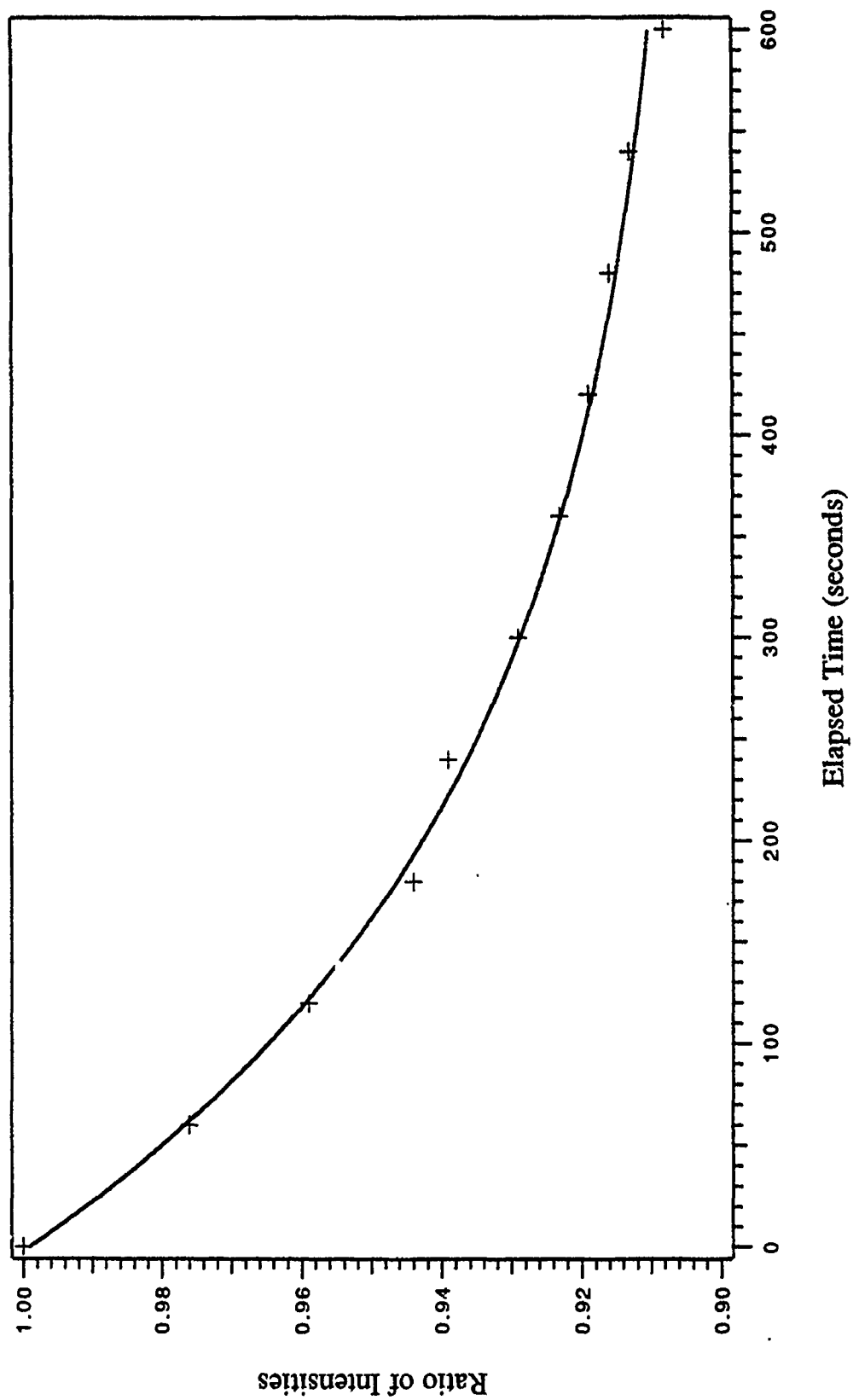


Figure 4-9: Time dependence of MUSTANG instrument response.



During various post-flight tests the instrument response to the Deuterium lamp was 9% lower than the pre-flight measurements while the response to the FEL-IR source ranged from 4 to 18% higher than expected. (The expected response of the instrument to the FEL-IR source in post-flight tests is based on the uniform application of the sensitivity reduction coefficient over the entire data bandwidth.) Although a lamp-log for the Deuterium lamp was not maintained it was determined that the drop in response is probably due to a decrease in source output and not detector sensitivity. The discrepancy in the FEL-IR readings are more difficult to assess.

The tests in question were made after the detector had been on for 10 minutes, by which time the instrument response should have reached its lower limit based on the initial time dependence test. After the instrument was on for about 2 hours the response to the FEL-IR source was almost identical to the reduced pre-flight measurements. Due to the difficulty in reproducing a specific time dependency function from day to day it was decided not to apply a time dependency correction to the data set for the initial analysis.

## 2. Wavelength Calibration

The design of the MUSTANG instrument is optimized for a bandwidth from 1800 Å to 3400 Å. Shorter wavelengths are attenuated by the quartz input window of the image intensifier, while the quantum efficiency of the CsTe photo-cathode drops rapidly for wavelengths above 3200 Å. The precise limits of the wavelength region striking the photo-detector are controlled by varying the angle of the diffraction grating relative to the Ebert mirror. To accurately determine the setting of the grating a wavelength calibration was performed using a FISHER SCIENTIFIC platinum hollow cathode lamp. The platinum lamp provides a wide range of spectral emissions in the wavelength region of interest.

The pixel positions on which 23 selected line emissions fell were determined by a rough approximation of the centroid of the emission profiles. The wavelengths of the 23 emissions were plotted versus the pixel position and a line fit was determined;

$$\lambda = [(1798.0 + 3.134N) \pm 0.5] \text{ \AA}; \quad (4-52)$$

where N is the pixel number. The standard deviation of the slope for this fit is  $\pm 0.002$ . This also determines the numerical value of  $3.134 \pm 0.002$  for  $B_w$ .

A plot of the instrument response to the platinum source is shown in Figure 4-10, with the 23 line emissions used in the wavelength calibration tagged. Figure 4-11 is a plot of the 23 emissions versus their respective pixel positions with the line fit overlayed.

The actual position a given wavelength will strike the detector is a function of the diffraction angle and the focal length of the Ebert mirror  $[(N-256) = f \tan\theta]$ . Therefore, a line fit is only valid in the small angle approximation where  $\tan\theta \sim \theta$ . A second order approximation requires a third order polynomial (with the coefficient for the second order term equal to zero). With the exception of a single data point, however, the best polynomial fit obtained did not significantly improve the match between the actual and calculated wavelengths for the 23 data points.

Table 4-5 lists the 23 identified emissions and their respective pixel positions, and compares these data points to the wavelengths calculated by the line fit and the best polynomial fit obtained.

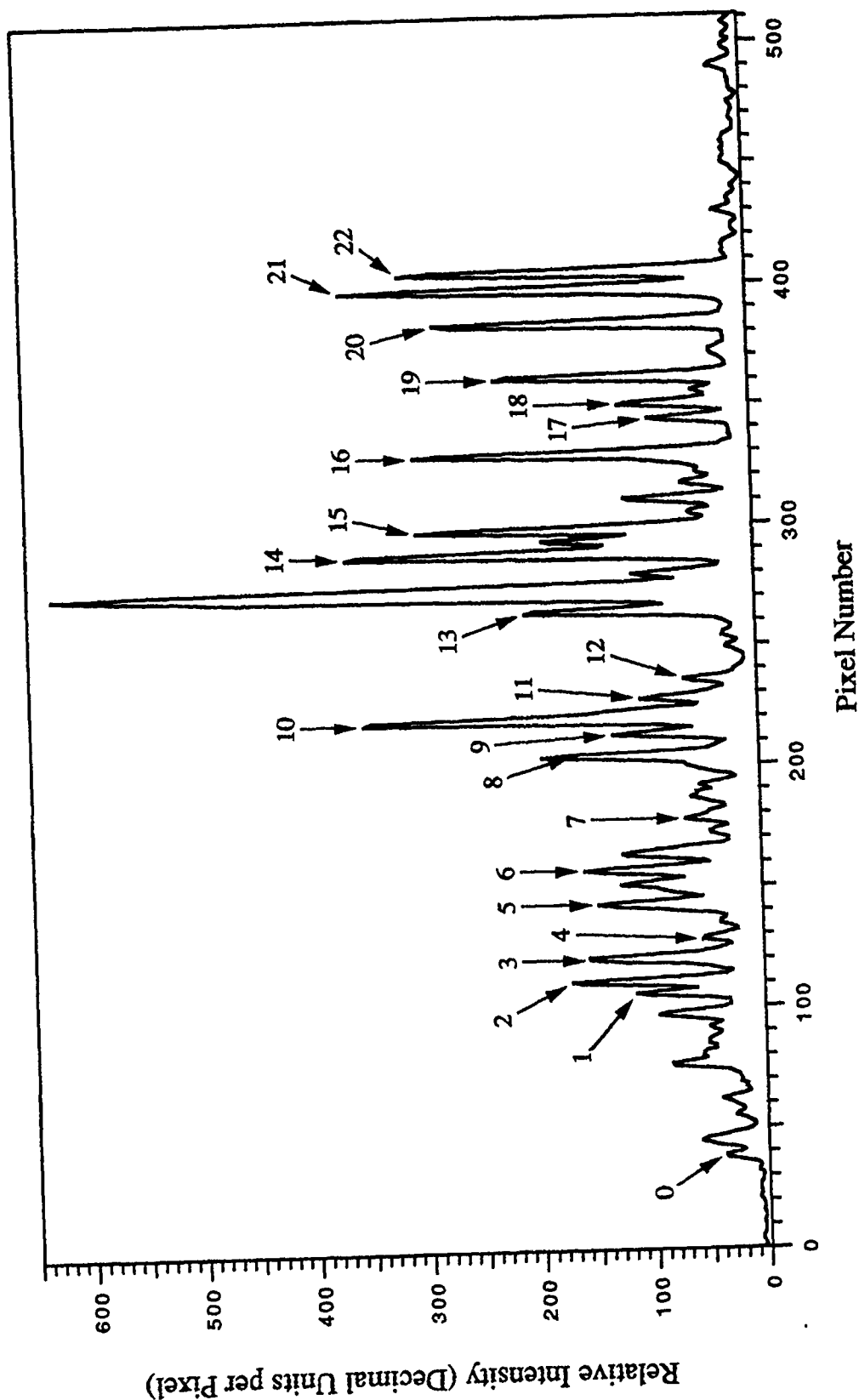


Figure 4-10: MUSTANG instrument recording of spectrum from a Platinum hollow cathode lamp. The 23 emissions used in the wavelength calibration are indicated (see Table 4-5).

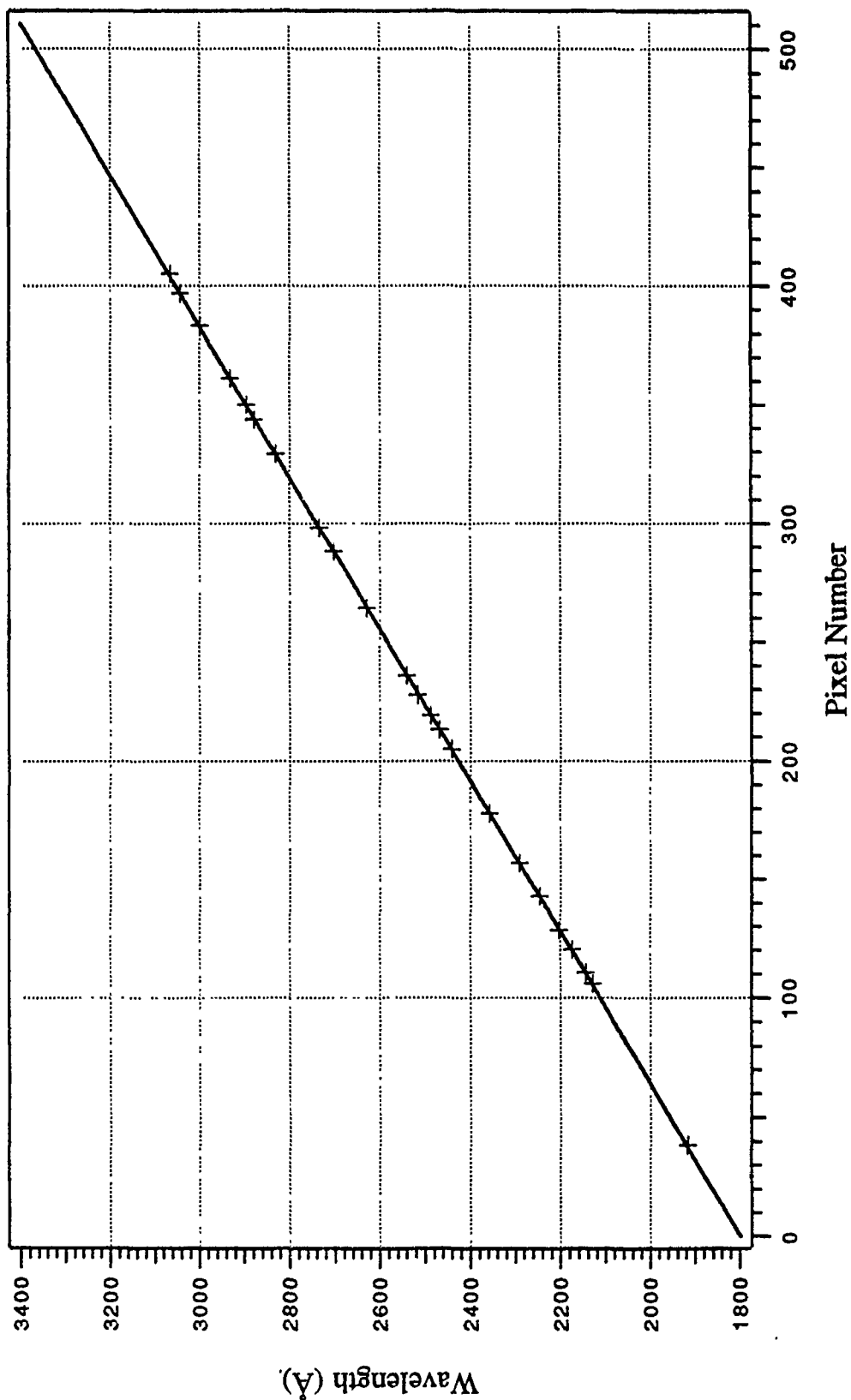


Figure 4-11: Wavelength versus pixel number of 23 selected emissions from platinum hollow cathode lamp. Solid line shows linear least squares fit;  $\lambda = 1798.0 + 3.134N$  (Å).

TABLE 4-5  
SELECTED EMISSIONS OF PLATINUM HOLLOW CATHODE LAMP

Data Point	Pixel Position	Selected Emissions (Å)	Calculated Wavelengths (Å)	
			Line-fit	Polynomial
0	38.6	NeII 1916.08	1918.9	1916.3
1	106.0	PtII 2128.61	2130.2	2130.2
2	110.8	PtI/II 2144.23	2145.2	2145.3
3	120.5	PtI 2174.67	2175.6	2175.9
4	128.5	PtI 2202.22	2200.7	2201.1
5	143.0	PtII 2245.52	2246.1	2246.7
6	157.0	PtI 2289.27	2290.0	2290.6
7	178.0	PtI 2357.10	2355.8	2356.5
8	205.0	PtI 2440.06	2440.4	2441.0
9	213.2	PtI 2467.44	2466.1	2466.6
10	219.4	PtI 2487.17	2485.5	2486.0
11	228.0	PtI 2515.58	2512.5	2512.9
12	236.0	PtI 2539.20	2537.6	2537.9
13	264.4	PtI 2628.03	2626.6	2626.6
14	288.4	PtI 2702.40	2701.8	2701.5
15	298.3	PtI 2733.96	2732.8	2732.5
16	329.4	PtI 2830.30	2830.2	2829.8
17	344.0	PtI 2877.52	2876.0	2875.5
18	350.2	PtI 2893.86	2895.4	2895.0
19	361.4	PtI 2929.79	2930.5	2930.1
20	383.7	PtI 2997.97	3000.4	3000.2
21	397.0	PtI 3042.64	3042.1	3042.1
22	405.3	PtI 3064.71	3068.1	3068.3

For simplicity, the line fit was used in calibration and data analysis. An evaluation of the platinum spectrum after the flight indicated that there was no change in the wavelength calibration.

### 3. Field of View (FOV) Calibration

From the geometry of the MUSTANG instrument the field of view was calculated to be approximately  $2.3^\circ$  by  $0.06^\circ$ . Following the flight this parameter was examined by direct measurement. The instrument was placed on a rotation stage which has an angular resolution of 5 minutes of arc. The stage was set-up in a long corridor. A mercury (Hg) pen-ray source was placed at a distance of approximately 150 feet from the opening of the

instrument's telescope and aligned with the optical axis of the instrument. A system of baffles was erected to prevent off-axis scattering. The detector response to the Hg 2357Å emission was recorded as the instrument was rotated through the field of view.

During flight the instrument was oriented so that the long dimension of the slit was in the vertical direction. Thus, the vertical FOV was expected to be 2.3°. A plot of the instrument response to the vertical FOV, found in Figure 4-12, shows a full width at half maximum (FWHM) of 2.0°.

The horizontal FOV was checked and found to be less than with the angular resolution of the rotation stage (0.08°). This is consistent with the estimated FOV of 0.06°. Based on the vertical FOV of 2.0° a bin size of 10 km was selected for the data.

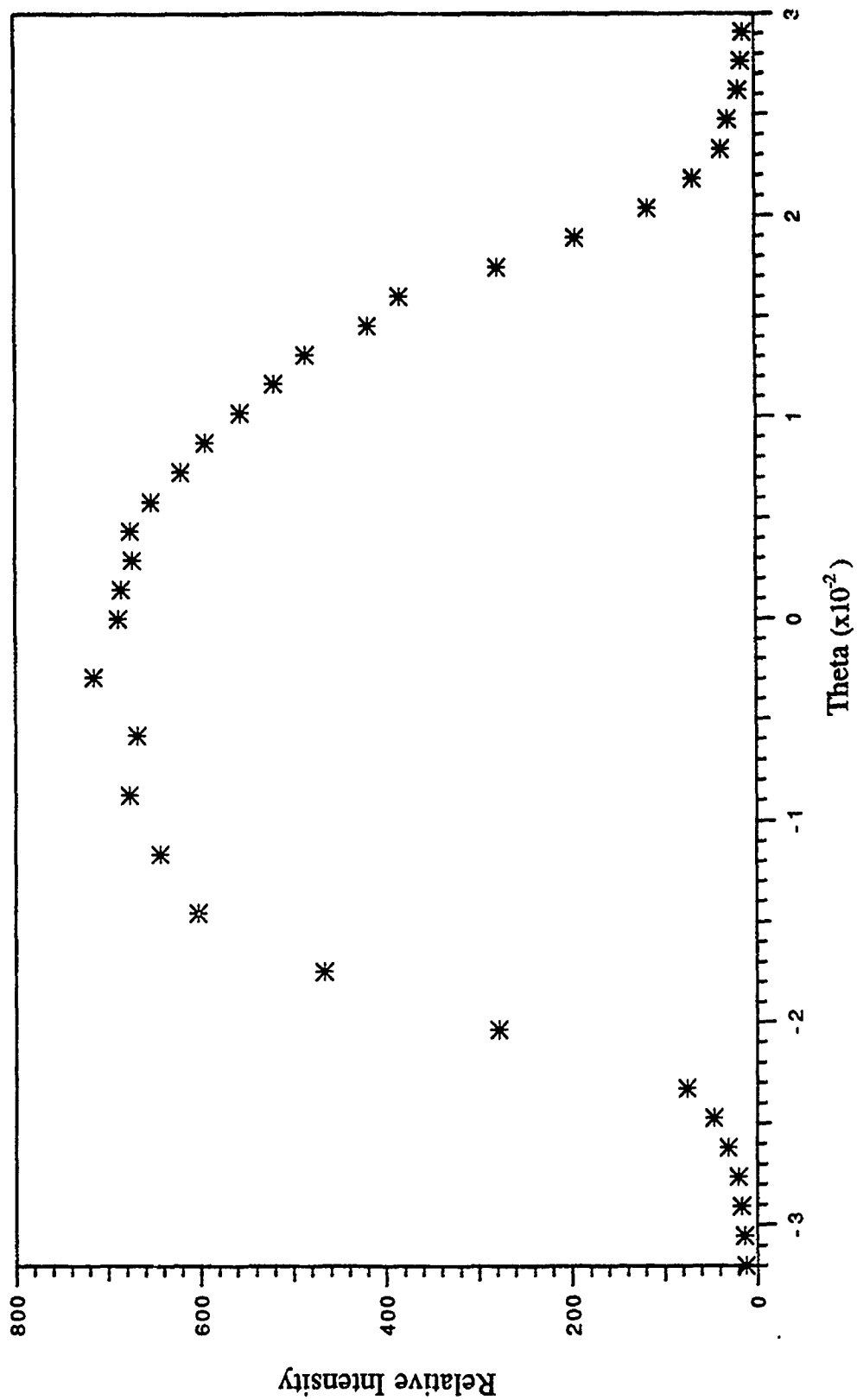


Figure 4-12: Vertical FOV for MUSTANG instrument; measured with Hg 2437 Å line emission

## V. DATA ANALYSIS

### A. INTRODUCTION

The data were collected from 100 km to approximately 320 km in altitude during the rocket experiment. The spectra are binned in 10 km intervals, starting at 140 km and continuing to 320 km on the up leg, and covering 180 km down to 100 km on the down leg. The bins are labeled according to the median altitude (eg., the 155 km bin corresponds to spectra collected from 150 km to 160 km). The number of spectra averaged together ranged from 81 in the 105 km bin to 330 in the 315 km bin. The spectrum from the 155 km bin (down leg) is shown in Figure 5-1. It is dominated by emissions of molecular NO from 1800 Å to 2500 Å and of molecular N<sub>2</sub> from 2500 Å to 3400 Å. In addition, relatively strong atomic emissions of O and O<sup>+</sup> are found at 2972 Å and 2470 Å, respectively. The objective of the analysis was to obtain absolute intensity profiles for the OII 2470.4 Å multiplet and the OI 2972.3 Å line emission. In addition, the NO column densities were compared to the values obtained by Clayton (1990) in his analysis of the 2000 Å to 2500 Å wavelength region of this data set. The data were analyzed by comparison with synthetically generated spectra over two regions; from 2420 Å to 2490 Å and from 2920 Å to 2972 Å. The averaged spectra were separated into the two wavelength regions for independent analysis.

The 2420 Å to 2490 Å region has three major constituents; N<sub>2</sub> Vegard-Kaplan (VK) bands, NO γ bands, and the OII 2470.4 Å multiplet. The 2920 Å to 2972 Å region has only two major components; the VK (0-7) band and the OI 2972.3 Å line emission. In addition, the background contribution varies with altitude and wavelength.



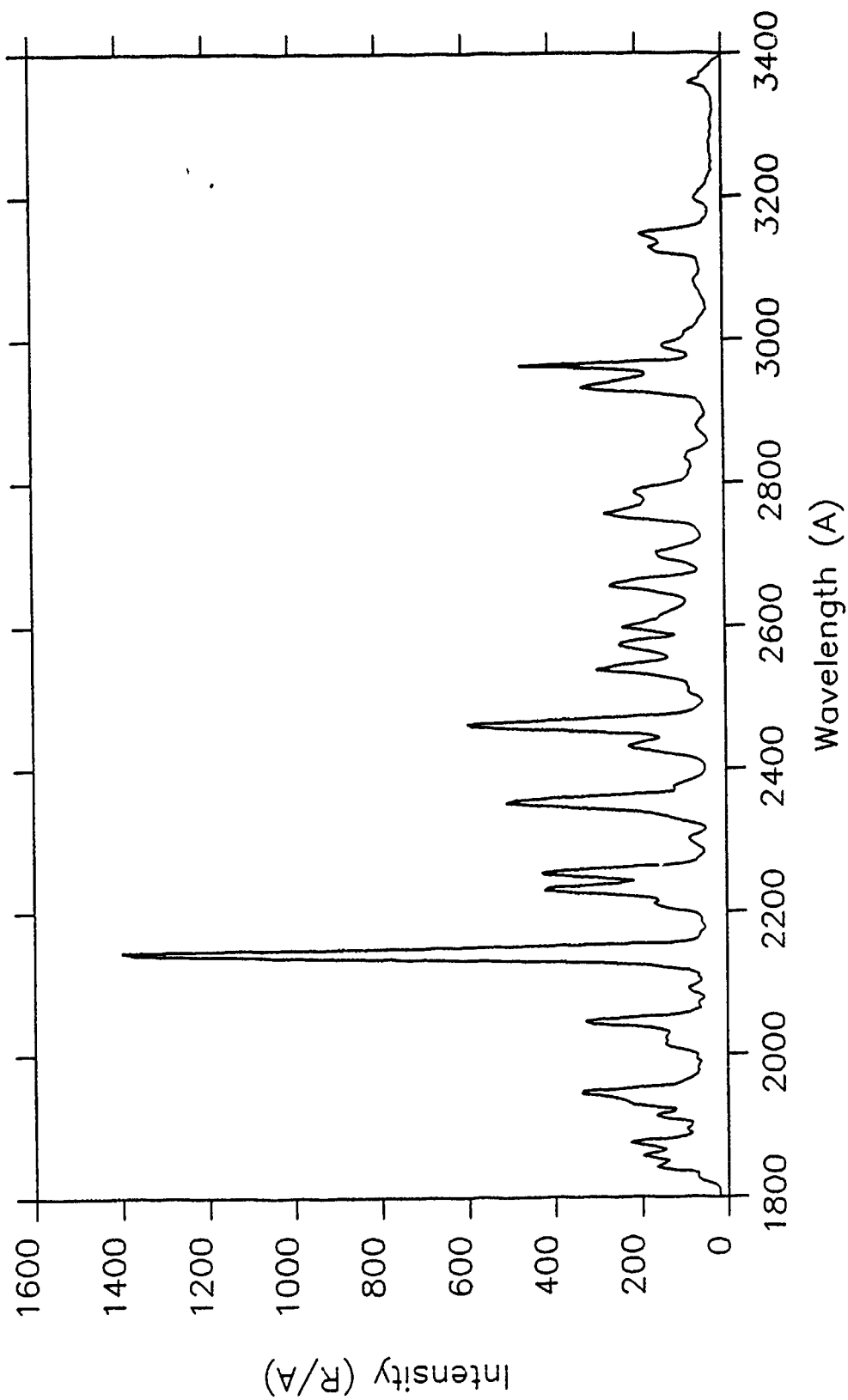


Figure 5-1: Thermospheric dayglow spectrum as measured by the MUSTANG instrument. This spectra, taken at 155 km (down leg), is representative of the data collected.

## B. APPLICATION OF SYNTHETIC SPECTRA

Synthetic spectra for the various N<sub>2</sub> VK bands and the NO  $\gamma$  bands were generated using algorithms developed by Cleary (1986). The temperature profile obtained by Clayton (1990) was used in this process. Before being fitted to the data, the synthetic spectra must be modified to model the wavelength resolution of the detector. This is accomplished by convolving the synthetic spectra with the instrument slit function, which is a measure of the instrument's response to an infinitely narrow emission line or delta function.

The instrument slit function for the MUSTANG instrument was determined from the emission profile of spectral lines of atomic mercury. Two different slit functions were found; a "symmetric" function when an emission falls near the center of a photodiode and a "squared" slit function when an emission line falls between two photodiodes. The wavelength resolution of the instrument, defined as the FWHM of the slit function, was determined to be 10.6 Å.

The shape of the 2470 Å feature indicates that the OII multiplet fell on or near the center of one of the image detector's photodiodes. Thus, the symmetric instrument slit function was selected for convolution with the synthesized spectra in this wavelength region. A discrepancy with the data (see Paragraph F below) makes it difficult to confirm, but the short wavelength edge of the 2972 Å feature suggests that the OI 2972.3 Å line emission fell at or near the boundary between two photodiodes. The squared slit function was used in the fitting procedure over this region.

The OII 2470.4 Å multiplet and OI 2972.3 Å line emissions were modeled by convolving delta functions with the appropriate slit function. The OII multiplet has lines at 2470.4 Å and 2470.3 Å with a relative strength ratio of 5:1 (Wiese, et. al. 1966). The line separation is too fine to be noticed with a wavelength resolution of 10.6 Å, thus a single delta function modeling the stronger of the two lines is used.

The NO  $\gamma$  bands are produced predominately by photo-excitation of the molecule. The rate at which the excitation occurs, and consequently the emission rate, for a given molecular density are known. Therefore, the synthetic spectra generated have specific dimensions of photons per second per molecule per wavelength bin. The N<sub>2</sub> VK bands and the two atomic emissions of interest are forbidden transitions, which are produced exclusively by collisional excitation of the ground states. The production rates for these transitions will depend strongly on solar activity. Only the relative intensities between differing vibrational and rotational transitions are known. Therefore, the synthetic spectra for the N<sub>2</sub> VK bands and atomic transitions are normalized so that the area under their respective curves has a value of one.

Fitting the data with synthesized spectra generates scaling factors; which are converted to column densities for NO and to intensity profiles for the N<sub>2</sub> VK bands, OII 2470.4 Å multiplet and OI 2972.3 Å emission. The NO  $\gamma$  band column densities are obtained by multiplying the scale factors by  $B_w \times 10^6$  ( $B_w = 3.134$  Å/pixel). The intensity profiles for the remaining features are generated by multiplying the scale factors by  $B_w$ .

### C. THE OI 2972 Å LINE EMISSION

The 2920 Å to 2972 Å region was examined first. Fits were performed using a parameter-space grid search adapted by Clayton (1990) from Bevington (1969). The data and associated fits are presented in the appendix. A representative fit to the data in the 195 km bin is presented in Figure 5-2, showing the overall fit and the relative contribution of each constituent. The background component has been subtracted out for clarity. The background component was assumed to be independent of wavelength and was an independent parameter of the grid search.

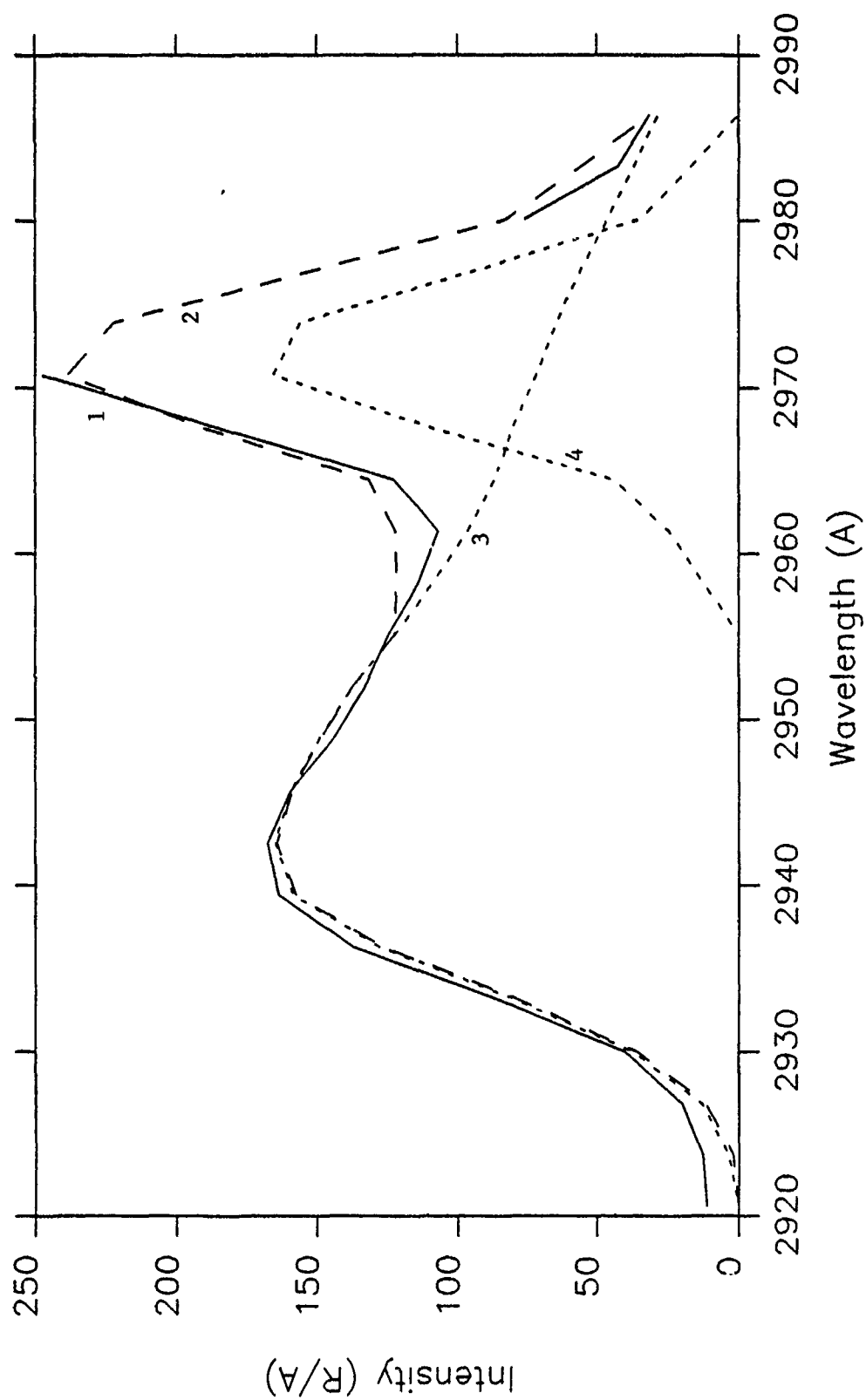


Figure 5-2: Representative fit of the synthetic spectra to the 2972 Å feature. The curves presented are; (1) Data, (2) Overall fit, (3) N<sub>2</sub> VK (0-7) band, and (4) OI 2972 Å line emission.

The scale factors for the OI 2972.3 Å emission and the N<sub>2</sub> VK (0-7) band are converted to intensity profiles. They are presented in Figures 5-3 and 5-4, respectively. The values obtained for the 155 km and 165 km bins (up leg) of the N<sub>2</sub> VK (0-7) band are clearly not in agreement with the rest of the fit. The scale factors obtained for the 155 km and 165 km bins (up leg) of the O 2972.3 Å emission, however, are in close agreement with the corresponding altitude bins on the down leg. The reason for this discrepancy is undetermined at this time.

The fits displayed an increasing divergence from the data over the down leg, especially below 145 km. The temperature profile was modified and an improvement in fit was obtained to the data at and below 145 km. The original temperature profile was determined by comparison of the NO  $\gamma$  (1,0) feature to a synthesis of this feature at various temperatures (Clayton, 1990). Below 145 km this band saturated the detector and the profile was extrapolated to predictions from the mass spectrometer incoherent scatter (MSIS-83) model atmosphere (Hedin, 1983).

Above 145 km the temperature inferred from the observations diverges rapidly from the MSIS predictions. The actual temperature was probably greater than the MSIS predictions because the geomagnetic activity occurring prior to launch was significantly high. The  $\Sigma Kp$  value, an indicator of geomagnetic activity over a 24 hour period, was 40 for the day of launch, with severe geomagnetic activity recorded from 0601 GMT to 1200 GMT, and intense activity recorded from 1201 GMT to 1800 GMT (Bullett, 1990).

The modified profile has a temperature of 400 K at both 105 km and 115 km, which is significantly higher than predicted. The original and modified temperature profiles, along with the MSIS prediction, are presented in Figure 5-5.

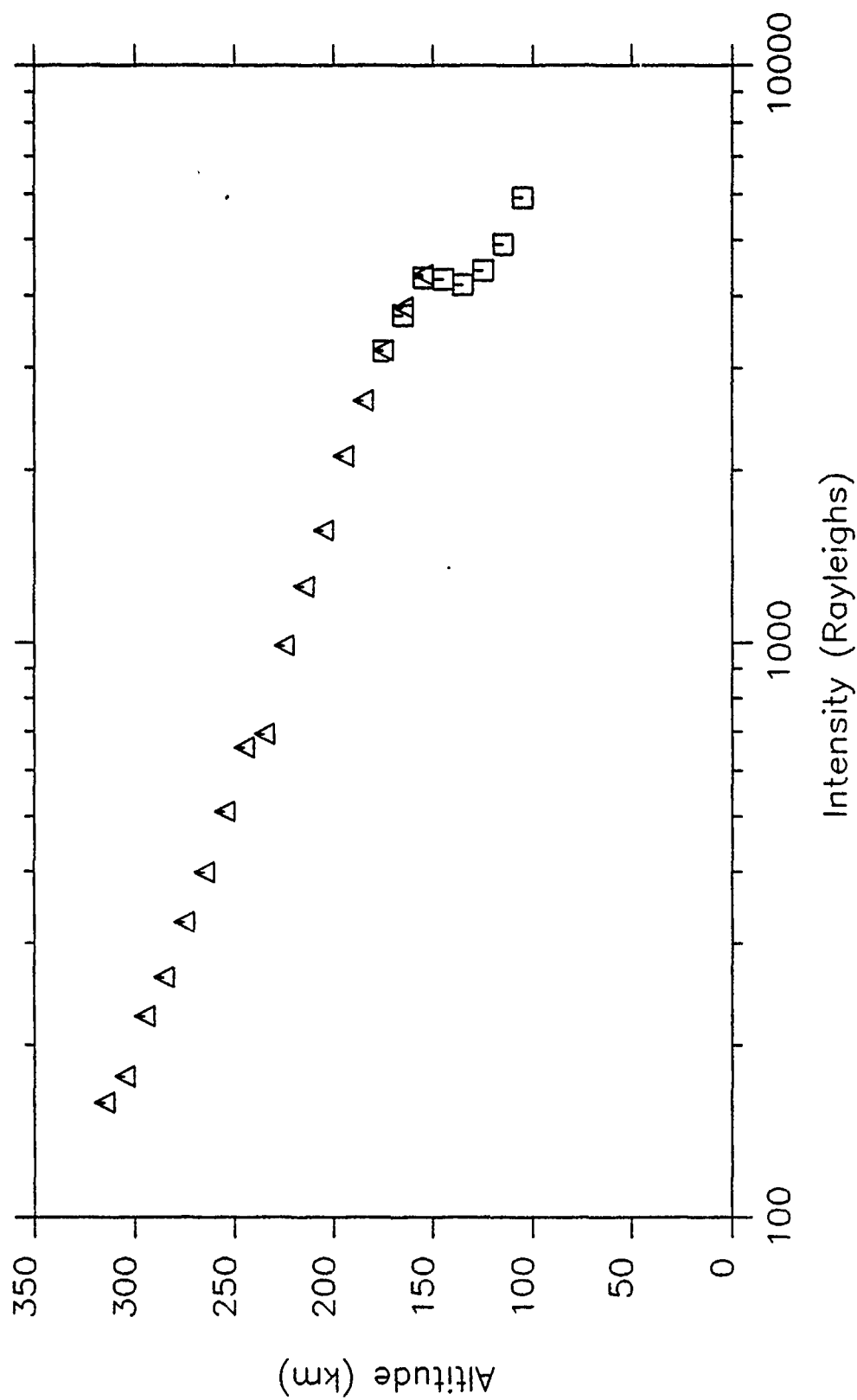


Figure 5-3: Intensity profile of OI 2972 Å line emission. Data from the up leg is represented by triangles, while the down leg is represented by squares. There is a systematic uncertainty of 20% for these intensities at all altitudes.

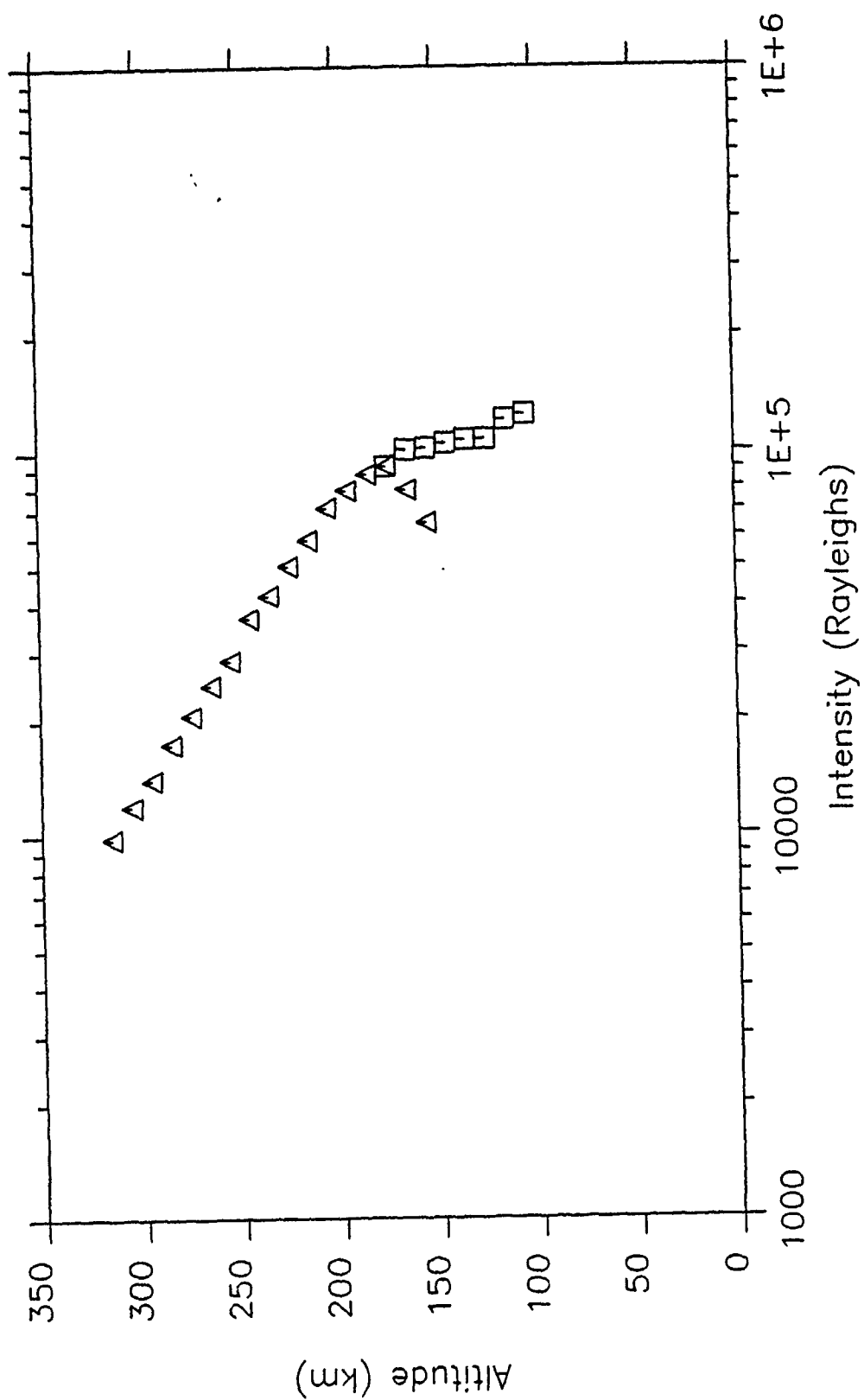


Figure 5-4: Intensity profile of N<sub>2</sub> VK (0-7) band. Data from the up leg is represented by triangles, while the down leg is represented by squares. There is a systematic uncertainty of 20% for these intensities at all altitudes.

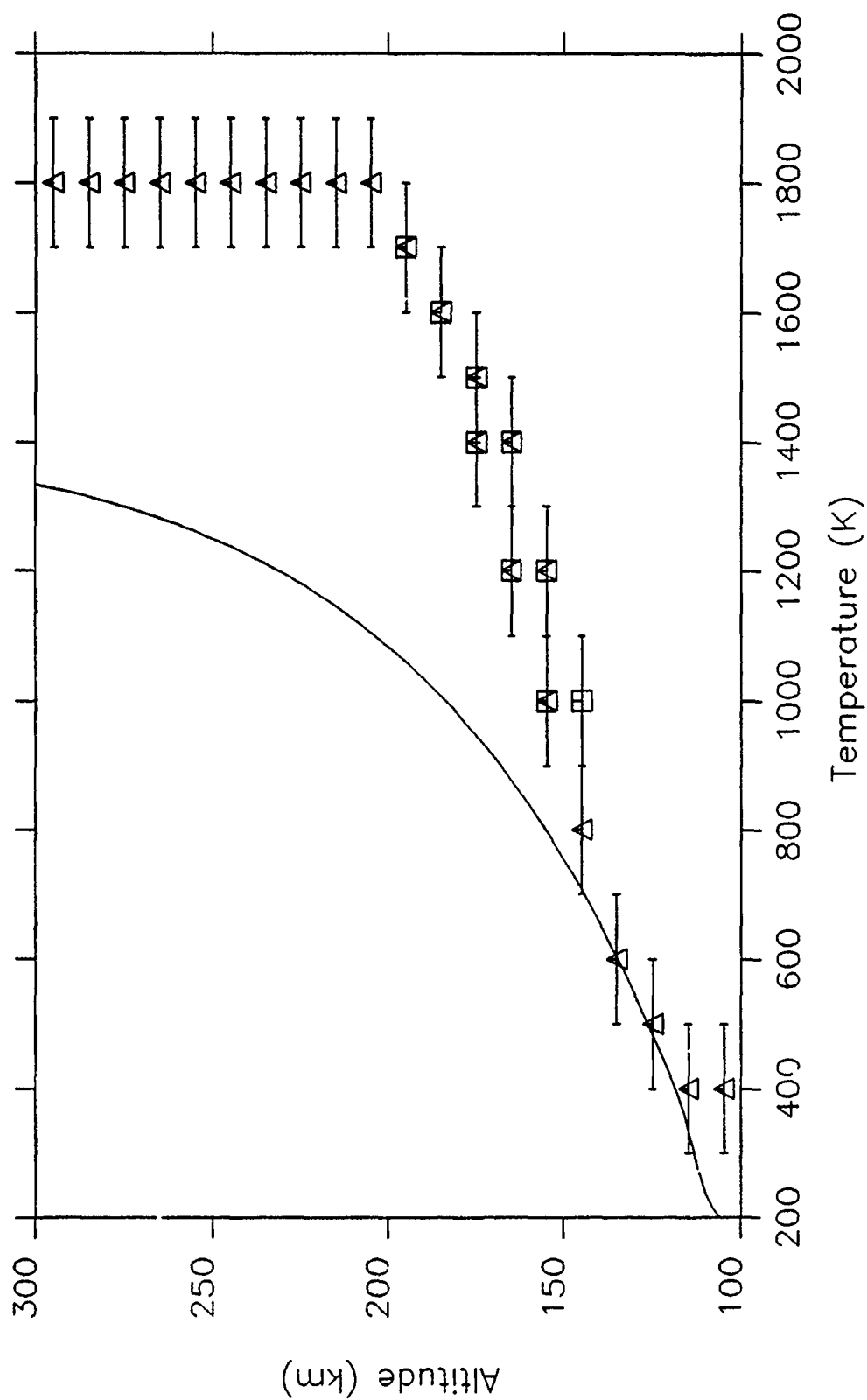


Figure 5-5: Comparison of atmospheric temperature profiles predicted by MSIS-83 (solid curve) and inferred from the data. Temperatures inferred by Clayton (1990) are represented by squares. Temperatures inferred in this analysis are represented by triangles.



The contributions by the background component were found to follow an exponential curve with respect to altitude:

$$B(h) = 6.62 + 9440e^{-\left(\frac{h}{28.33}\right)}; \quad (5-1)$$

where  $B(h)$  is the background in  $R/\text{\AA}$  as a function of altitude,  $h$ , in km. This appears reasonable, as the expected minimum value of the background due to instrument dark count is approximately  $10 R/\text{\AA}$ . Additional contributions are primarily due to Rayleigh scattering which, for a given frequency and flux, is proportional to the atmospheric density.

The calculated values for the background contribution were used to generate background data curves in  $R/\text{\AA}$  over the entire  $1800 \text{\AA}$  to  $3400 \text{\AA}$  wavelength region for each altitude bin. The final fitting routine was performed using the calculated values for the background contribution.

#### D. THE OII 2470 $\text{\AA}$ MULTIPLET

A grid search of the parameter space for the  $2420 \text{\AA}$  to  $2490 \text{\AA}$  region was performed using the two temperature profiles described above. The process was not as sensitive to changes in temperature as it was in the prior analysis, but there is a general reduction in  $\chi$  squared when using the modified temperature profile. The data and associated fits are found in the appendix. Intensity profiles for the two atomic emissions and the column density profile for NO are generated using the fits obtained with the modified temperature profile. A representative fit to the data at  $165 \text{ km}$  is presented in Figure 5-6. For clarity the background contribution has been subtracted out.

The intensity profile for the OII  $2470.4 \text{\AA}$  multiplet is presented in Figure 5-7. It shows a broad profile with a maximum intensity at approximately  $250 \text{ km}$ .

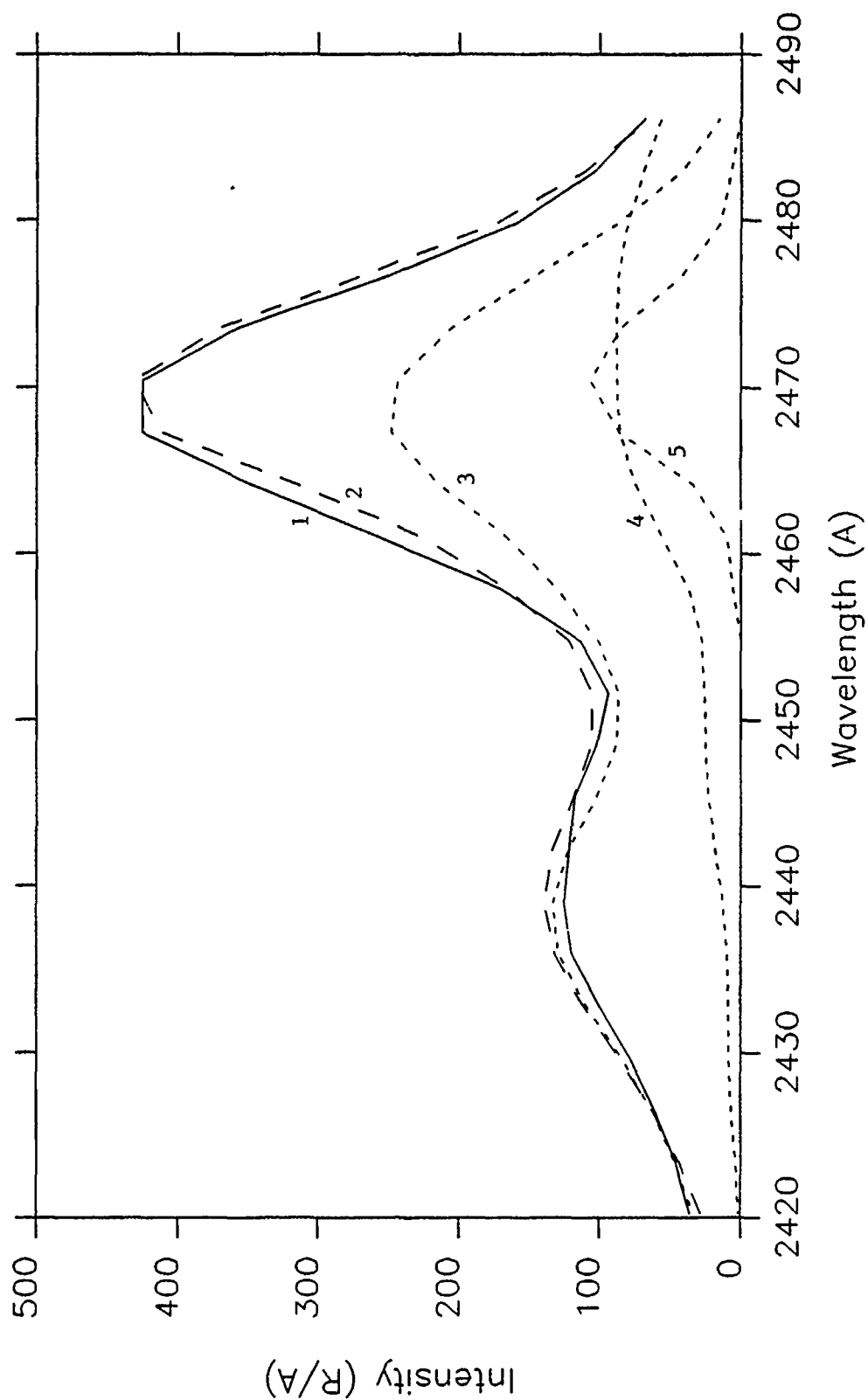
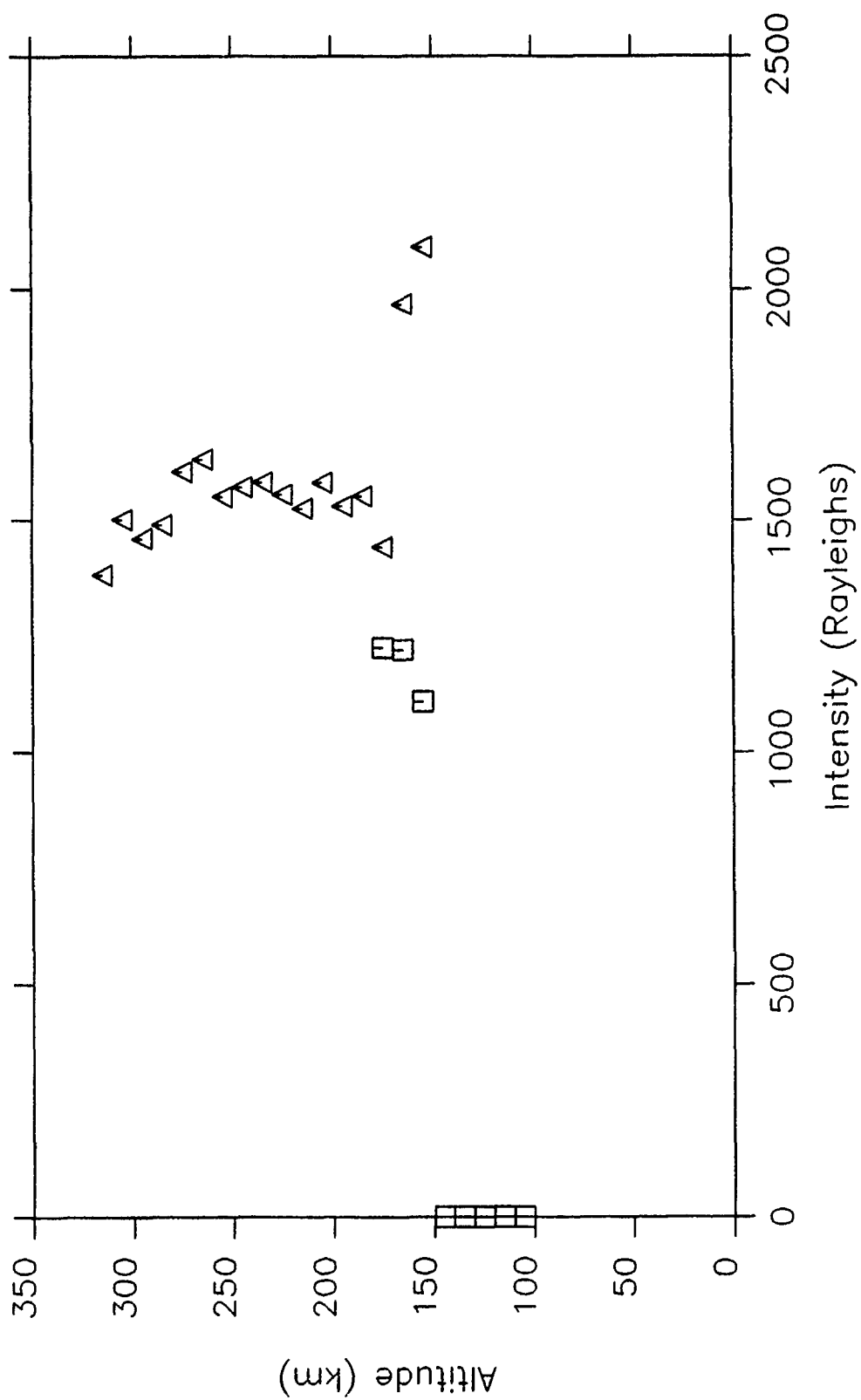


Figure 5-6: Representative fit of the synthetic spectra to the 2470 Å feature. The curves presented are; (1) Data, (2) Overall fit, (3) N<sub>2</sub> VK bands, (4) NO γ bands, and (5) OII 2470 Å multiplet.



An intensity profile for the N<sub>2</sub> VK (0-4) band was generated by multiplying the scale factors for the VK bands by the ratio of the area under the (0-4) band to the area under all the VK bands in this wavelength region. The ratio of these areas is approximately 47%. The intensity profile of the N<sub>2</sub> VK (0-4) band is shown in Figure 5-8.

A plot of the NO column densities versus altitude is found in Figure 5-9. The values obtained in this analysis are compared with those determined by Clayton (1990) in Figure 5-10, and are presented in Table 5-1.

TABLE 5-1  
COMPARISON OF COLUMN DENSITIES FOR NO

Altitude Bin (km)	Leg	Column Density (molecules/cm <sup>2</sup> )	
		Andersen	Clayton
155	up	2.8x10 <sup>15</sup>	2.5x10 <sup>15</sup>
165	"	2.3	2.0
175	"	2.3	1.9
185	"	1.7	1.5
195	"	1.4	1.2
205	"	1.2	---
215	"	9.6x10 <sup>14</sup>	---
225	"	7.6	---
235	"	6.4	---
245	"	5.3	---
255	"	4.1	---
265	"	3.5	---
275	"	2.9	---
285	"	2.5	---
295	"	2.1	---
305	"	1.9	---
315	"	1.7	---
175	down	2.4x10 <sup>15</sup>	1.9x10 <sup>15</sup>
165	"	3.2	2.7
155	"	4.8	4.1
145	"	7.3	7.8
135	"	8.4	1.1x10 <sup>16</sup>
125	"	1.1x10 <sup>16</sup>	1.4
115	"	1.6	2.0
105	"	2.0	2.3

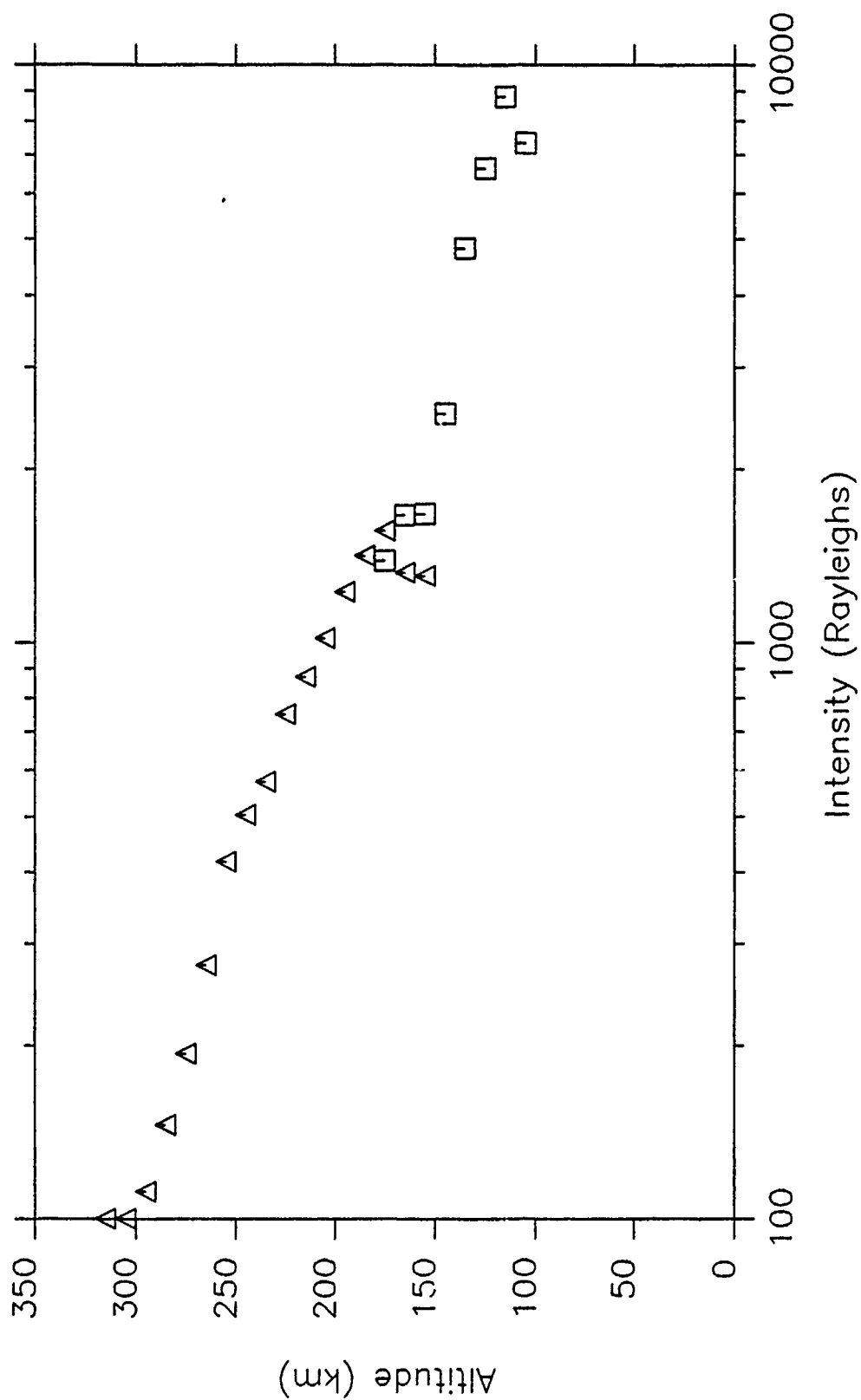


Figure 5-8: Intensity profile of N<sub>2</sub> VK (0-4) band. Data from the up leg is represented by triangles, while the down leg is represented by squares. There is a systematic uncertainty of 10% for these intensities at all altitudes.

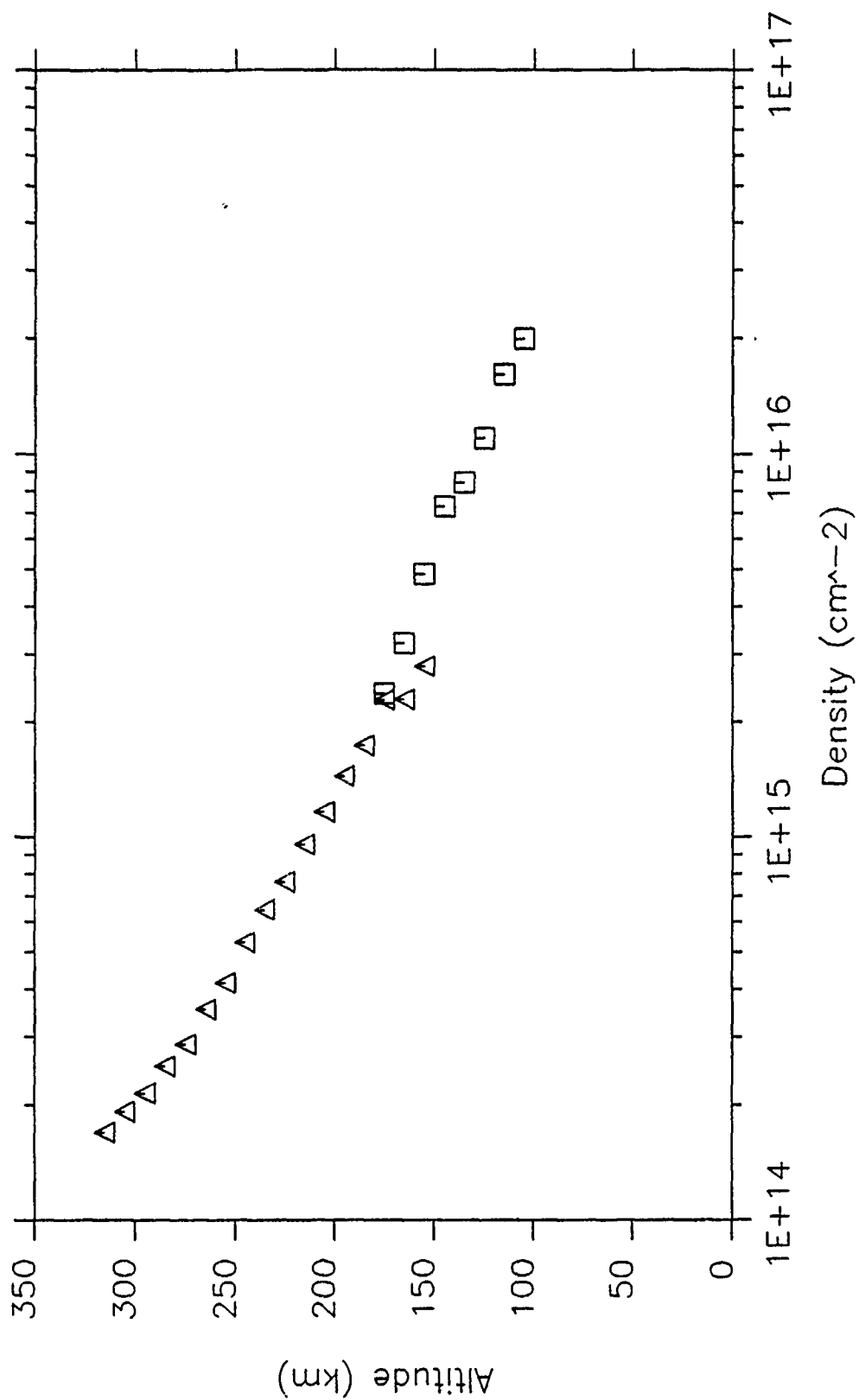


Figure 5-9: Column density profile of NO. Data from the up leg is represented by triangles, while the down leg is represented by squares. There is a systematic uncertainty of 10% for these densities at all altitudes.

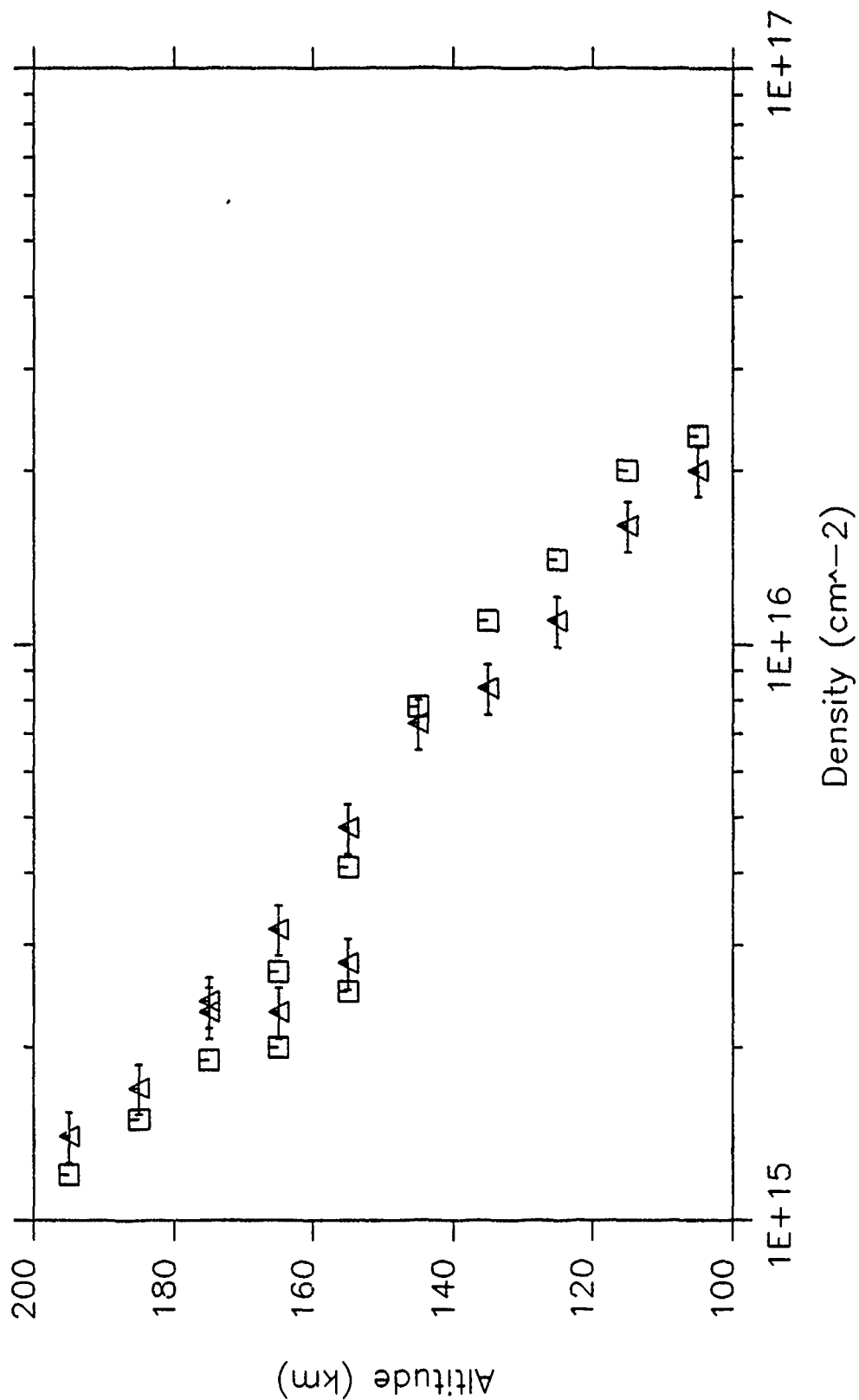


Figure 5-10: Comparison of NO column densities. Values obtained by Clayton (1990) are represented by squares. Densities determined by this analysis are represented by triangles. The error bars indicate the systematic uncertainty in this analysis of 10%.

The NO column densities are in relative agreement, with the differences between the two fits on the order of 20%. The values for the 135 km, 125 km and 115 km altitude bins have differences of 28%, 24% and 22% respectively. An examination of the fits for those altitudes indicates a greater variance from the data compared to the other fits.

The scale factors obtained from the 155 km and 165 km altitude bins (up leg) are not in agreement with the remainder of the fits for all three constituents. In the intensity profile for the OII 2470.4 Å multiplet these values are as much as 90% greater than the corresponding values obtained on the down leg, while the fit obtained for the NO γ band has the up leg values approximately 40% lower than the down leg values. Clayton (1990) found similar discrepancies with these data bins in his analysis of the data set.

The background used for this region was identical to that used in the fitting routine for the 2920 Å to 2972 Å region except that the intensity was reduced by 40% at all altitudes. This 40% reduction is not unreasonable considering the difference in solar flux and the Rayleigh scattering cross sections.

## E. DISCUSSION

The MUSTANG instrument electronics interface relied on a number of timing signals provided by the NASA telemetry system. Two of these signals, the word clock and the data request were logically anded to enable the transfer of data from the FIFO to the buffer in preparation for transmission to ground. Due to an approximately 3 μs lag in the drop of the data request clock (which was low for 16 words then switched high for the last 16 words of each subframe) a seventeenth word was transferred to the buffer during each subframe and was subsequently lost when it was overwritten by the following word during the next subframe. This error was corrected during the data reduction by inserting an averaged value for each dropped word.



An additional discrepancy in the data was noted by Clayton (1990) when he was fitting the 2000 Å to 2500 Å region with synthesized spectra for the NO  $\gamma$ ,  $\delta$  and  $\epsilon$  bands. The data appeared to be shifted progressively with increasing wavelength. Several prominent emissions were used as fiducials to generate a correction for this undetermined discrepancy. As noted in Chapter IV, a comparison of the pre-flight and post-flight calibration data suggests that the wavelength calibration did not change as a result of the flight. Therefore, it is probable that this second discrepancy is also a result of problems with the NASA telemetry timing signals.

The 2920 Å to 2972 Å range is affected by these two discrepancies. The 2972 Å feature falls where one of the data words was calculated to have been dropped by telemetry. After correcting for this, it was found that this feature appeared narrower than the instrument slit function. Based on this it was concluded that this feature was affected by an additional data dropout. Without a means to reconstruct the missing data the fitting procedure was cut-off at the last valid data point for this feature, which is at approximately 2971 Å. Because of this there is a systematic uncertainty of 20% for the intensities calculated for this feature. Figure 5-11 compares the data, as received, with the squared instrument slit function. In Figure 5-12 the correction for the known data dropout is made and the results are again compared with the slit function. Finally, in Figure 5-13 a correction for an additional data dropout is made and the results are again compared with the slit function.

In addition to the data dropouts, the spectra for altitudes above 200 km in the 2920 Å to 2972 Å wavelength region exhibit features which appear to be atomic emission lines at approximately 2942 Å and 2952 Å (see appendix). These features can be seen for all spectra above 200 km, and their relative intensities increase with increasing altitude. Because of their persistence, these features are believed to be real, independent emissions.

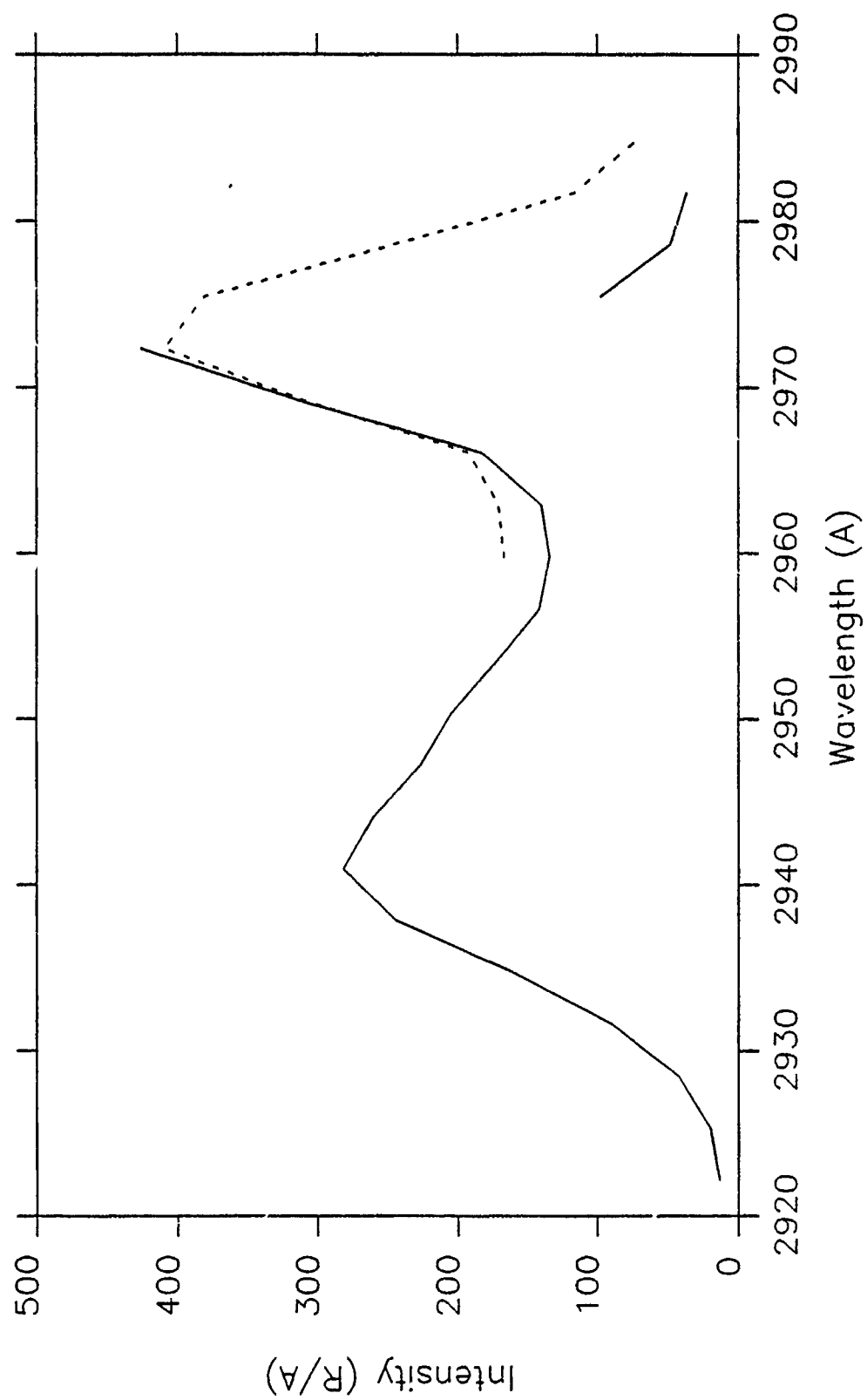


Figure 5-11: Comparison of data as received with instrument slit function at 2972 Å.

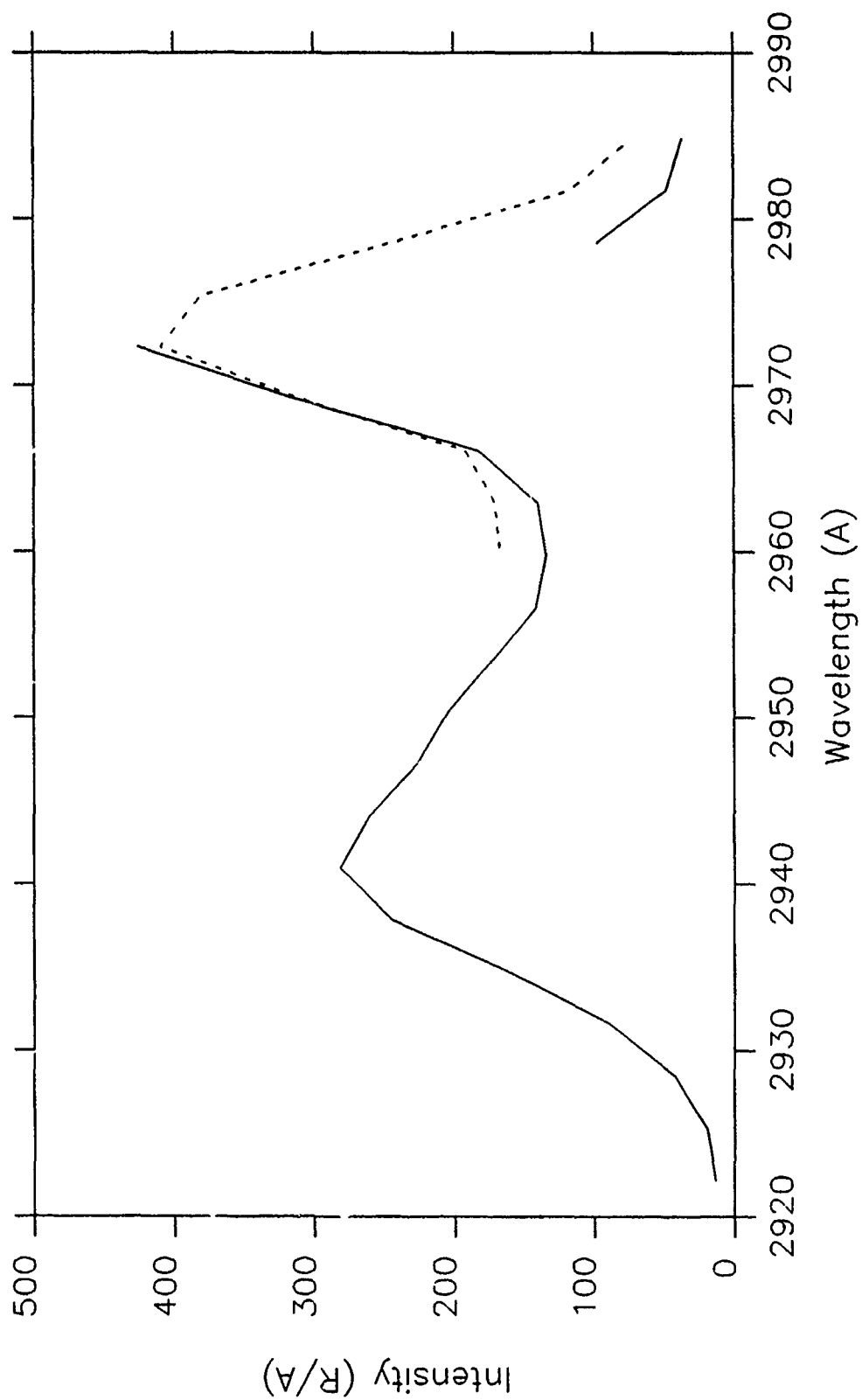


Figure 5-12: Comparison of data corrected for known dropout with instrument slit function at 2972 Å.

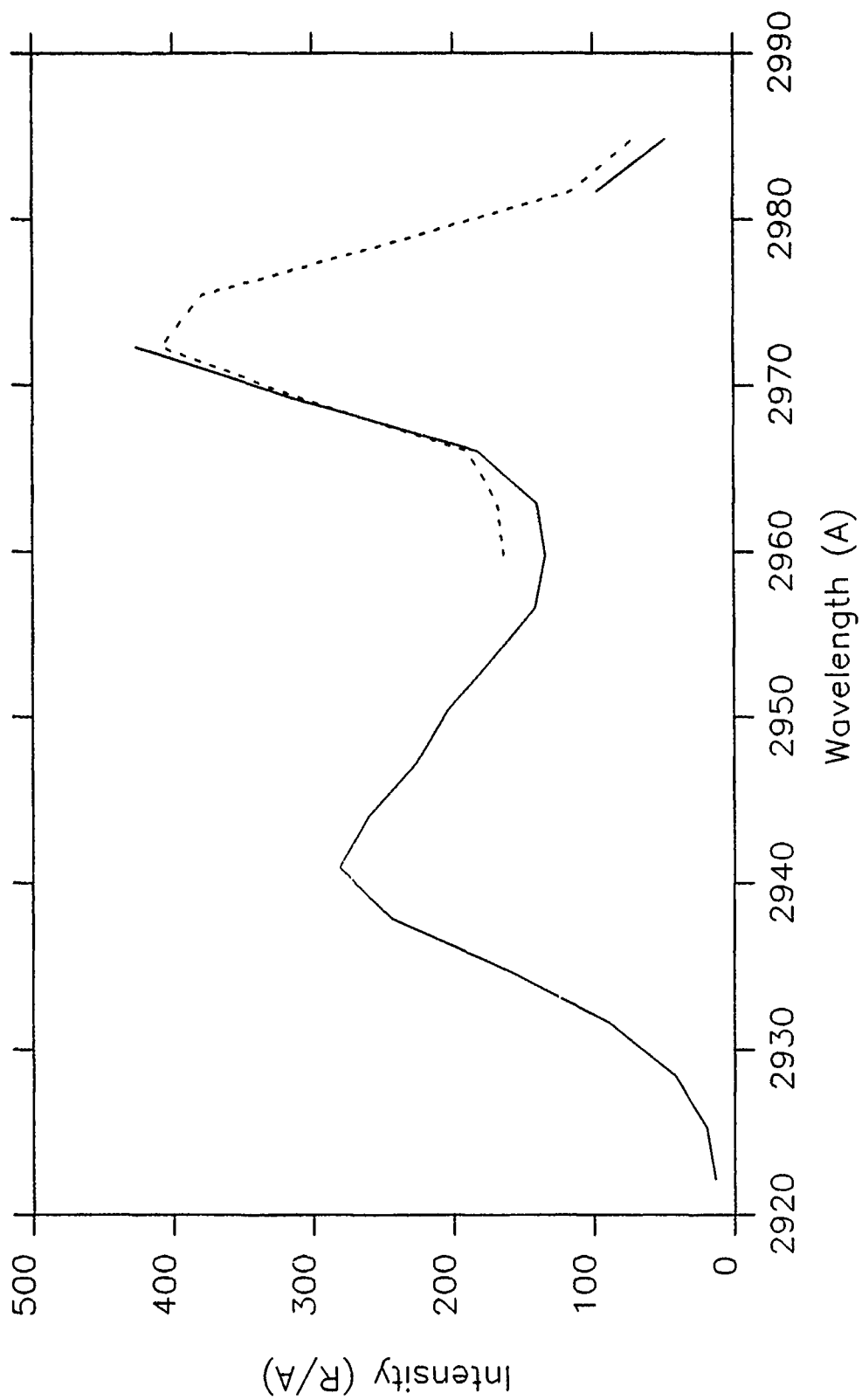


Figure 5-13: Comparison of data corrected for known dropout and anomalous data loss with instrument slit function at 2972 Å.

The synthetic spectra generated for this region did not include emissions at these wavelengths. As a result the fitting program may have overestimated the intensities of the constituent parameters, especially that of the N<sub>2</sub> VK (0-7) band. Emissions at 2942 Å and 2952 Å broaden the data curve relative to the synthetic VK band, especially at lower temperatures. The contamination appears to be altitude dependent and is not readily apparent below 200 km. However, the high temperatures calculated for 115 km and 105 km may be due to contamination of the VK band by the unidentified emissions.

Comparison of the intensity profile of the N<sub>2</sub> VK (0-4) band at 2463 Å with the profile of the N<sub>2</sub> VK (0-7) band at 2937 Å serves as a self-correlation of the fitting programs. In Table 5-2 the intensities for the N<sub>2</sub> VK (0-4) and (0-7) bands are presented, along with the ratio of the two values. The wide variance in the ratio of the intensities for the two bands indicates that the fits are not consistent. Furthermore, the calculated ratio for these two bands using the synthetic spectra algorithm is approximately 0.49. This value was confirmed using a rough calculation of the ratio of the emission rate factors for the two transitions by taking the square of the wavelengths times their respective Franck-Condon factors (Barth, 1965).

The inconsistency between the two fitting routines indicates that one, or both, of the sets of fits are in error. Based on the general agreement between the NO column density profile obtained in the analysis of the 2420 Å to 2490 Å wavelength range with the profile obtained by Clayton (1990) and the apparent contamination of the 2920 Å to 2972 Å range, the fits for the latter range are suspect.

TABLE 5-2  
COMPARISON OF INTENSITIES FOR N<sub>2</sub> VK (0-4) AND (0-7) BANDS

Altitude Bin (km)	Leg	Band Intensity (R)		Ratio (0-4)/(0-7)
(0-4)	(0-7)			
155	up	4.9x10 <sup>3</sup>	5.7x10 <sup>4</sup>	8.6x10 <sup>-2</sup>
165	"	4.9	7.3	5.5
175	"	5.8	8.6	6.7
185	"	5.3	8.2	6.5
195	"	4.5	7.5	6.0
205	"	3.8	6.8	5.6
215	"	3.2	5.6	5.7
225	"	2.8	4.8	5.8
235	"	2.1	4.0	5.3
245	"	1.9	3.5	5.4
255	"	1.5	2.7	5.6
265	"	1.0	2.3	4.3
275	"	7.8x10 <sup>2</sup>	1.9	4.1
285	"	5.4	1.6	3.4
295	"	4.1	1.2	~ 4
305	"	0.0	1.0	0.0
315	"	0.0	8.2x10 <sup>3</sup>	0.0
175	down	5.2x10 <sup>3</sup>	8.6x10 <sup>4</sup>	6.0
165	"	6.2	9.4	6.6
155	"	6.2	9.3	6.7
145	"	9.3	8.7	10.9
135	"	1.8x10 <sup>4</sup>	8.6	20.9
125	"	2.5	9.2	27.2
115	"	3.3	1.1x10 <sup>5</sup>	30.0
105	"	2.7	1.2	22.5

## VI. CONCLUSION

### A. INTRODUCTION

The MUSTANG instrument was calibrated using standard techniques to determine the sensitivity and wavelength calibrations and field of view. The instrument was launched aboard a NASA sounding rocket on March 30, 1990. Post-flight tests indicated that the calibration did not change as a result of the rocket experiment. Ultraviolet dayglow spectra of the Earth's ionosphere were obtained from approximately 100 km to 320 km in altitude over a wavelength range of 1800 Å to 3400 Å. The spectra were divided into 512 pixels of approximately 3.134 Å per pixel. Analyses of the data from 2420 Å to 2490 Å and from 2920 Å to 2972 Å were conducted to obtain the intensity profiles of the OII 2470.4 Å multiplet and the OI 2972.3 Å line emission, respectively.

### B. SUMMARY OF FINDINGS

The intensity profile of the OII 2470.4 Å multiplet was found to have a broad peak of 1.6 kR centered at approximately 250 km. The intensity drops off rapidly below 150 km and is not apparent at altitudes below 140 km.

The intensity profile of the OI 2972.3 Å line emission shows a general trend of decreasing intensity with altitude. The maximum intensity of 3.6 kR was found at 105 km and the minimum of 137 R at 315 km. A partial layer, with an intensity of 4.1 kR, was evident near 150 km. Data dropouts in the wavelength region containing this feature introduce a systematic uncertainty of 20% in the profile.

The average column densities of NO were found to be within 20% of the values obtained by Clayton (1990). This is considered a good correlation due to the limited number of NO emissions in the wavelength regions analyzed. The column densities presented here were derived from a single feature encompassing three NO  $\gamma$  bands. The

synthetic spectra generated to model this feature was only one of three independent variables being fitted to the 2420 Å to 2490 Å wavelength region. The bands included are the (1,3) at 2438.6 Å, the (0,2) at 2470.1 Å and the (3,6) at 2481.2 Å. [Clayton (1990) produced synthetic fits to 11 features, several of which were strictly due to NO emissions. The other features he analyzed were dominated by NO  $\gamma$ ,  $\delta$  and  $\epsilon$  emissions.]

An atmospheric temperature profile for altitudes below 145 km was inferred from the fit of the N<sub>2</sub> VK (0-7) band. Significantly higher temperatures than those predicted by the MSIS-83 model were inferred for altitudes of 105 km and 115 km. The value of 400 K obtained for these altitudes may be artificially high due to possible contamination of the N<sub>2</sub> VK (0-7) band by atomic emissions at 2942 Å and 2952 Å.

### C. RECOMMENDATIONS FOR FURTHER RESEARCH

The time/temperature dependence of the sensitivity calibration needs to be more fully explored. Placing a thermocouple on the driver/amplifier card of the detector system and monitoring the temperature and instrument response as a function of time may provide a clearer understanding of the dynamics of this relationship. The calibration tests should include the use of heat guns and coolants to vary the temperature of the instrument. Incorporation of the time dependence of the instrument response should significantly reduce the uncertainty in the data.

Positive identification of the emission features at about 2942 Å and 2952 Å will allow inclusion of these features in the synthetic spectra fitted to the data. This should produce an improvement to the uncertainty of the fits in the 2920 Å to 2972 Å wavelength region, and provide an indication of whether the high temperatures calculated for 105 km and 115 km are real or are caused by contamination of the N<sub>2</sub> VK (0-7) band.

Prior to launching the MUSTANG instrument on future rocket experiments, the electronics interface should be modified to account for possible lags in the NASA telemetry



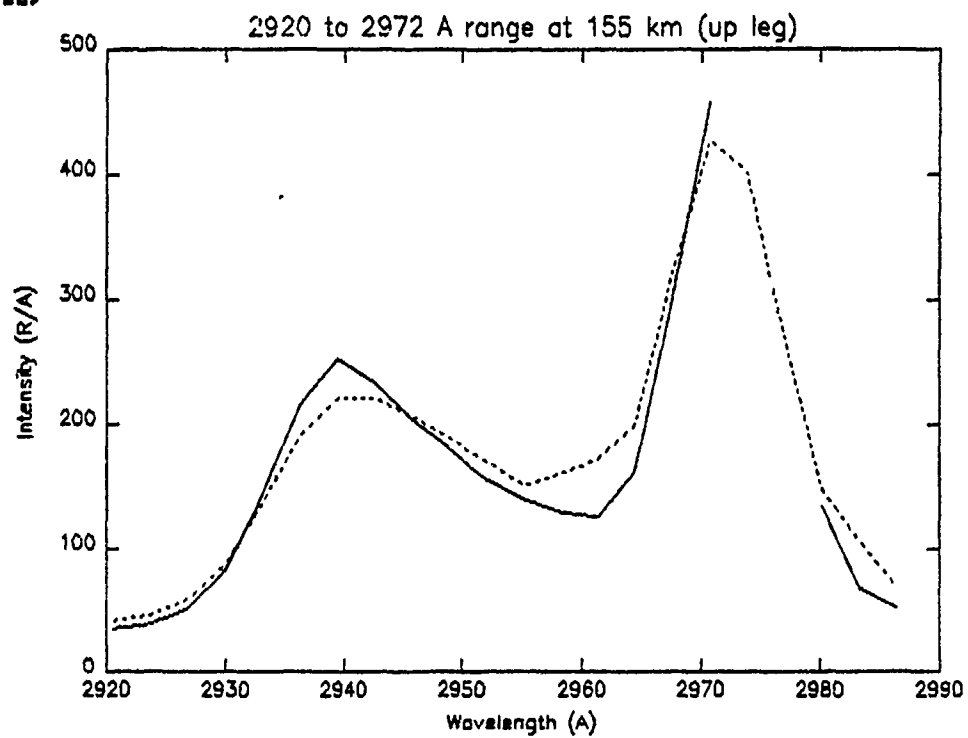
timing signals. A plausible method of doing this is by using a 16-bit shift register to "count out" the data words to be sent to the buffer.

## APPENDIX

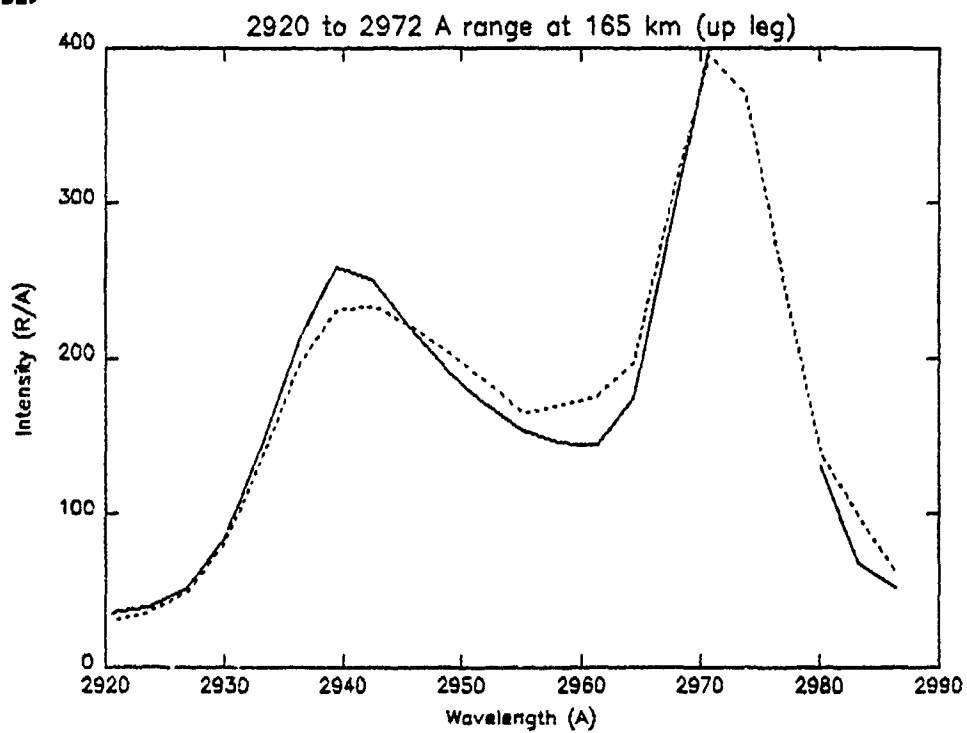
The appendix is broken down into two sections. Pages 82 through 94 show the data curves and best fits obtained with the synthetic spectra for the 2920 Å to 2972 Å wavelength region. The plots are presented sequentially, starting with the 155 km (up leg) altitude bin to the 315 km (up leg) bin and continuing with the 175 km (down leg) bin to the 105 km (down leg) bin. The solid curves display the data and the fits are represented with the dashed curves. The data curve is shown with the correction for both data word dropouts. The fits were produced using the data to the short wavelength side of the break, from approximately 2920 Å to about 2971 Å. The contamination to the N2 VK (0-7) band is noticeable above 200 km, and is quite pronounced above 270 km. Note how the long wavelength side of the modeled OI 2972.3 Å line emission is pushed above the data in the fits above 250 km. This is indicative of the parameter-space grid search program overestimating the intensity of the VK band due to the contamination. There is a similar mismatch between the data and the curve fit for this feature at 115 km and 105 km. This is probably the result of the background component being too large at these altitude bins.

The data and synthetic spectra fits for the 2420 Å to 2490 Å wavelength range are displayed in pages 95 through 107. The format of presentation is the same as for the prior section of the appendix.

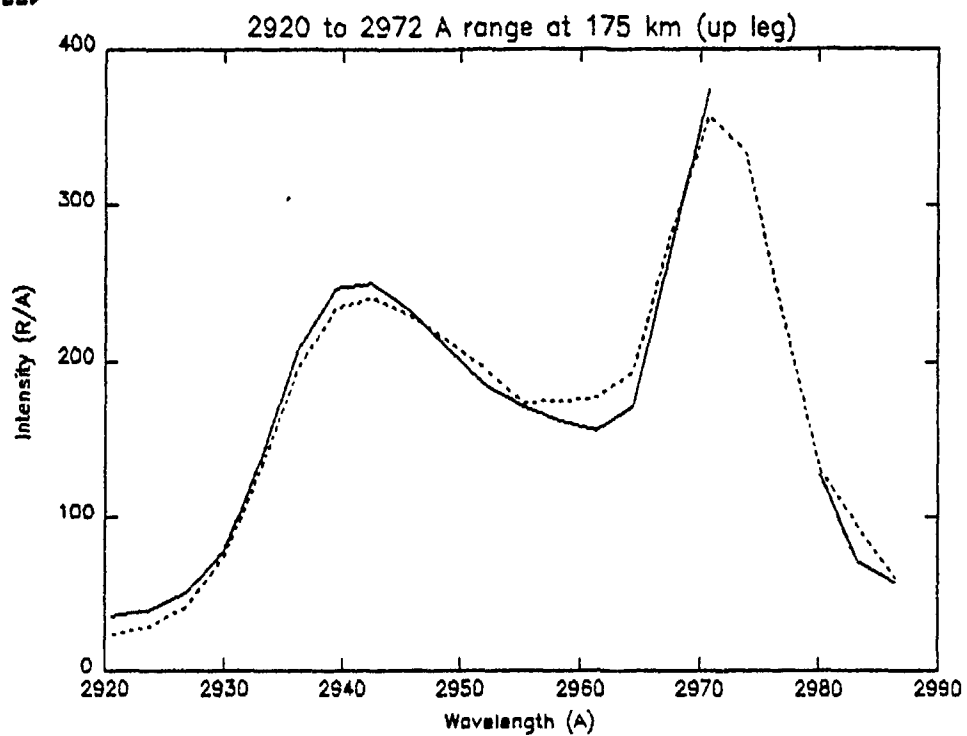
IDL>



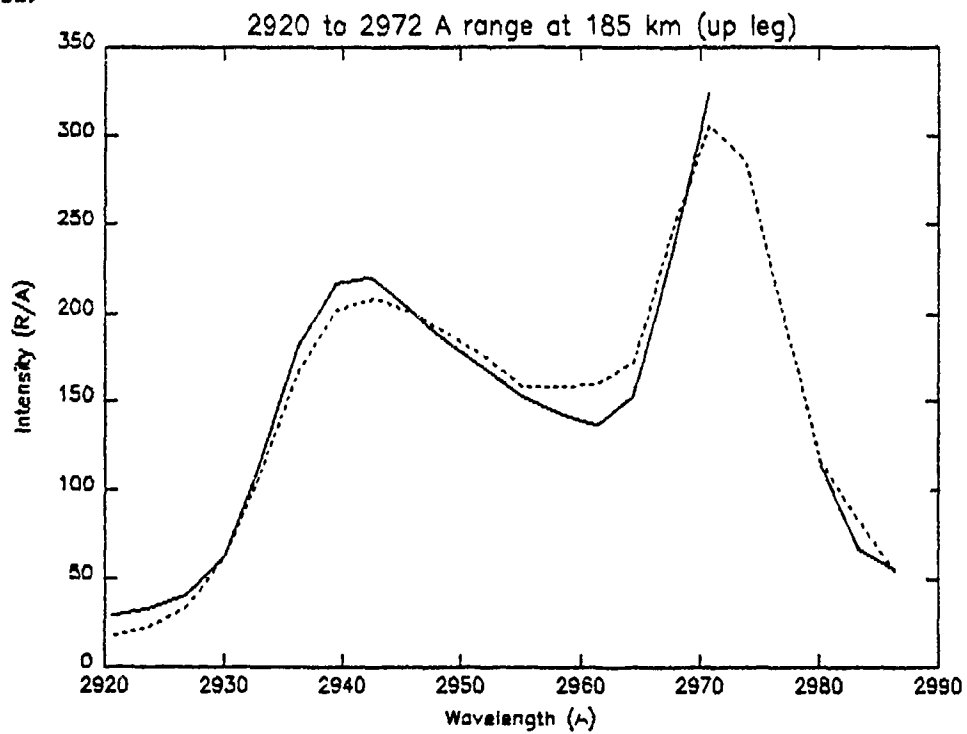
IDL>



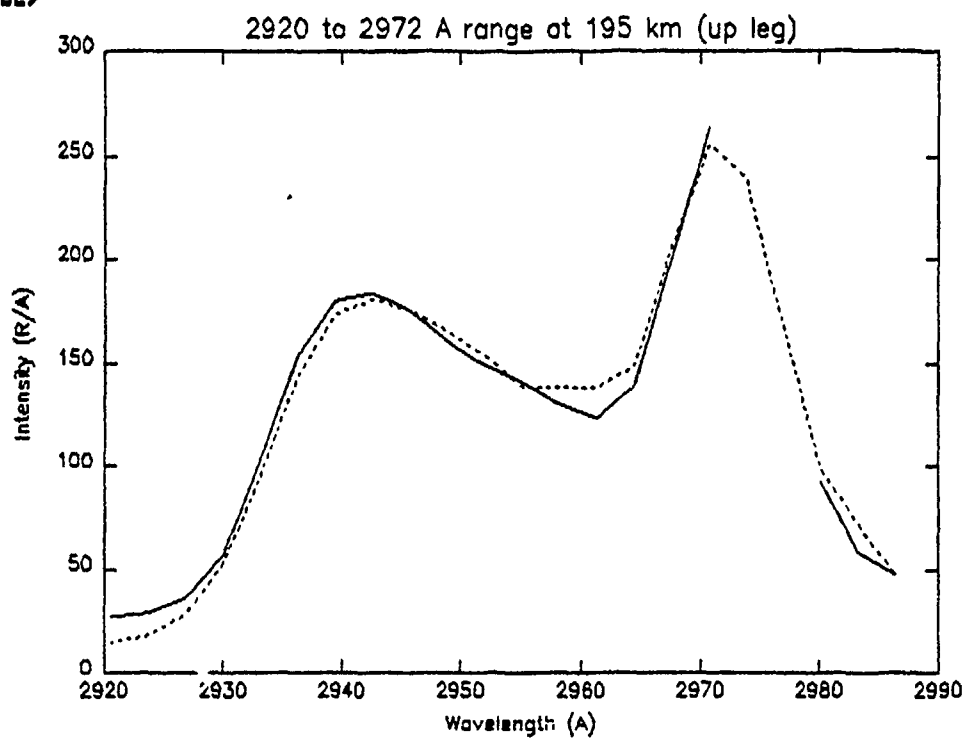
IDL>



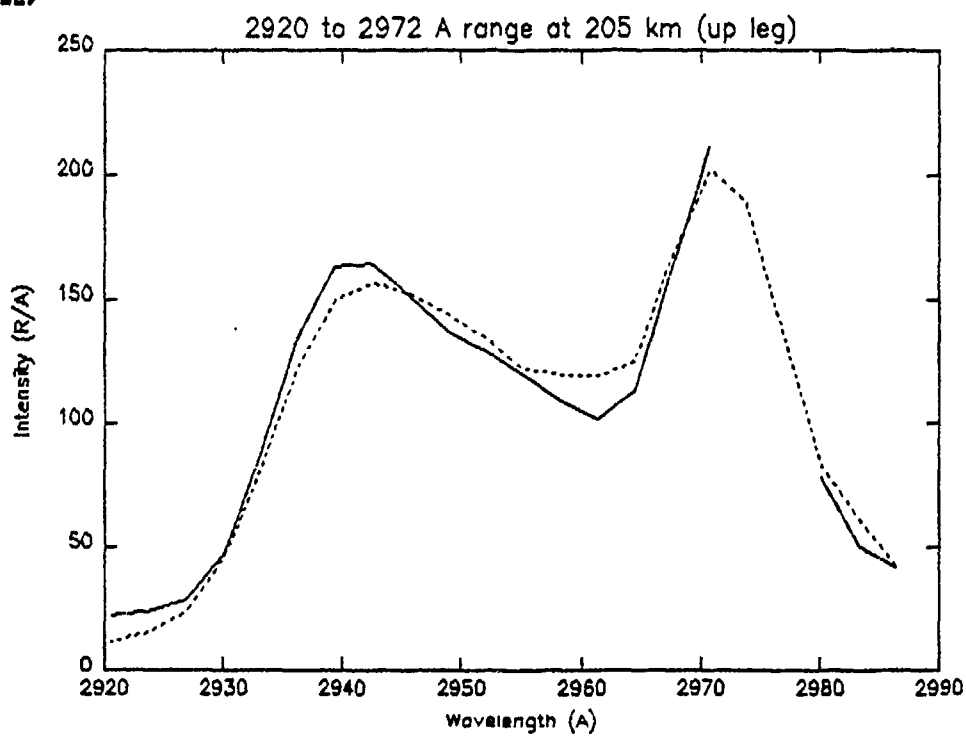
IDL>



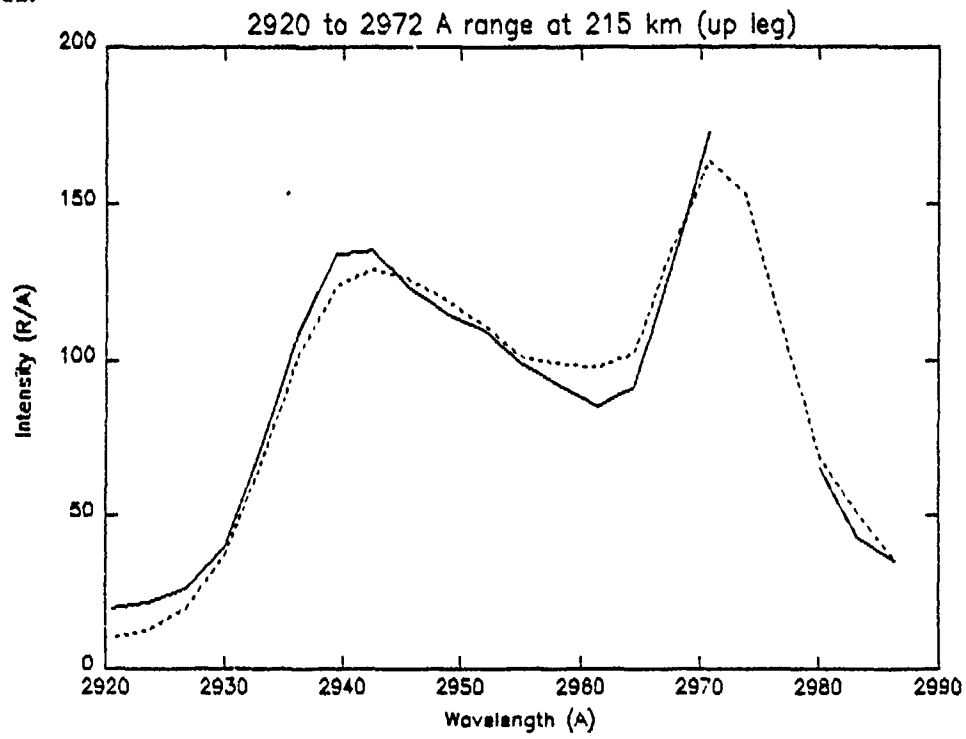
IDL>



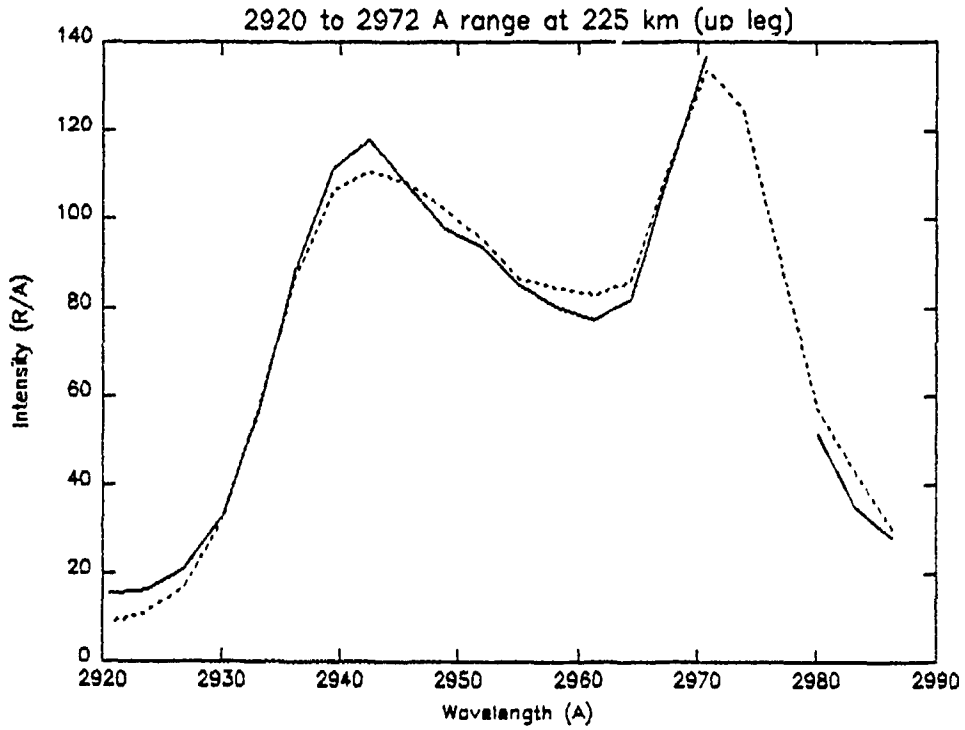
IDL>



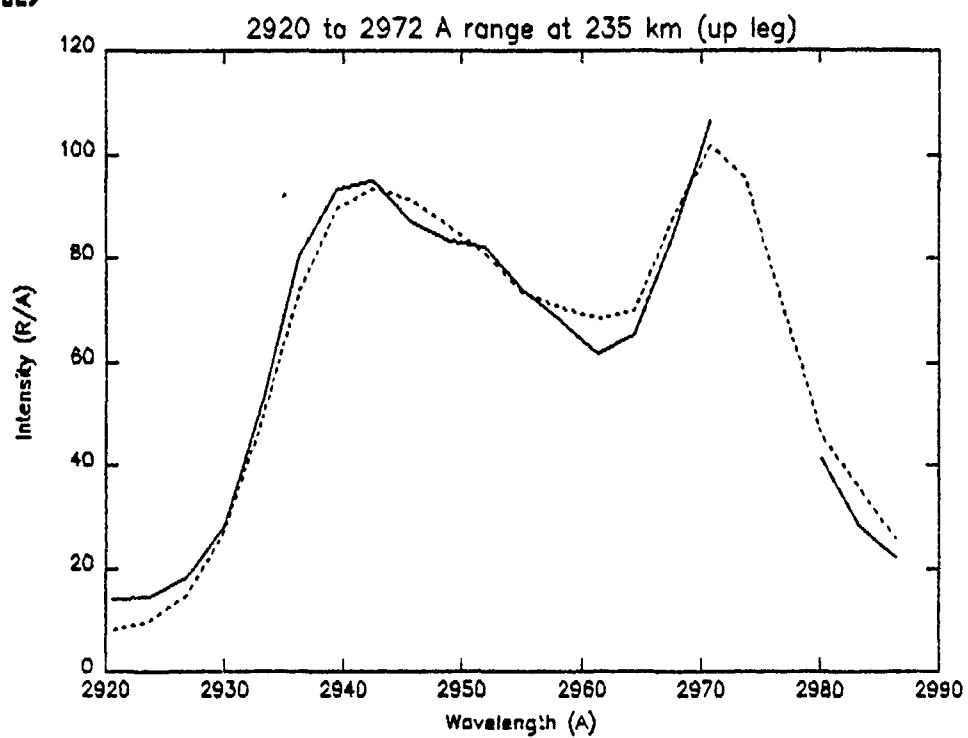
IDL>



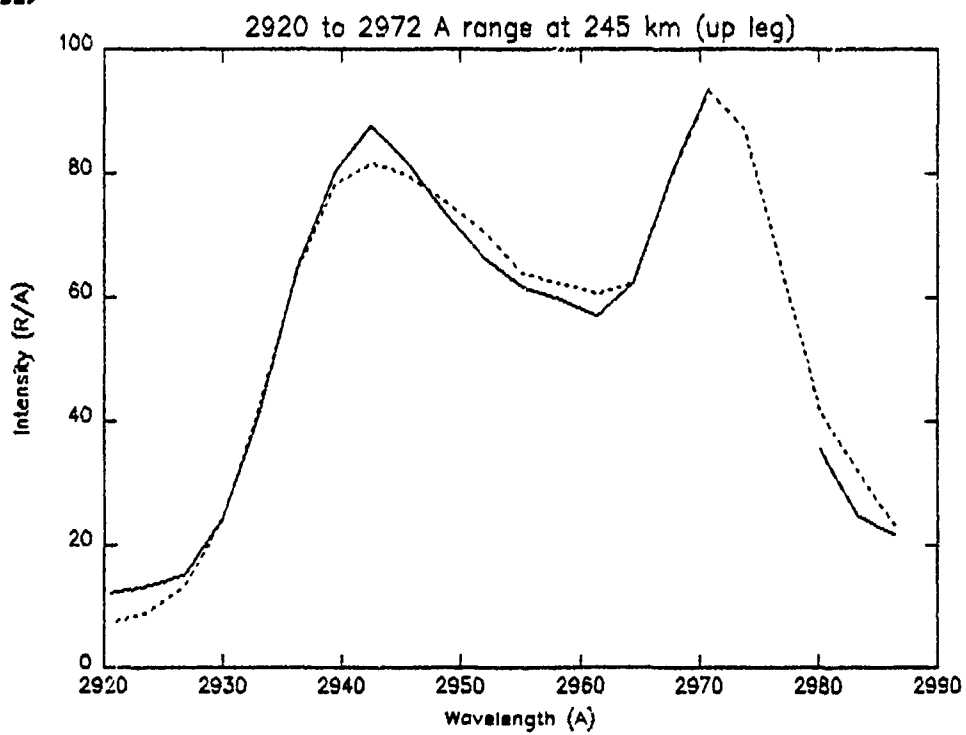
IDL>



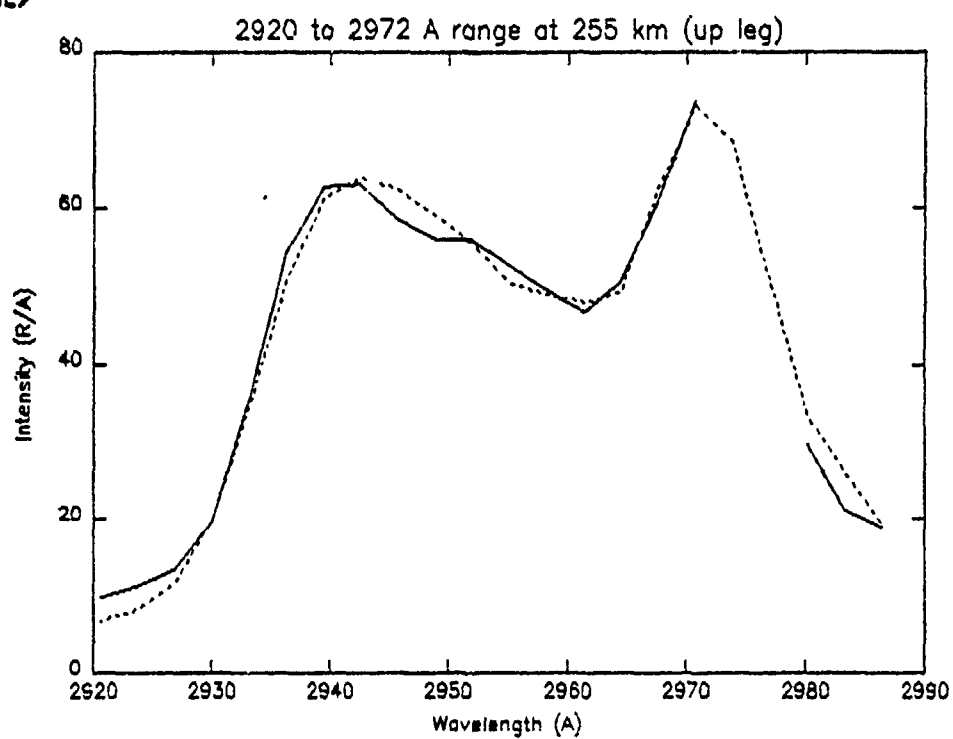
IDL>



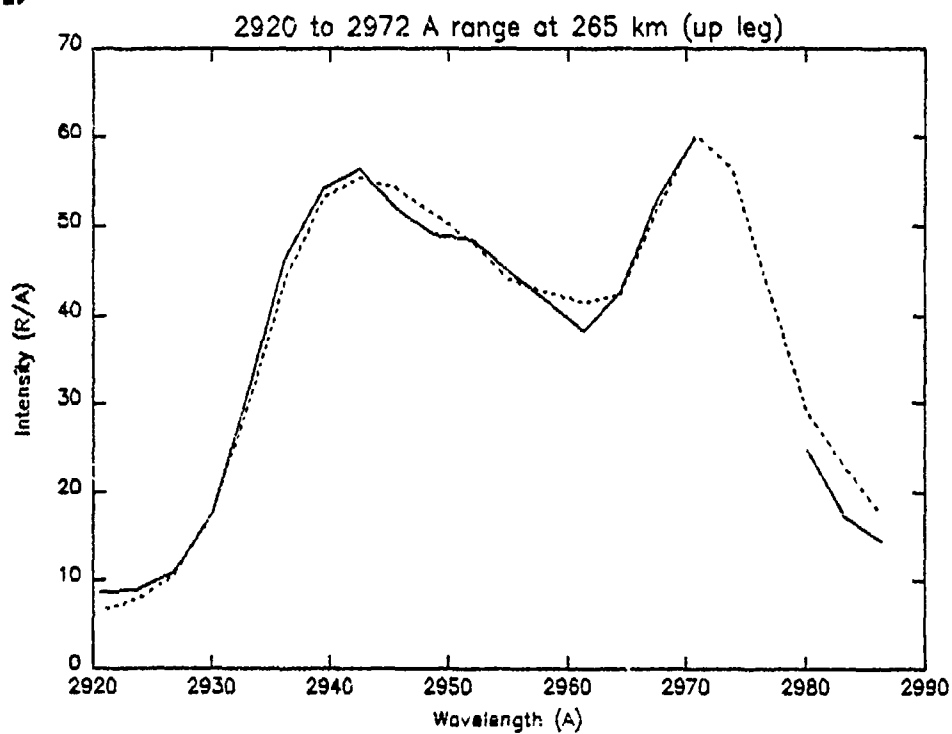
IDL>



IDL>

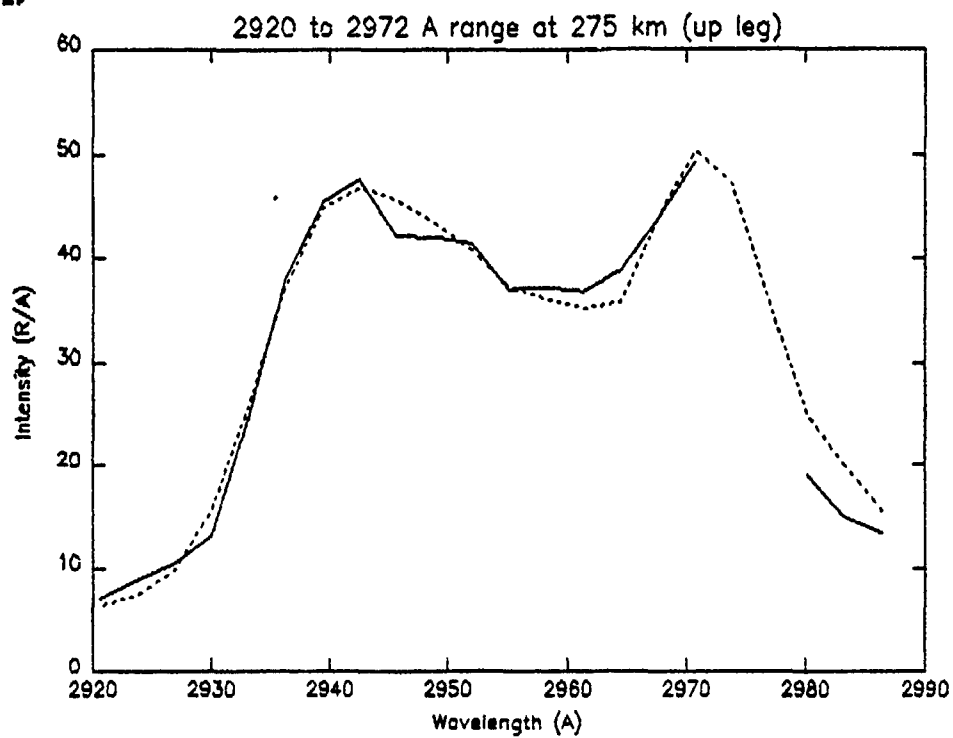


IDL>

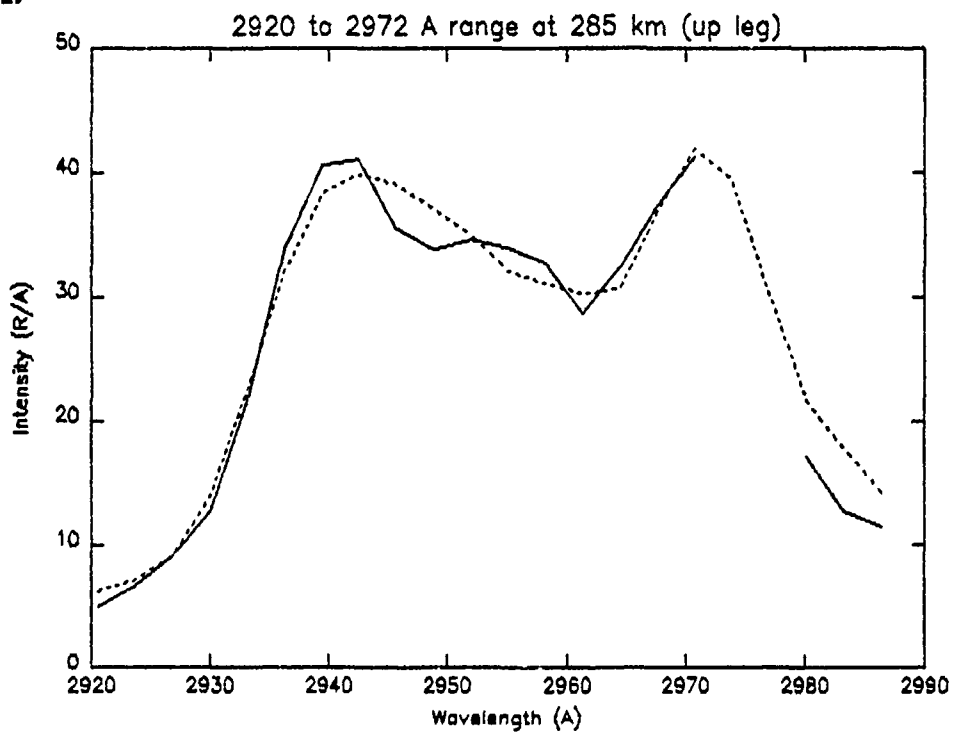




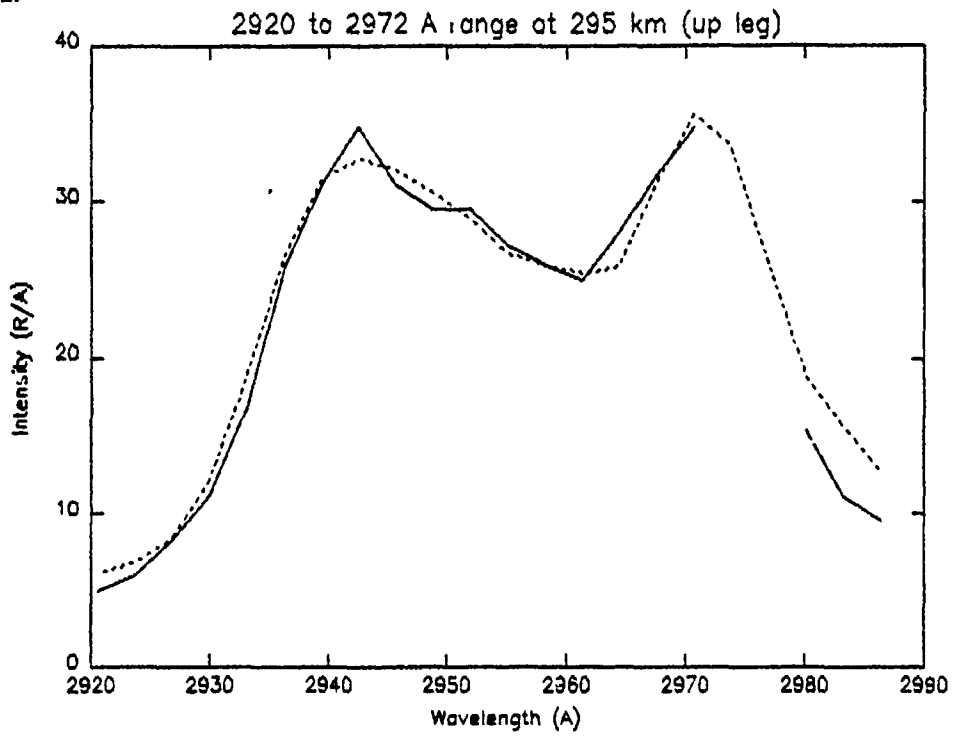
IDL>



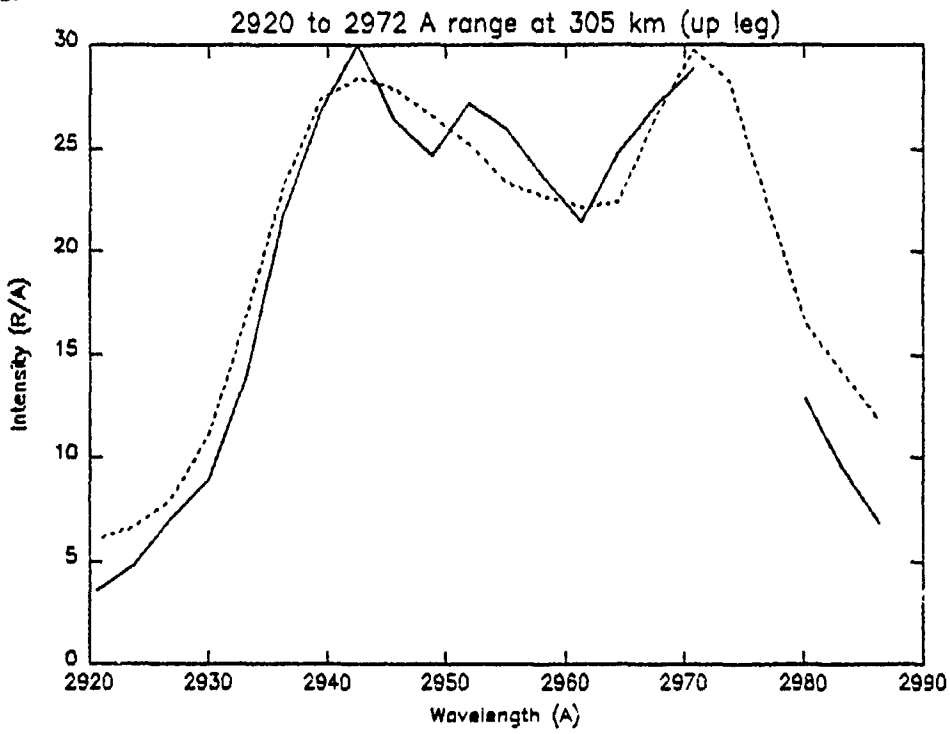
IDL>



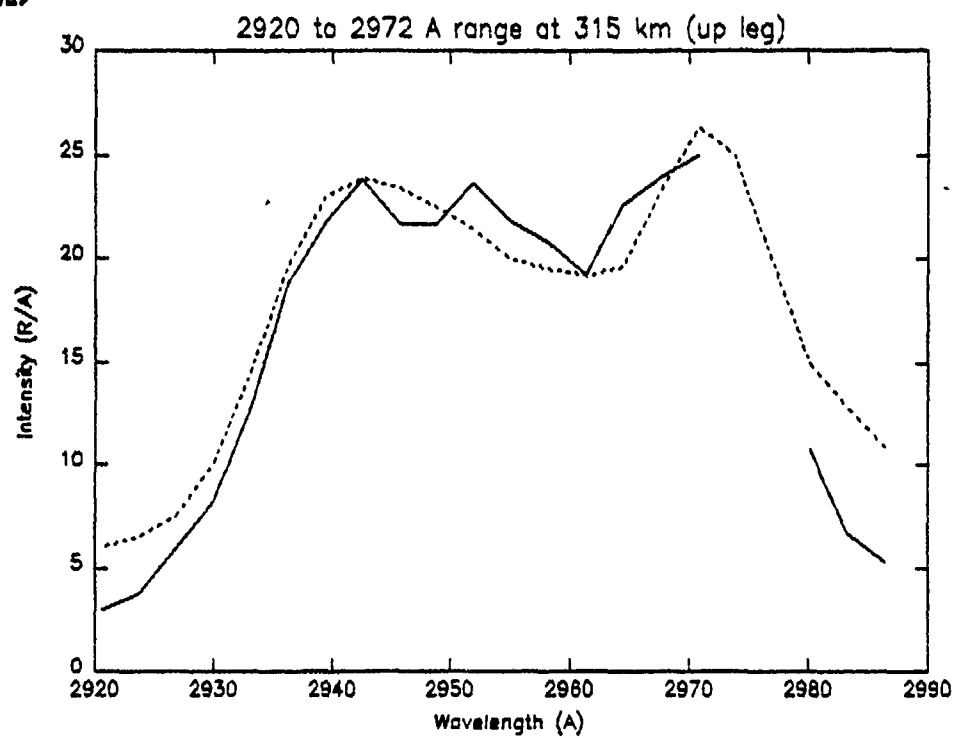
IDL>



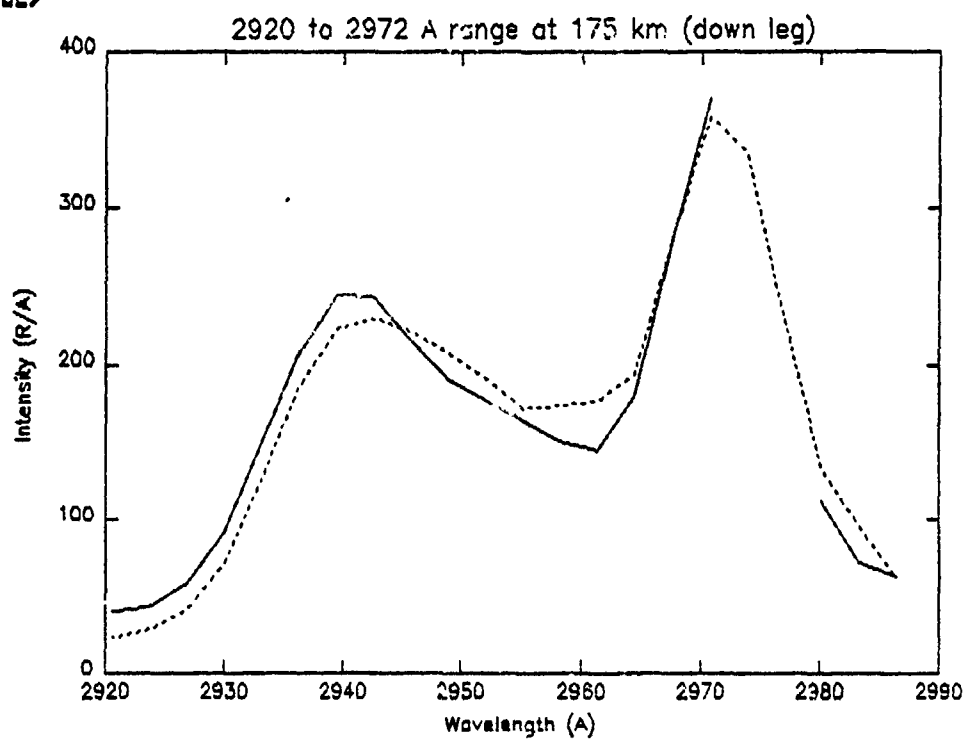
IDL>



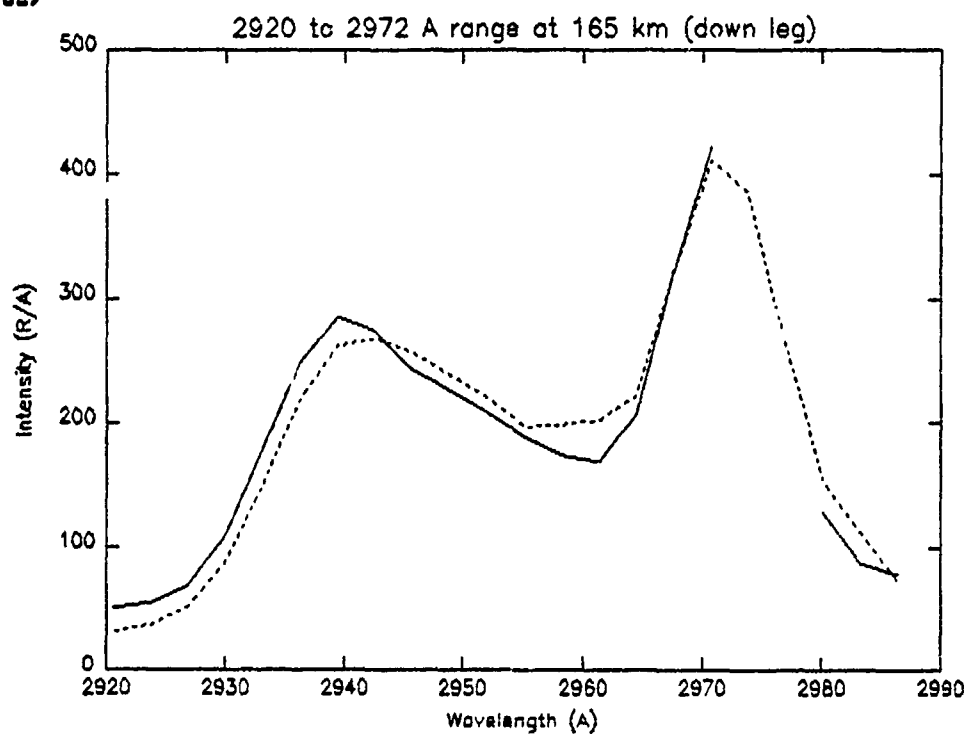
IDL>



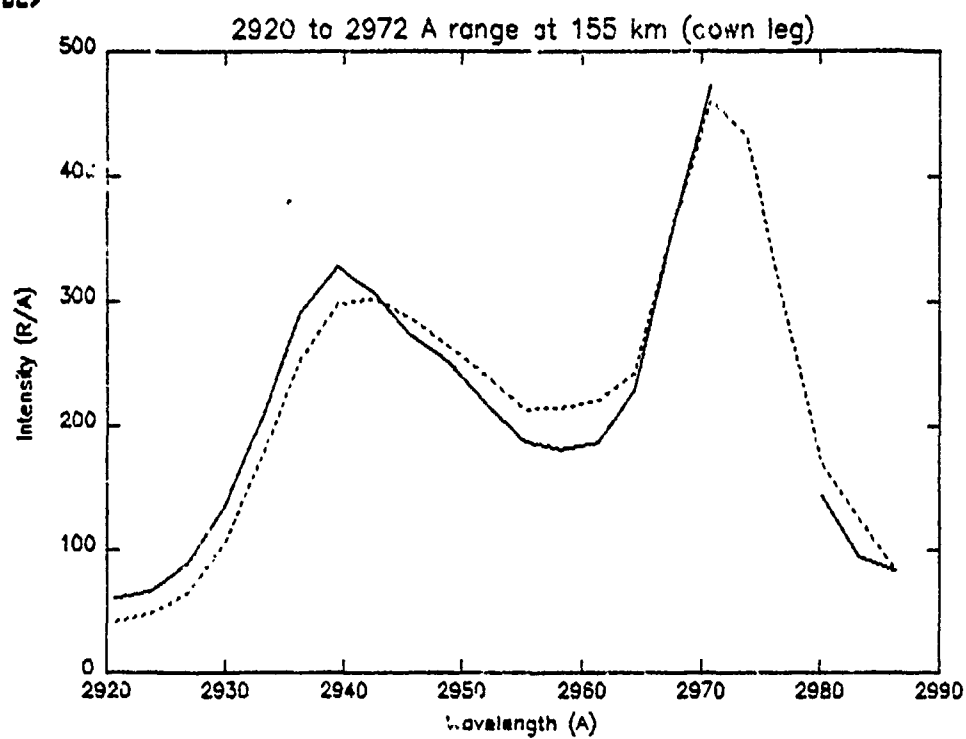
IDL>



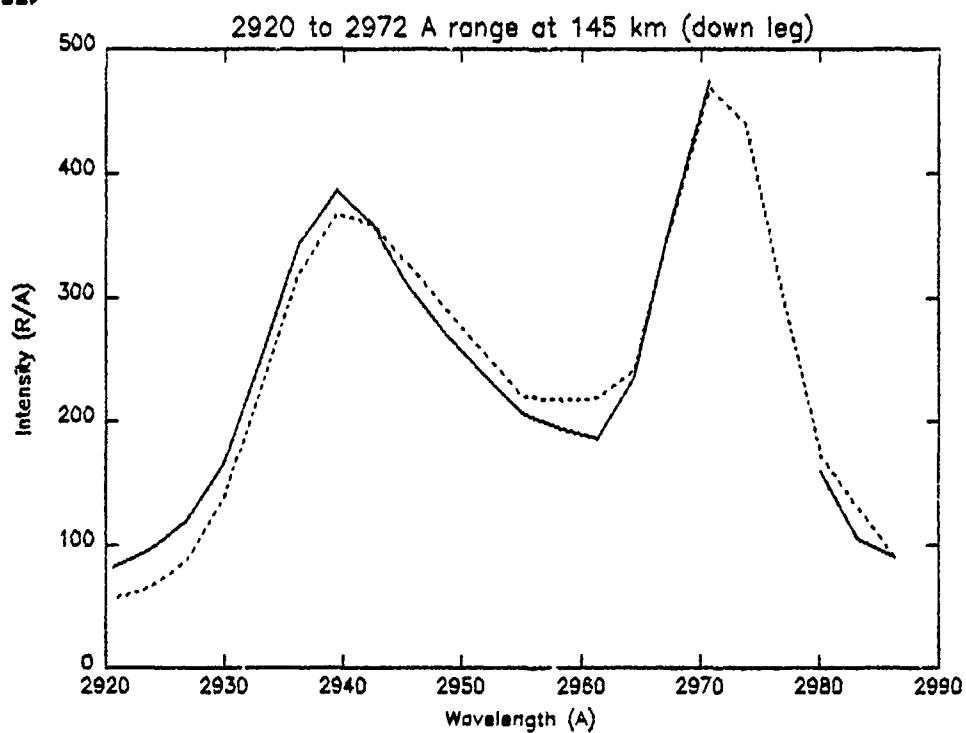
IDL>



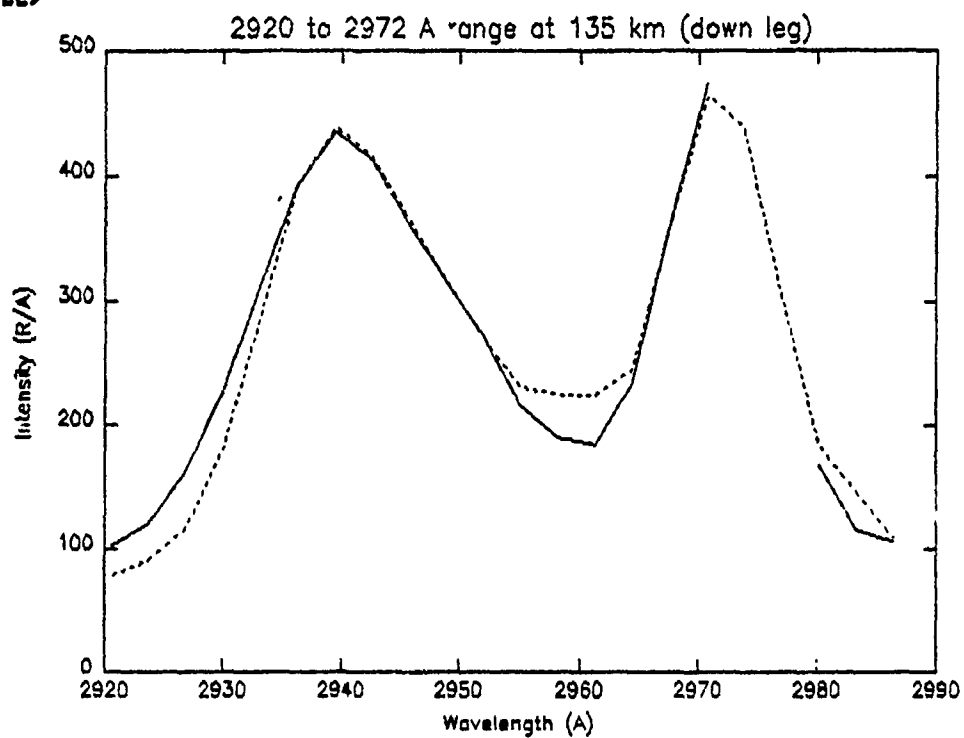
IDL>



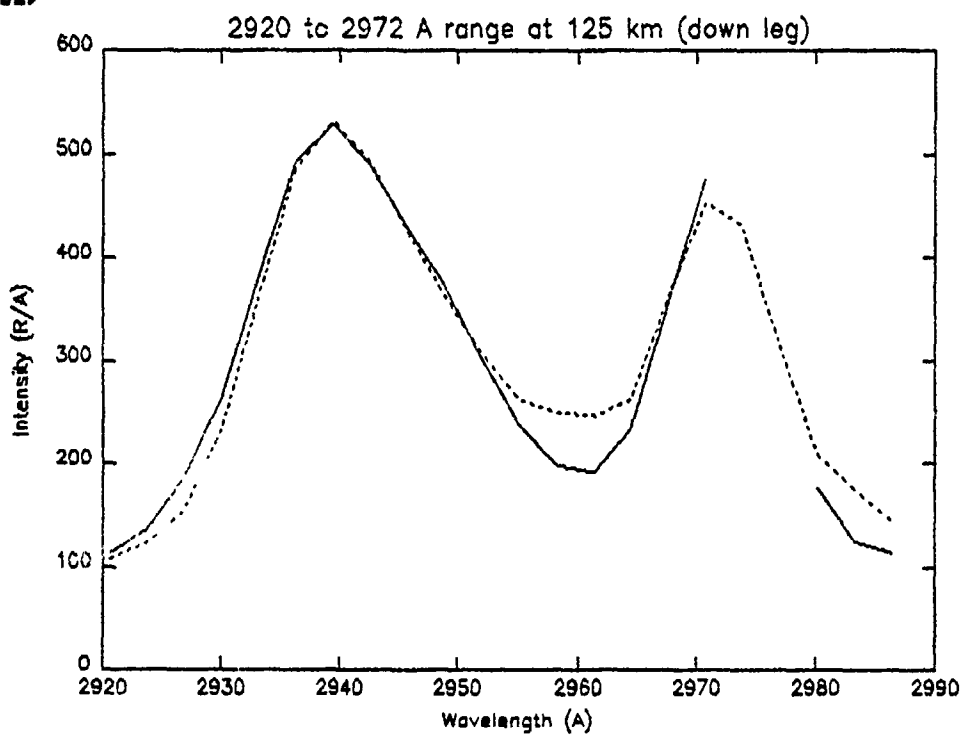
IDL>



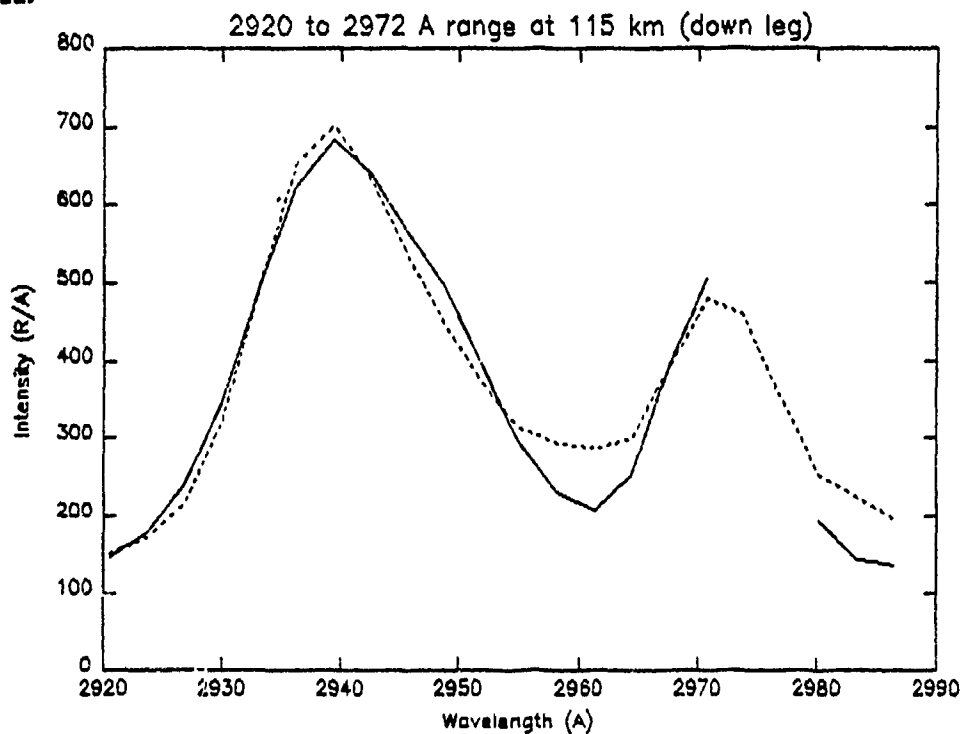
IDL>



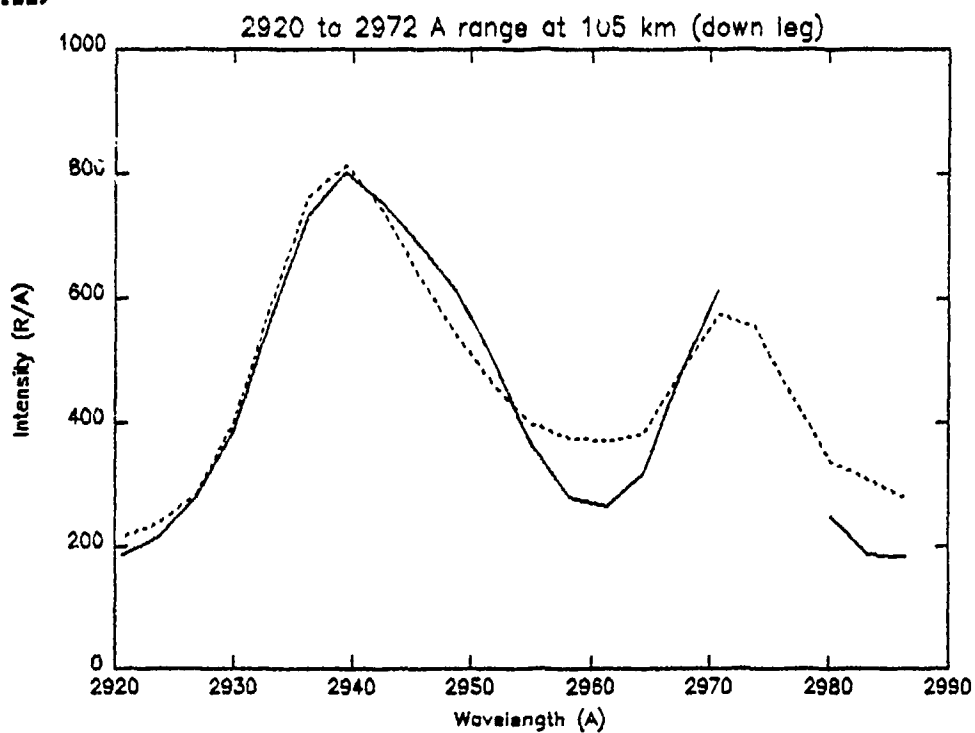
IDL>



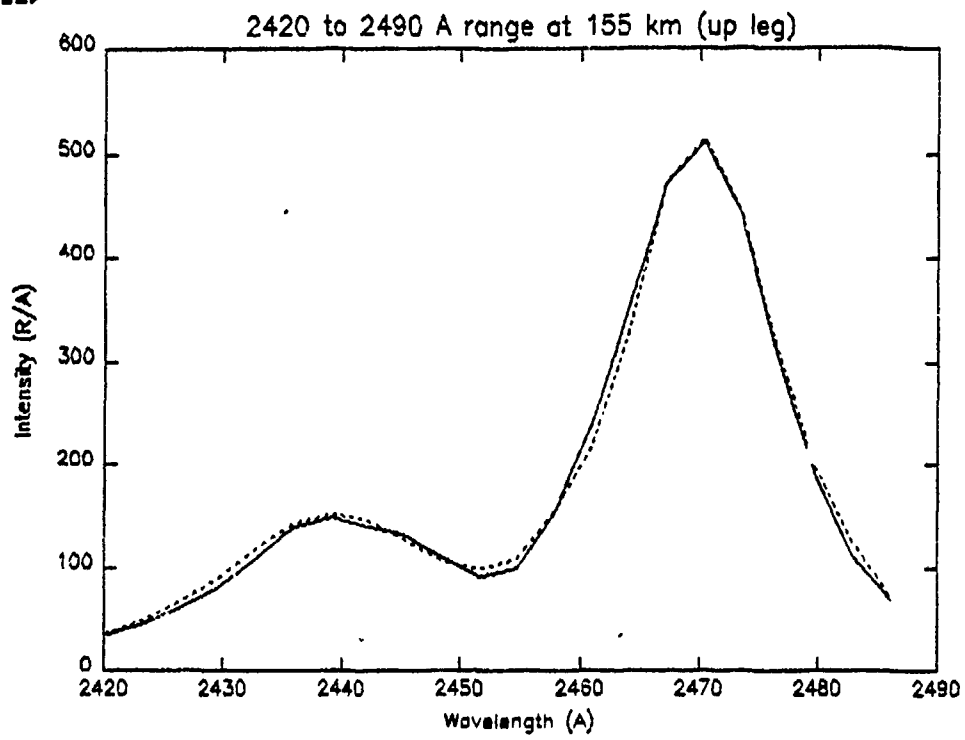
IDL>



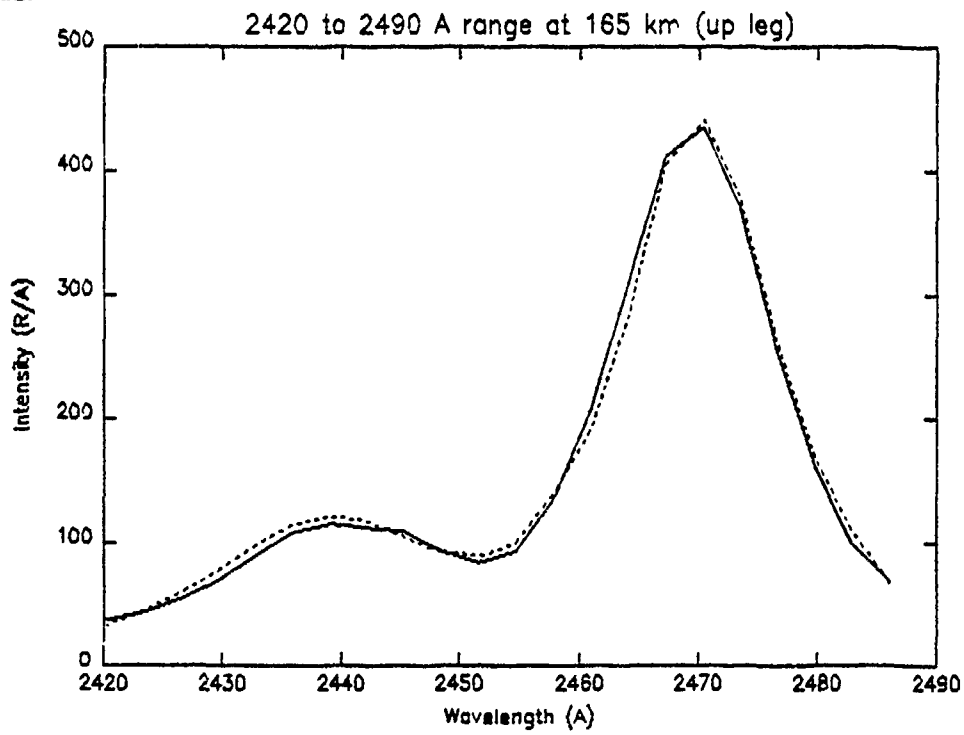
IDL>



IDL>

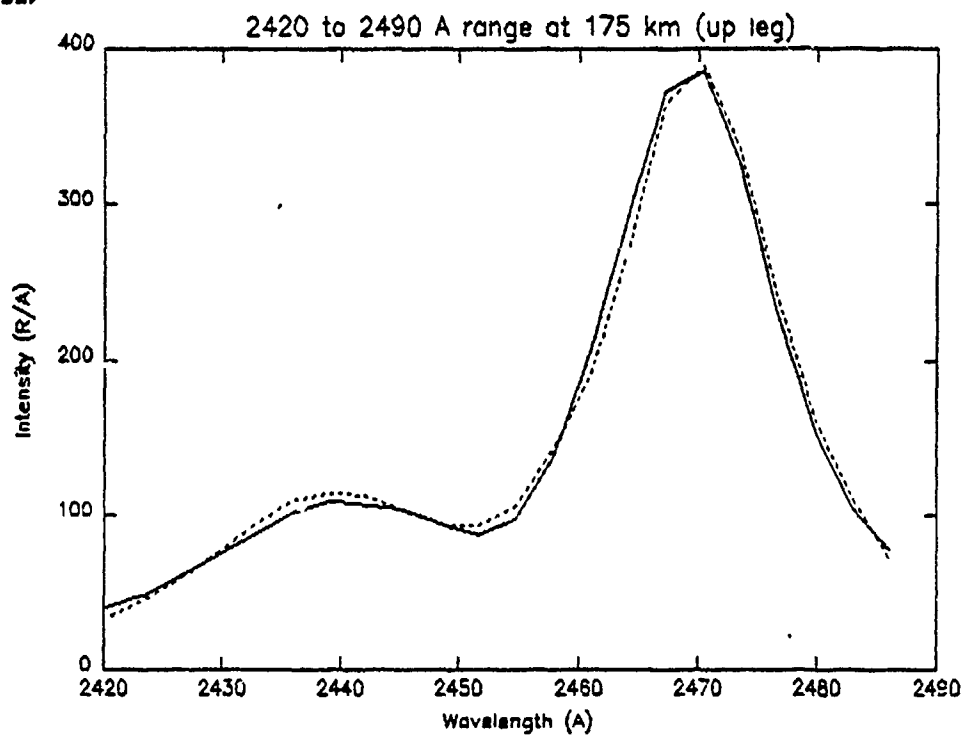


IDL>

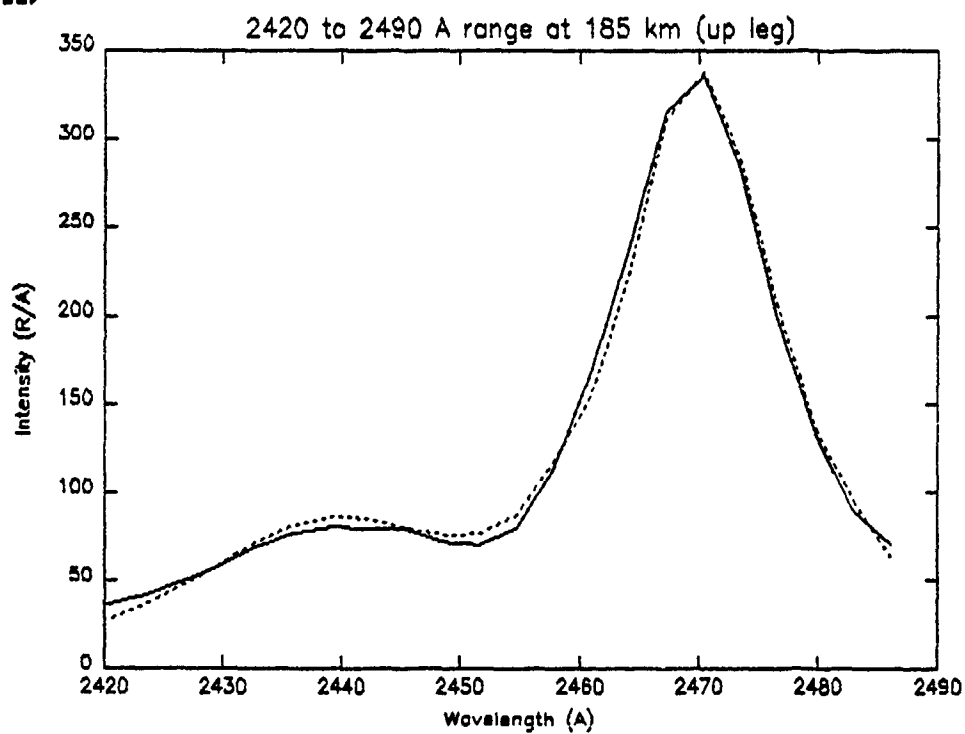




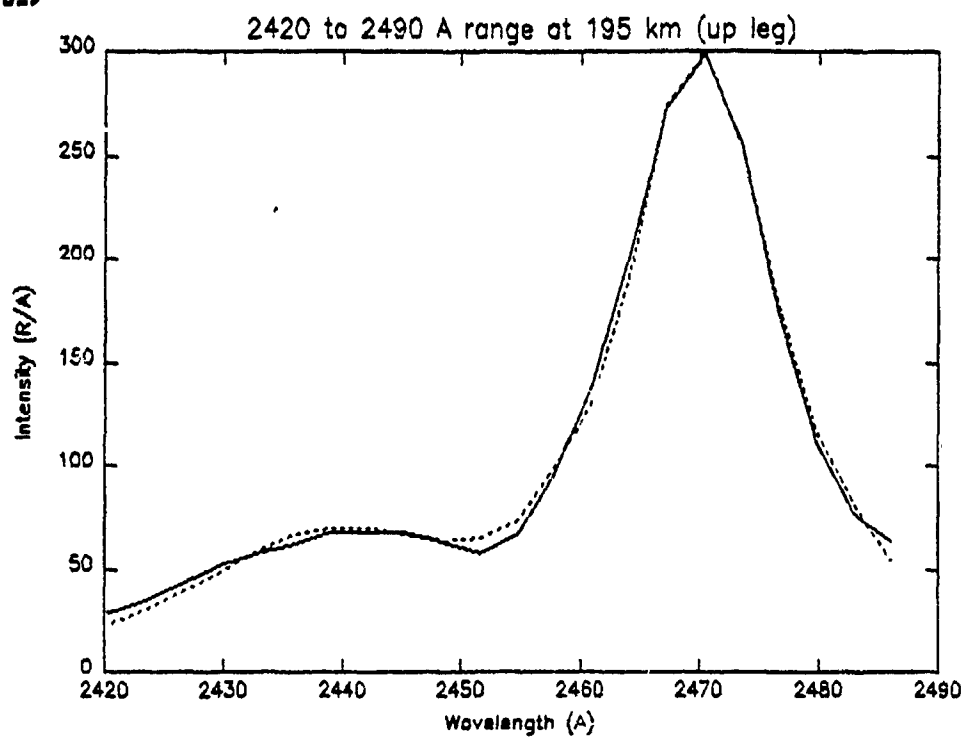
IDL>



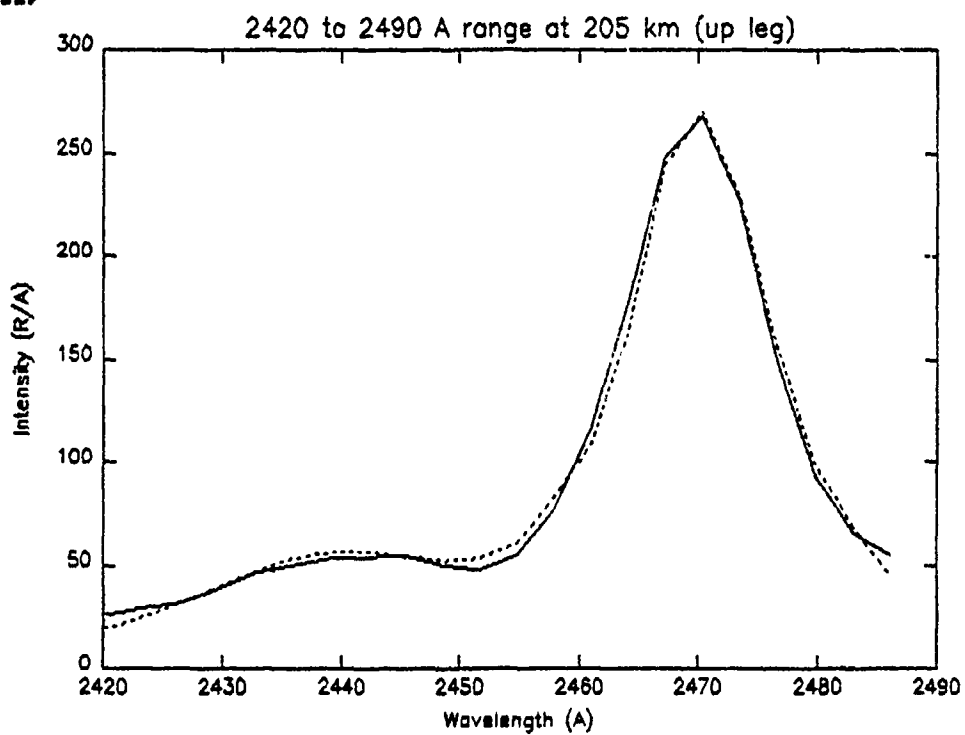
IDL>



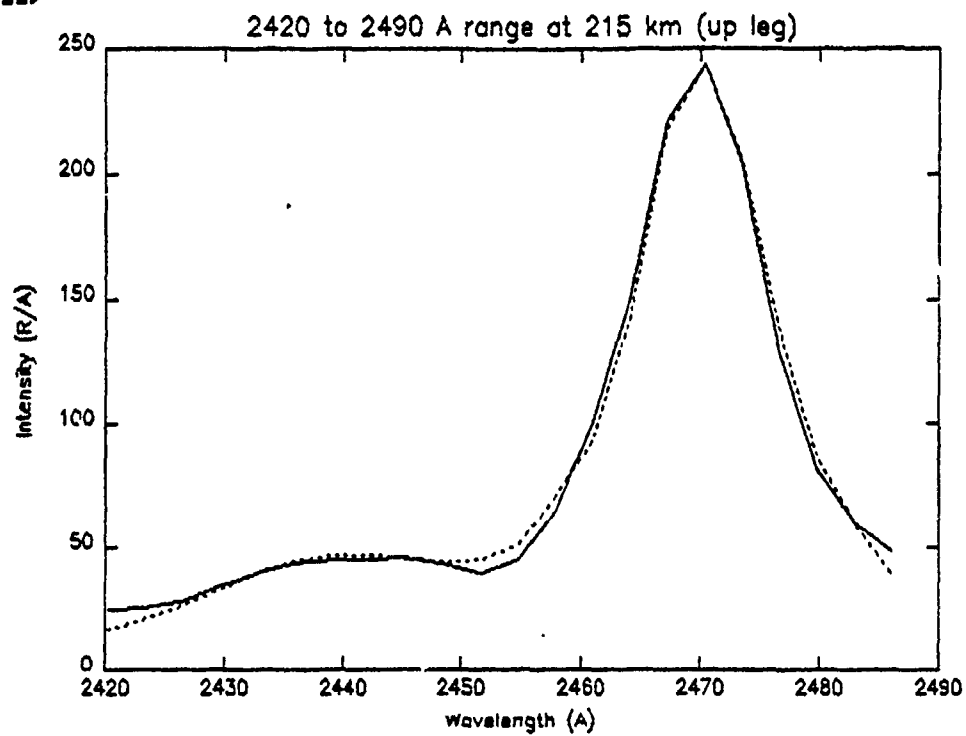
IDL>



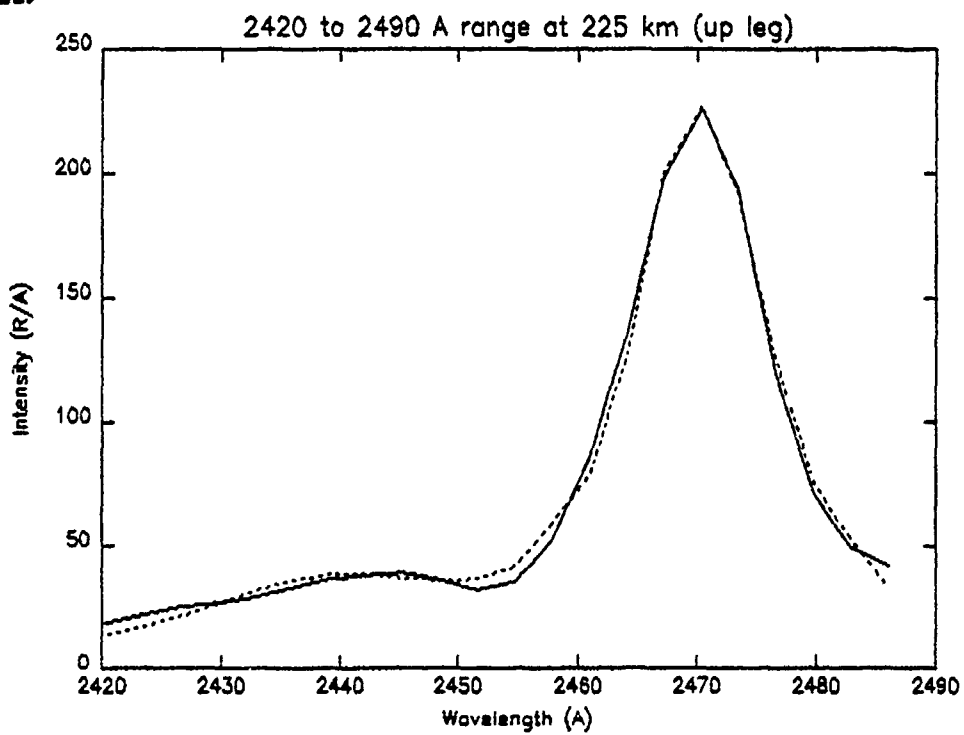
IDL>



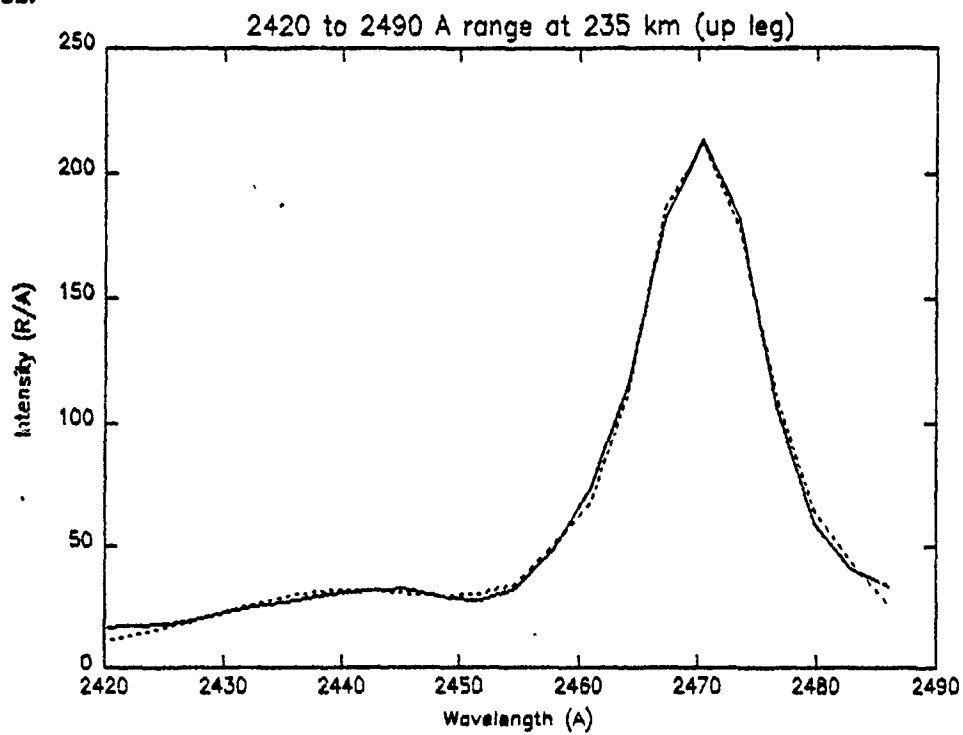
IDL>



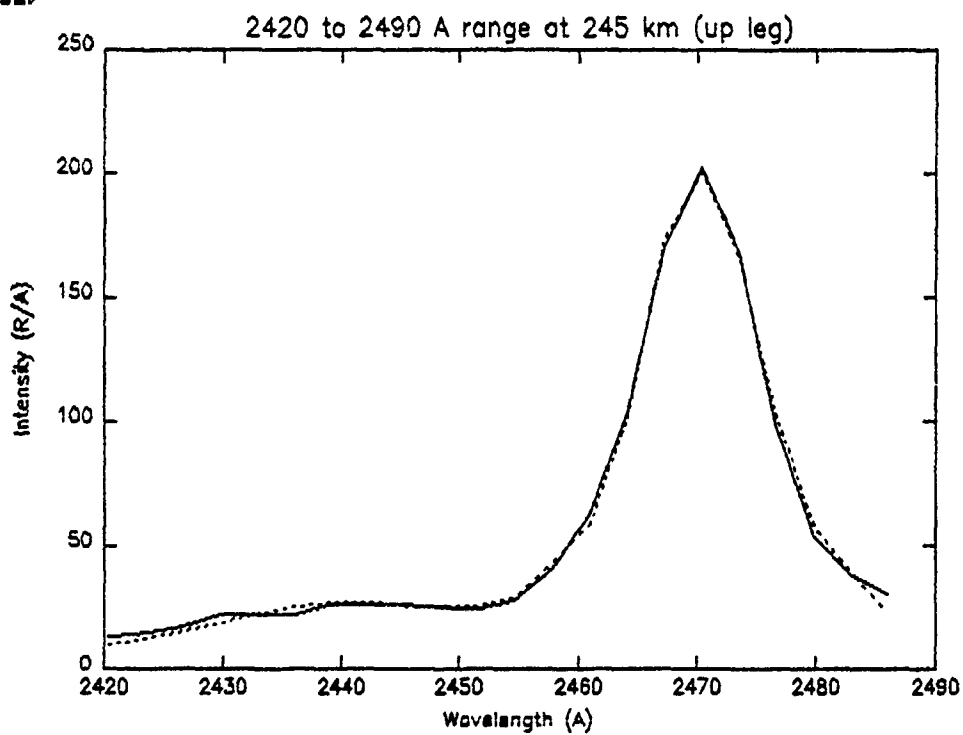
IDL>



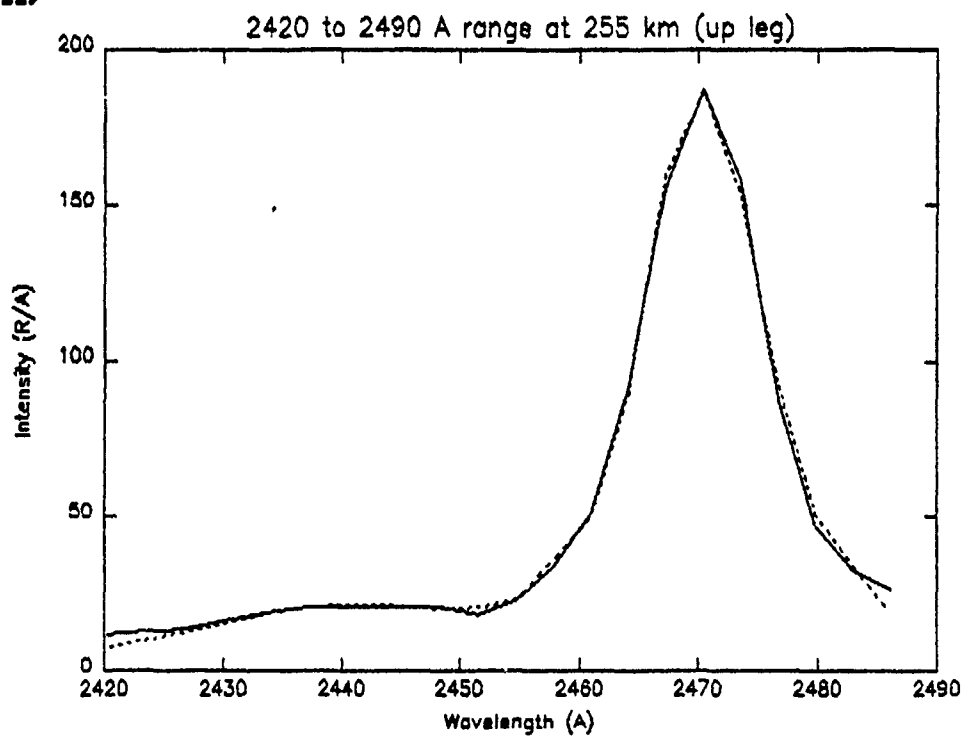
IDL>



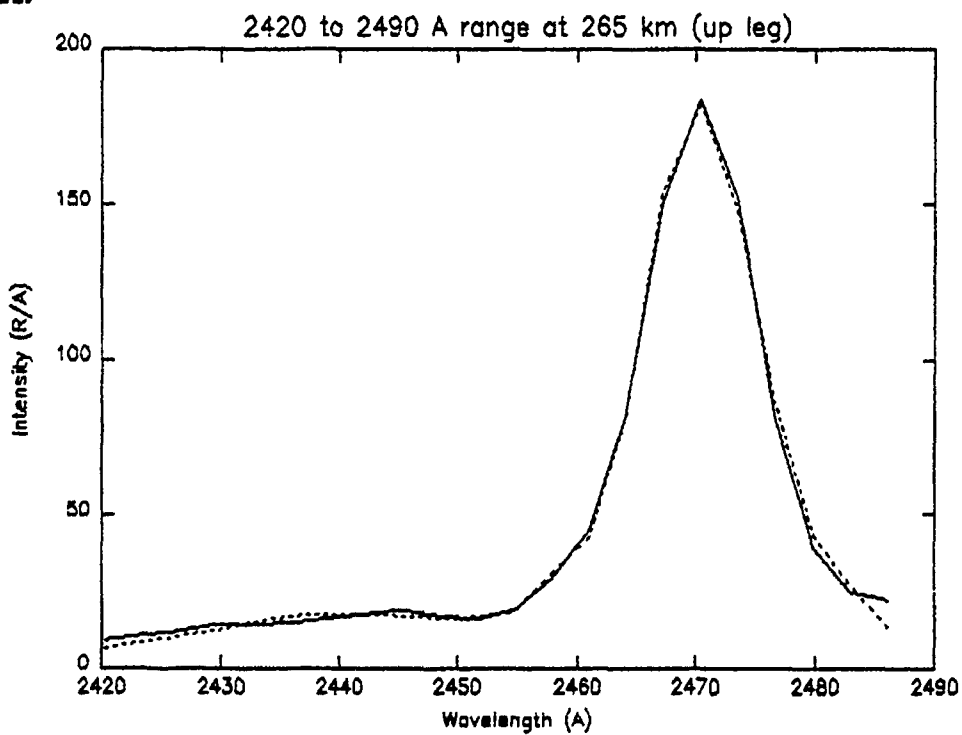
IDL>



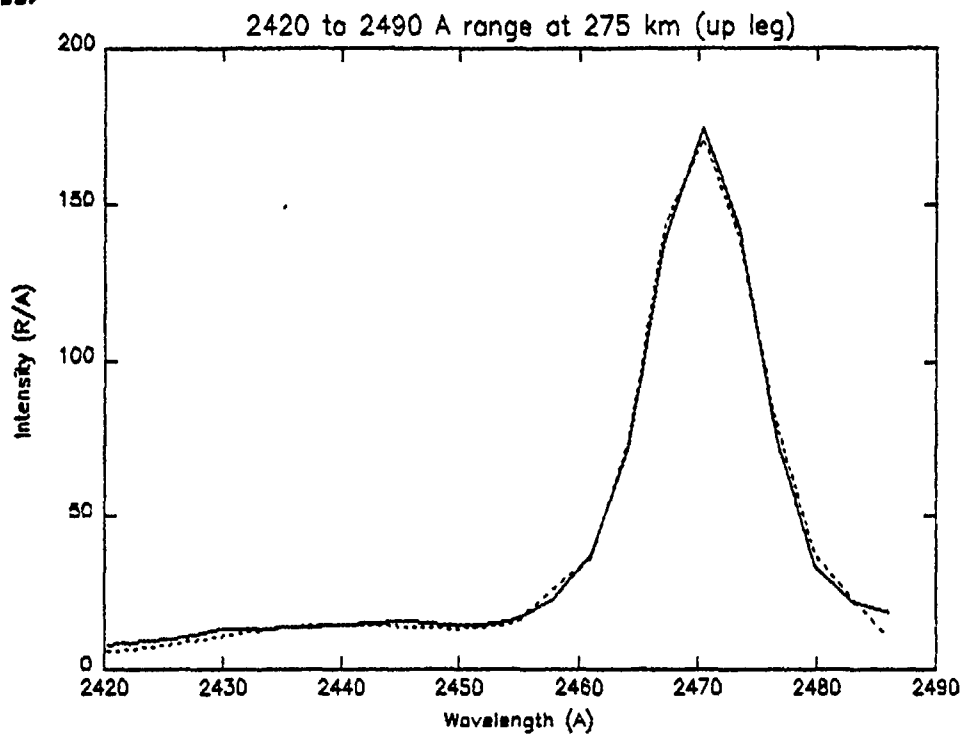
IDL>



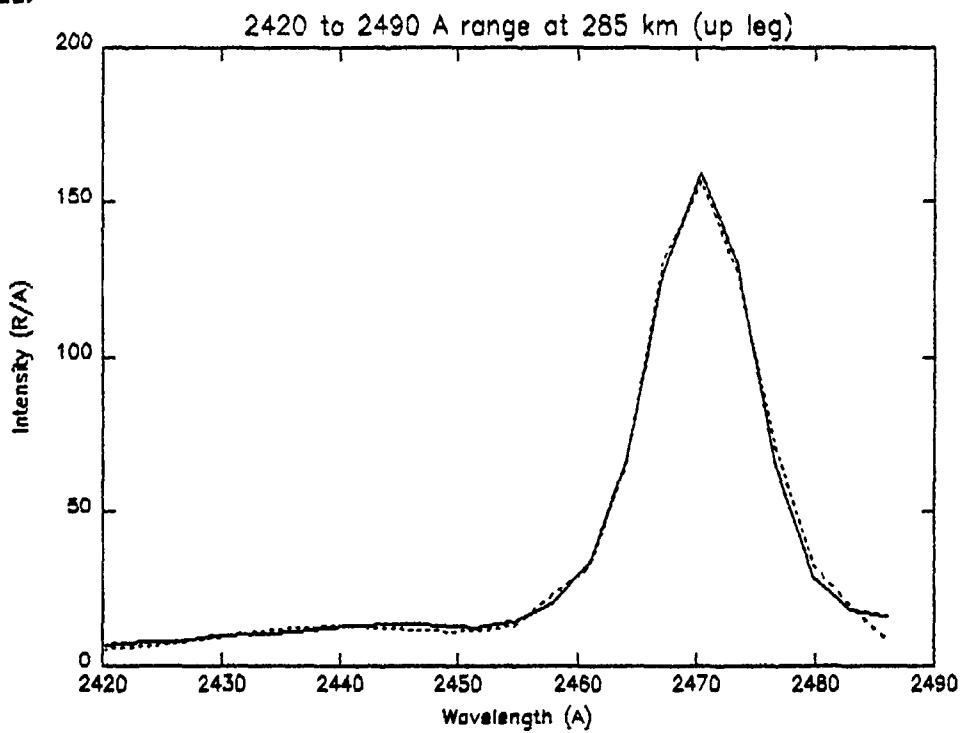
IDL>



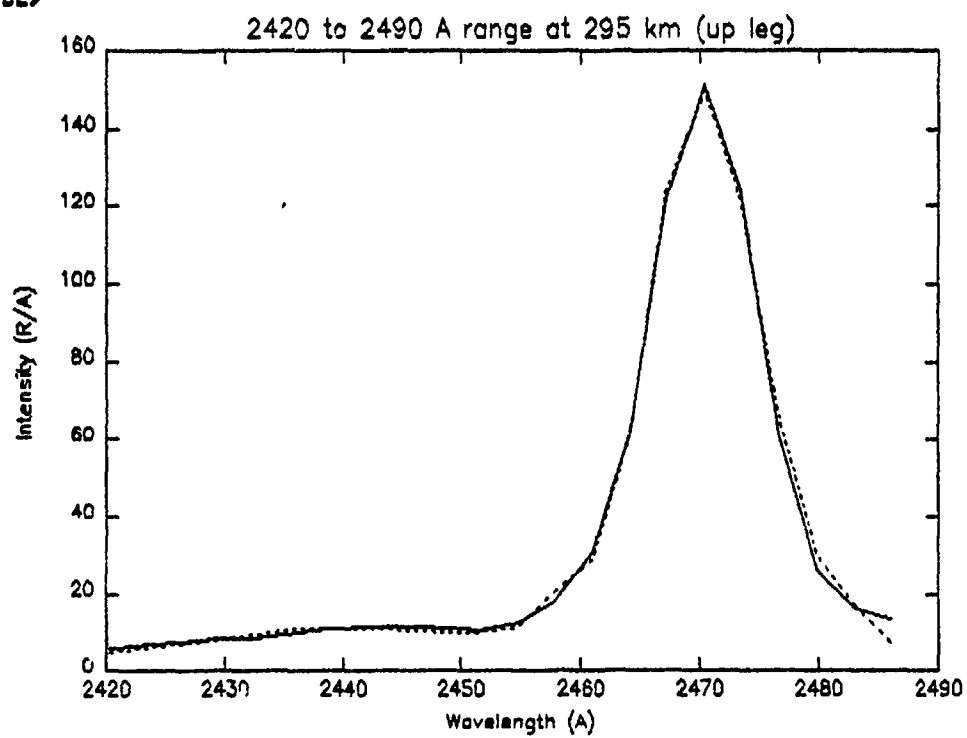
IDL>



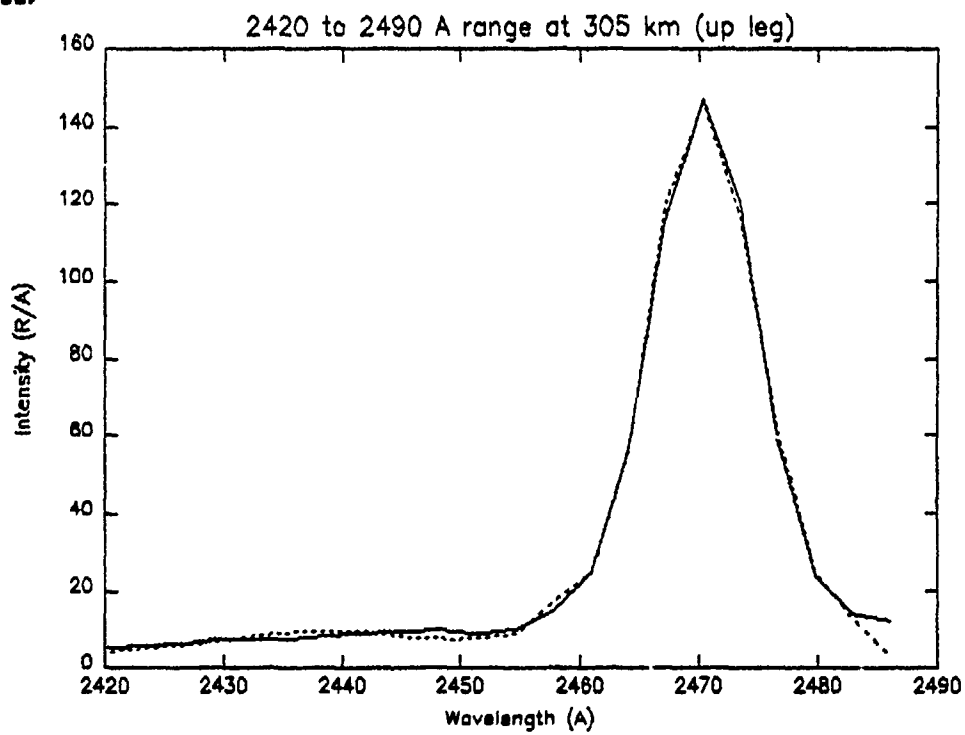
IDL>



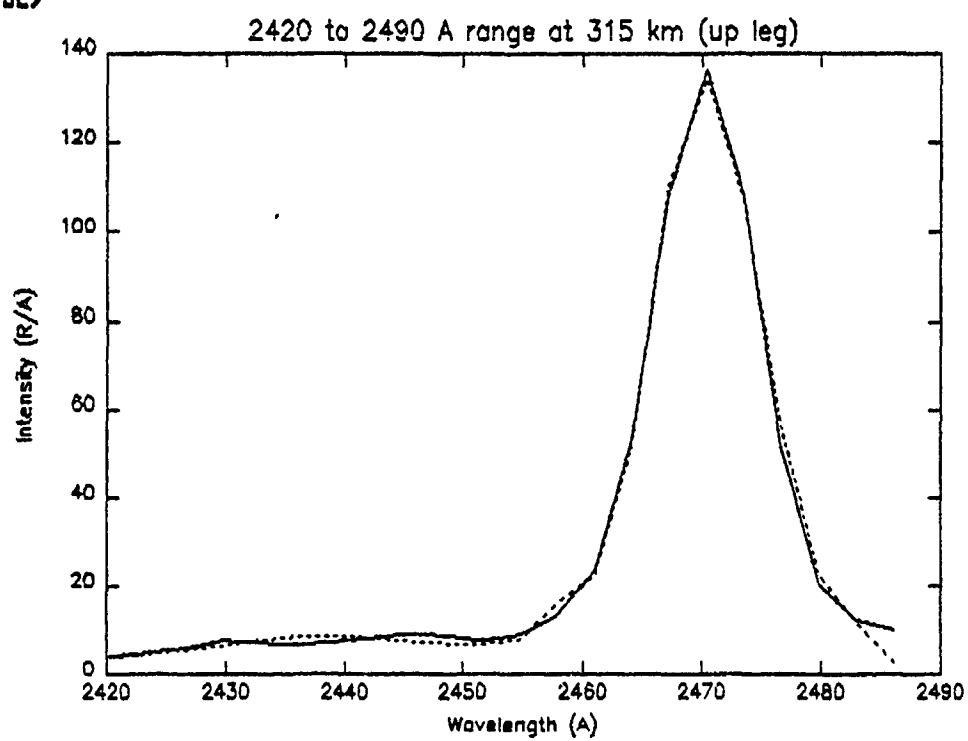
IDL>



IDL>

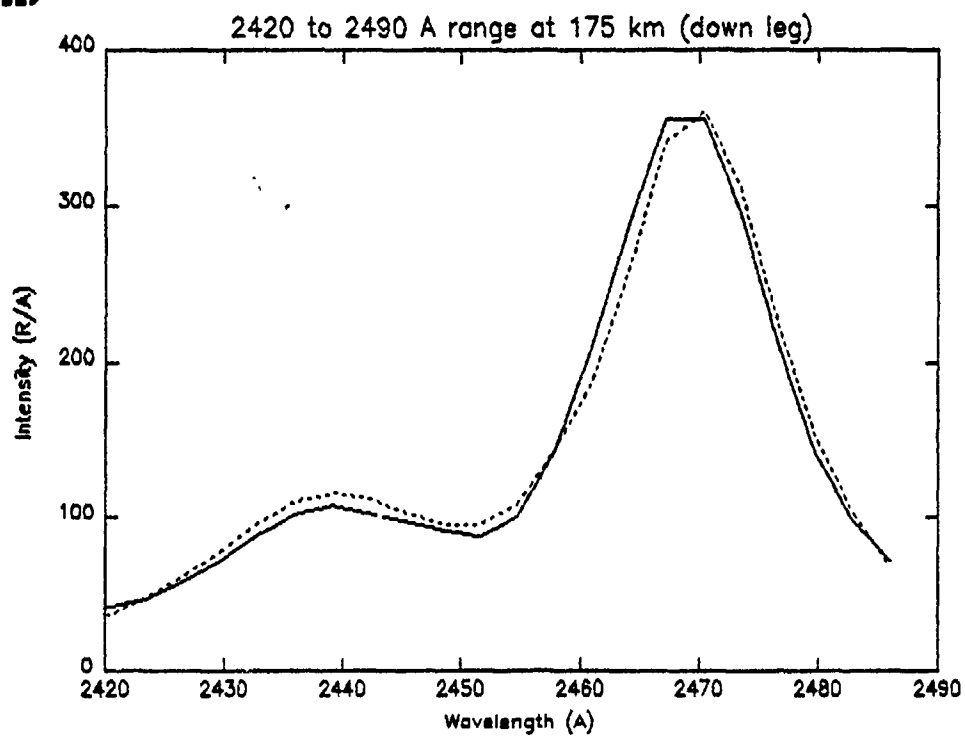


10L>

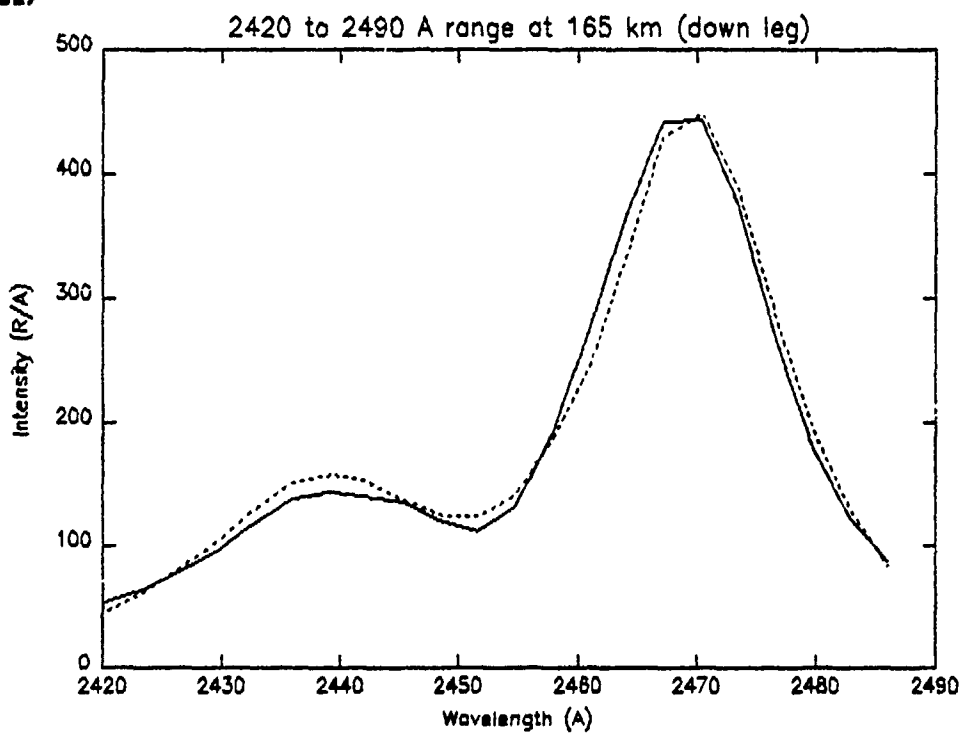




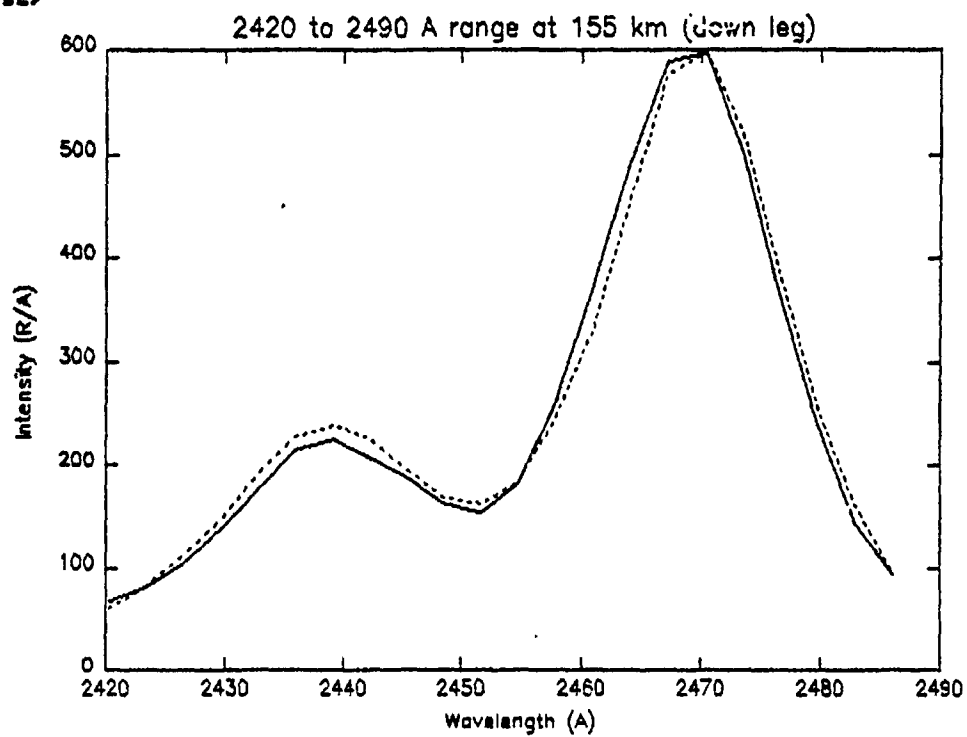
IDL>



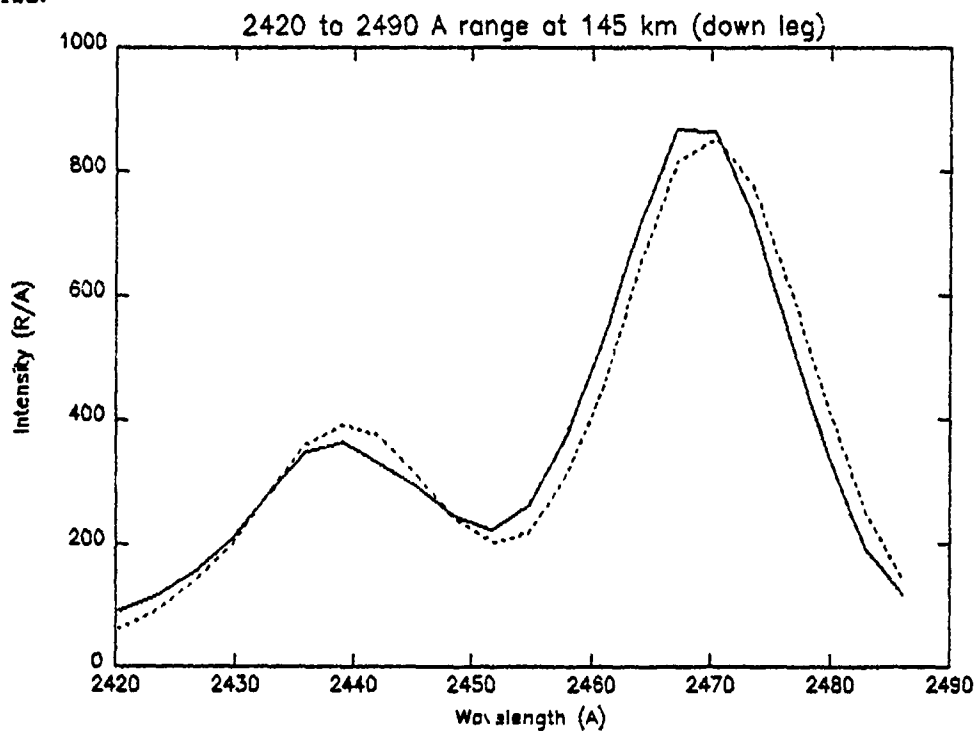
IDL>



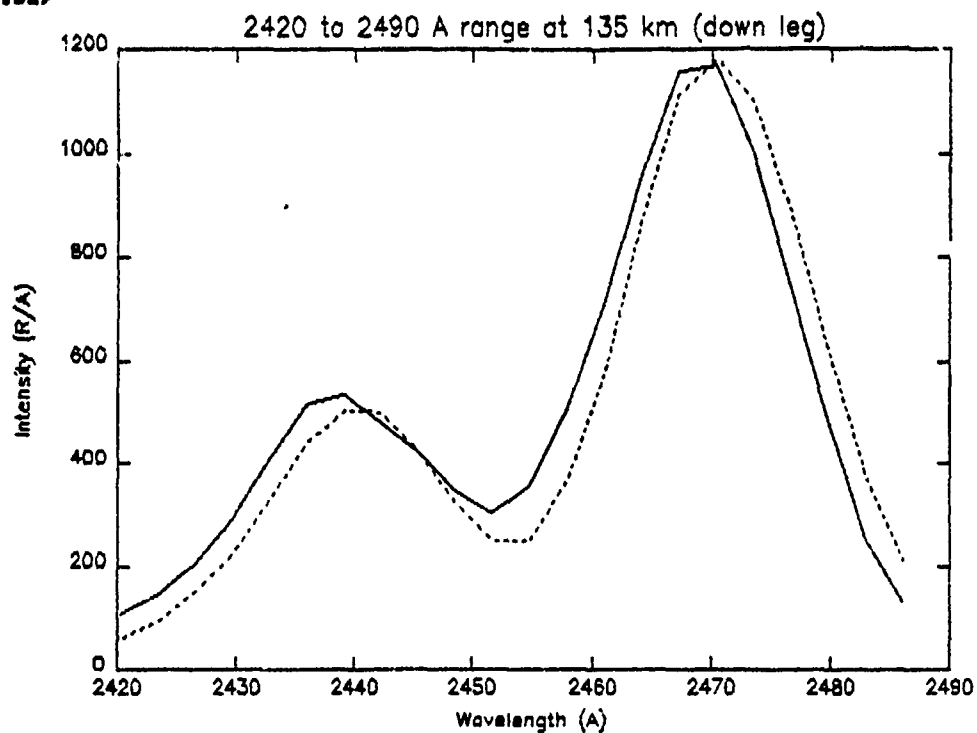
IDL>



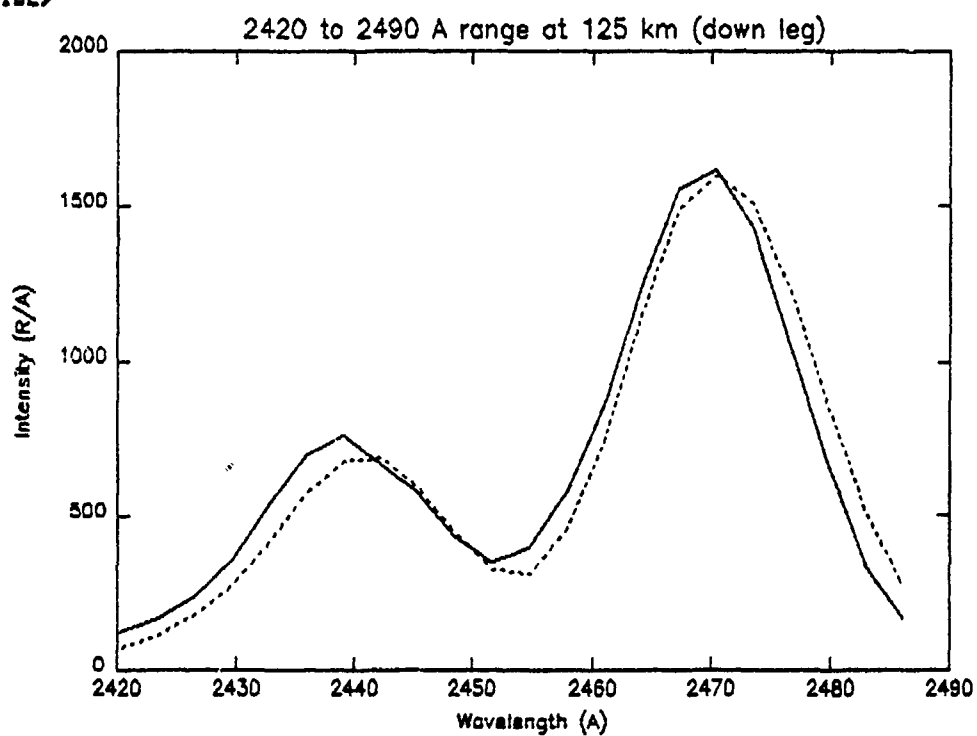
IDL>



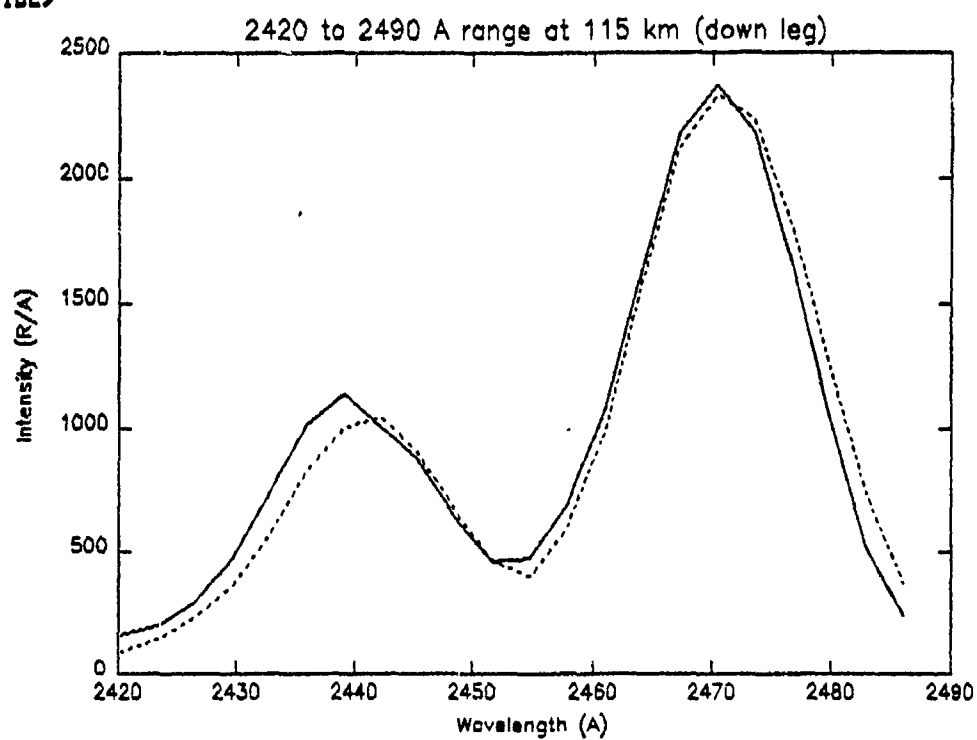
IDL>



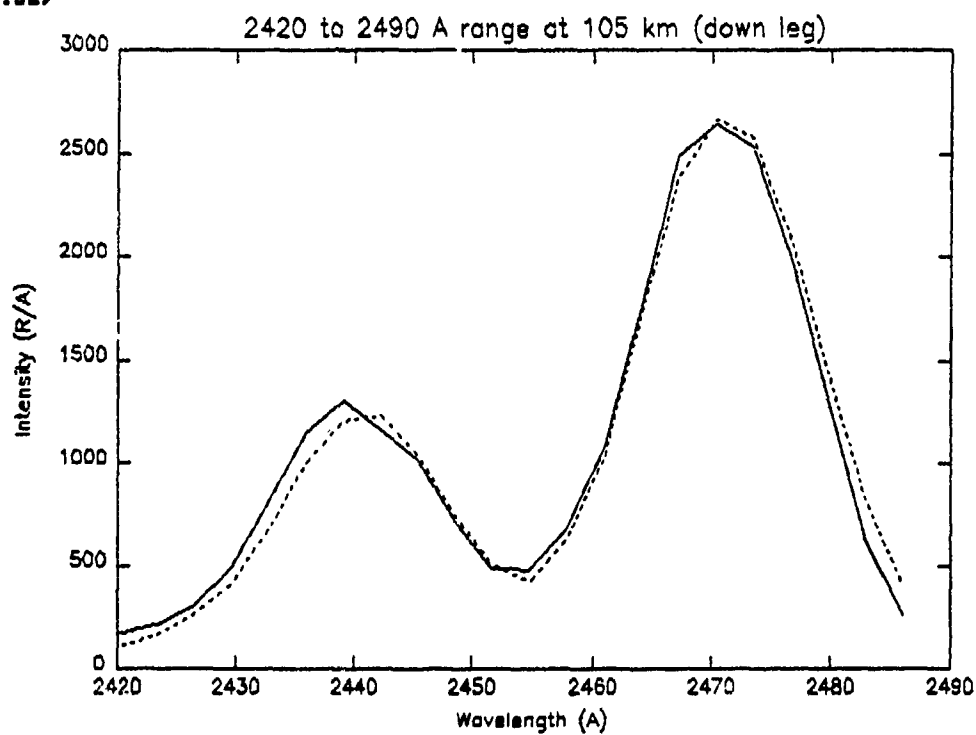
IDL>



IDL>



IDL>



## BIBLIOGRAPHY

Anderson, D.E., and Meier, R.R., "The OII 834 Å Dayglow: A general model for excitation rate and intensity calculations," *Planetary Space Science*, 33, 1179, 1985.

Banks, P.M., and Kockarts, G., *Aeronomy*, Part A, Academic Press, 1973.

Bevington, P.R., *Data Reduction and Error Analysis for the Physical Sciences*, McGraw-Hill, Inc., 1969.

Bosserman, J.L., *Analysis of Thermospheric Dayglow Spectra From the Spacelab 1 Shuttle Mission*, Master's Thesis, Naval Postgraduate School, Monterey, California, December, 1989.

Bullett, T.W., Telephone conversation, September 19, 1990.

Campbell, R.S., *Development and Integration of the NPS Middle Ultraviolet Spectrograph with an Extreme Ultraviolet Spectrograph*, Master's Thesis, Naval Postgraduate School, Monterey, California, December, 1989.

Chamberlain, J.W., *Theory of Planetary Atmospheres, An Introduction to Their Physics and Chemistry*, Academic Press, 1978.

Clayton, M.J., *Analysis of the Ultraviolet Emissions of Nitric Oxide from Mid-Latitude Rocket Observations*, Master's Thesis, Naval Postgraduate School, Monterey, California, June, 1990.

Cleary, D.D., *Analysis of Nitric Oxide Fluorescence Bands From High Latitude Rocket Observations of the Thermospheric Dayglow*, Ph.D. Dissertation, University of Colorado, 1985.

Cleary, D.D., "Daytime High-Latitude Rocket Observations of the NO  $\gamma$ ,  $\delta$ , and  $\epsilon$  Bands," *Journal of Geophysical Research*, 91, 11337, 1986.

Cleary, D.D., McCoy, R.P., Harada, L.K., and Chakrabarti, S., "A self-consistent analysis of the HeI (537 Å, 584 Å) and OII (538 Å, 539 Å, 834 Å) EUV airglow from STP 78-1 satellite measurements," *EOS Transactions, American Geophysical Union*, 67373, 1987.

Cleary, D.D., Meier, R.R., Gentieu, E.P., Feldman, P.D., and Christensen, A.B., "An Analysis of the Effects of N<sub>2</sub> Absorption on the O<sup>+</sup> 834-Å Emission From Rocket Observations," *Journal of Geophysical Research*, 94, 17281, 1989.

Danczyk, G.M., *Identification of Thermospheric Dayglow Emissions for the MUSTANG Experiment*, Master's Thesis, Naval Postgraduate School, Monterey, California, December, 1989.

Eisberg, R. and Resnick, R., *Quantum Physics of Atoms, Molecules, Solids, Nuclei, and Particles*, Second Edition, John Wiley & Sons, Inc., 1985.

Grum, F., and Luckey, C.W., "Optical Sphere Paint and a Working Standard of Reflectance," *Applied Optics*, 7, 2289, 1968.

Hedin, A.E., "A Revised Thermospheric Model Based on Mass Spectrometer and Incoherent Scatter Data; MSIS-83," *Journal of Geophysical Research*, 88, 10170, 1983.

Herzberg, G., *Molecular Spectra and Molecular Structure I. Spectra of Diatomic Molecules*, Second Edition, Van Nostrand Company, Inc., 1950.

McCoy, R.P., Anderson, D.E., Jr., and Chakrabarti, S., "F<sub>2</sub> Region Ion Densities from Analysis of O<sup>+</sup> 834-Å Airglow: A parametric study and comparisons with satellite data," *Journal of Geophysical Research*, 90, 12257, 1985.

NASA Technical Report 32822, *Ultraviolet Spectroscopy of Planets*, Barth, C.A., 1965.

NASA Technical Memorandum 80286, *Atomic Emission Lines in the Near Ultraviolet; Hydrogen Through Krypton*, Section II, Kelly, R.L., 1979.

Reader, J., Corliss, C.H., Wiese, W.L., and Martin, C.A., *Wavelengths and Transition Probabilities for Atoms and Atomic Ions*, U.S. Department of Commerce, 1980.

Siskind, D.E., Barth, C.A., and Cleary, D.D., "The Possible Effect of Solar Soft X Rays on Thermospheric Nitric Oxide," *Journal of Geophysical Research*, 95, 4311, 1990.

Wallace, L., "A Collection of Band-Head Wavelengths of N<sub>2</sub> and N<sub>2</sub><sup>+</sup>," *The Astrophysical Journal Supplement Series*, 62, 445, 1962.

Wallace, L., "Band-Head Wavelengths of C<sub>2</sub>, CH, CN, CO, NH, NO, O<sub>2</sub>, OH, and Their Ions," *The Astrophysical Journal Supplement Series*, 68, 165, 1962.

Wiese, W.L., Smith, M.W., and Glennon, B.M., *Atomic Transition Probabilities, Vol I, Hydrogen Through Neon*, U.S. Department of Commerce, 1966.

## INITIAL DISTRIBUTION LIST

- |     |  |   |
|-----|--|---|
| 1.  | Commandant (G-EVC-3)<br>United States Coast Guard<br>2100 2nd Street SW<br>Washington D.C. 20593                           | 2 |
| 2.  | Defense Technical Information Center<br>Cameron Station<br>Alexandria, Virginia 22304-6145                                 | 2 |
| 3.  | Library, Code 0142<br>Naval Postgraduate School<br>Monterey, California 93943-5000   | 2 |
| 4.  | Dr. K. Woehler, Chairman<br>Physics Department<br>Naval Postgraduate School<br>Monterey, California 93943-5000             | 1 |
| 5.  | Dr. David D. Cleary<br>Physics Department, 61-CL<br>Naval Postgraduate School<br>Monterey, California 93943-5000           | 3 |
| 6.  | Dr. S. Gnanalingam<br>Physics Department, 61-GM<br>Naval Postgraduate School<br>Monterey, California 93943-5000            | 1 |
| 7.  | Dr. R. McCoy<br>Code 4140<br>Naval Research Laboratory<br>Washington D.C. 20375  | 1 |
| 8.  | Dr. Larry Paxton<br>Room 24-E115<br>Johns Hopkins Applied Physics Lab<br>Johns Hopkins Road<br>Laurel, Maryland 20723-6099 | 1 |
| 9.  | LT Michael J. Clayton<br>Physics Department<br>United States Naval Academy<br>Annapolis, Maryland 21402-5000               | 1 |
| 10. | LT Carl K. Andersen<br>15073 Camellia Lane<br>Dumfries, Virginia 22026   | 1 |